Particle Architecture and Surface Engineering of NIR-to-VIS Upconversion Nanoparticles as Luminescent Probes for Bioapplications

Dissertation

zur Erlangung des Doktorgrades der Naturwissenschaften

(Dr. rer. nat.)

an der Fakultät für Chemie und Pharmazie

der Universität Regensburg

vorgelegt von

Alexandra Schroter

aus Regensburg

im Juli 2023

Die vorliegende Dissertation entstand in der Zeit von Januar 2020 bis Juli 2023 am Institut für Analytische Chemie, Chemo- und Biosensorik der Universität Regensburg.

Die Arbeit wurde angeleitet von Dr. Thomas Hirsch und Prof. Dr. Antje Baeumner.

Promotionsgesuch eingereicht am: 19. Juli 2023

Promotionskolloquium: 25. September 2023

Prüfungsausschuss:

Vorsitzender: Prof. Dr. Oliver Tepner

Erstgutachter: Dr. Thomas Hirsch

Zweitgutachterin: Prof. Dr. Antje Baeumner

Drittprüfer: Prof. Dr. Patrick Nürnberger

Danksagung

Zuallererst möchte ich mich bei **Prof. Antje Baeumner** und **Dr. Thomas Hirsch** bedanken, die mir die Möglichkeit gegeben haben, meine Promotion in diesem Arbeitskreis über ein so spannendes Thema anzufertigen. Danke für die gute Betreuung und all die Unterstützung in den letzten Jahren!

Des Weiteren bedanke ich mich bei **Prof. Patrick Nürnberger** für die Übernahme der Aufgabe des Drittprüfers und bei **Prof. Oliver Tepner** dafür, dass er sich bereit erklärt hat, den Prüfungsvorsitz zu übernehmen.

Mein Dank geht auch an **Prof. Reinhard Rachel**, der mir die Möglichkeit und Unterstützung gegeben hat in den letzten Jahren zahlreiche Messungen am Transmissions-Elektronenmikroskop durchzuführen. Bei **Joachim Rewitzer** bedanke ich mich vor allem für die durchgehende Hilfe und gute Zusammenarbeit am ICP-OES. **Dr. María Marín** und **Dr. Carla Arnau del Valle** von der UEA (Norwich) möchte ich für all ihr Engagement in unserem gemeinsamen Forschungsprojekt danken.

Ein großes Dankeschön geht an das **Upcon-Team** (sowohl den alten als auch den neuen Mitgliedern) für die tolle Zusammenarbeit und Unterstützung in jeder Hinsicht. Allen voran **Dr. Thomas Hirsch**, der mit mir alle wissenschaftlichen Fragestellungen und Ergebnisse bis ins kleinste Detail durchdiskutiert hat, mir aber auch viel Freiraum gelassen hat, neue Ideen umzusetzen. Ich habe während meiner Zeit in dieser Arbeitsgruppe sehr viel gelernt, und das verdanke ich zu großen Teilen ihm.

Ein ganz besonderer Dank geht an **Dr. Susanne Märkl**, die sowohl arbeitstechnisch als auch privat mein Leben extrem bereichert hat und es auch immer noch tut. Danke für die schöne Zeit im Büro, für die unzähligen Diskussionen und Gespräche (egal ob arbeitsrelevant oder nicht) und danke für die Aufnahme von über tausend TEM-Bildern während meiner synthesewütigen Phase.

Danke auch an all meine Kollegen aus dem 4. Stock. Besonderer Dank geht an meine derzeitigen Bürokolleginnen **Sophia Baumann** und **Naomi Weitzel** für alle wissenschaftlichen und unwissenschaftlichen Gespräche und Diskussionen. Bei dem Superhelden-Büro bestehend aus **Patrick Recum**, **Christoph Bühler** und **Laurin Hastreiter** bedanke ich mich insbesondere für die schönen nachmittäglichen Kaffeepausen, Feierabendbiere und für all den Blödsinn zwischendurch, der mir den Arbeitsalltag sehr versüßt hat. Auch den „alten" Kollegen **Dr. Lukas Wunderlich** und **Dr. Eva-Maria Kirchner** möchte ich für die schöne Zeit innerhalb und auch außerhalb der Arbeit danken. Zudem danke ich auch **Rosmarie Walter** für ihre immerwährende Unterstützung und ihr stets offenes Ohr.

Zu guter Letzt geht ein riesiges Dankeschön an meine Eltern **Karin** und **Andreas** für ihre durchgängige Unterstützung in jeglicher Hinsicht und dafür, dass sie immer an mich geglaubt und mir immer alles ermöglicht haben. Ohne euch wäre ich nie so weit gekommen! Ebenso möchte ich meiner Schwester **Franziska** danken, die bei jeglichen Problemen immer für mich da war. Besonderer Dank geht auch an meinen Freund **Tobias**, der mich insbesondere in der letzten Phase der Promotion extrem unterstützt hat, mir so viel abgenommen hat, wie er konnte und mir die nötige Kraft gegeben hat, bis zum Ende durchzuhalten.

Table of Contents

Declaration of Collaborations

The author carried out most of the experiments and data evaluation presented in this work. Some results were obtained in collaboration with other researchers. In accordance with § 8 Abs. 1 Satz 2 Ziff. 7 of the "Ordnung zum Erwerb des akademischen Grades eines Doktors der Naturwissenschaften (Dr. rer. nat.) an der Universität Regensburg vom 18. Juni 2009", this section gives information about these collaborations.

Chapter 3: Upconversion Nanocrystals with High Lanthanide Content: Luminescence Loss by Energy Migration versus Luminescence Enhancement by Increased NIR Absorption

This manuscript was published after peer-reviewing. The author synthesized all nanoparticles, with exception of β-NaYF$_4$(20%Yb,20%Er)@NaYF$_4$ and β-NaYF$_4$(80%Yb,2%Er)@NaYF$_4$, which were synthesized by Naomi Weitzel. All surface modifications were conducted by the author, as well as luminescence, lifetime, and absorption measurements. Characterizations as well as all data evaluations and interpretations were done solely by author. Susanne Märkl recorded the transmission electron micrographs. The manuscript was revised and edited by the author and Thomas Hirsch. Thomas Hirsch is the corresponding author of the publication.

Chapter 4: Bilayer-Coating Strategy for Hydrophobic Nanoparticles Providing Colloidal Stability, Functionality, and Surface Protection in Biological Media

This manuscript was published after peer-reviewing. This work is a cooperation of the University of Regensburg and University of East Anglia.

The author synthesized all upconversion core and core-shell nanoparticles used within the publication. The surface modifications of different sized core-shell particles with the bilayer strategy, including variations of the incorporated amine were done by the author. Investigation of the formed bilayer by negative staining in TEM as well as freeze drying experiments were performed by the author. The author developed and realized the protocols for coupling of Rose Bengal, NO-probe, and gold nanoparticles to the bilayer of UCNPs. All characterizations of the particles with TEM, DLS, ICP-OES, zeta potential, absorption, and luminescence were carried out by the author. Carla Arnau del Valle synthesized and characterized the NO-probe and characterized the absorption and fluorescence properties UCNPs@bilayer-RB and UCNPs@bilayer-NO-probe, which were used for cellular experiments. She conducted

the experiments regarding singlet oxygen generation and nitric oxide detection in solution and performed all experiments with cell cultures.

The manuscript was revised and edited by the author, Carla Arnau del Valle, María J. Marín, and Thomas Hirsch. María J. Marín and Thomas Hirsch are corresponding authors.

Chapter 5: Control of Luminescence and Interfacial Properties as Perspective for Upconversion Nanoparticles

This chapter has been published as perspectives article. Concept and structure of the article were planned by the author and Thomas Hirsch. The author did the literature survey and wrote the manuscript. The manuscript was revised by the author together with Thomas Hirsch. Thomas Hirsch is the corresponding author.

Abstract

Lanthanide-doped upconversion nanoparticles (UCNPs) have emerged as promising candidates for various biological applications since they can be excited with near-infrared light, which is characterized by minimal scattering and negligible background fluorescence excitation in tissues. Within this thesis, one of the main challenges of UCNPs is tackled: the low upconversion efficiency and thus low brightness. An enhancement strategy is presented that combines an augmented NIR absorption rate through increased sensitizer content with the blocking of energy migration pathways to the particle surface by passivating the active core with an optically silent shell. Notably, 8.5 nm sized UCNPs composed of $NaYbF_4(20\%Er)$ with a 2 nm thick $NaYF_4$ shell exhibit significantly improved upconversion luminescence in the red spectral range compared to commonly used particles with only 20% Yb^{3+} and 2% Er^{3+}. The impact of particle size, composition, and core-shell architecture on the photophysical properties is investigated, demonstrating that increased doping rates enable the design of small and bright UCNPs with immense potential for biological applications. To bridge the gap between such a particle design and applications in biologically relevant environments, sophisticated surface chemistry of nanoparticles is fundamental. In this context, a bilayer-based surface modification strategy is introduced, offering excellent colloidal stability in aqueous environments, while enabling facile surface functionalization through simple carbodiimide chemistry. This is demonstrated using originally hydrophobic UCNPs coated with oleate, on which a bilayer forms after addition of further excess oleate. The resulting hydrophobic interlayer prevents the diffusion of water or other hydrophilic molecules to the particle surface and thus reduces luminescence quenching. By incorporating additional amino-functionalized molecules, the colloidal stability is enhanced and at the same time the introduction of desired functionalities is facilitated. This was demonstrated with two proof-of-concept studies using a photosensitizer and a nitric oxide (NO) probe. When attached to the particle surface, their functionality for producing singlet oxygen and detecting intracellular NO is maintained.

The design of UCNPs always requires sophisticated particle composition and architecture as well as thoughtful surface engineering. When both are successfully combined, UCNPs show promise as nanolamps in applications where deep tissue penetration is required, such as in photodynamic therapy or optogenetics.

Zusammenfassung

Lanthanoid-dotierte Upconversion-Nanopartikel (UCNPs) haben sich als vielversprechende Kandidaten für verschiedene biologische Anwendungen erwiesen, da sie mit Nahinfrarot-Licht (NIR) anregbar sind, was zu einer minimalen Streuung und Hintergrundfluoreszenz im Gewebe führt. In dieser Arbeit wird eine der größten Herausforderungen von UCNPs behandelt: die geringe Upconversion-Effizienz und die damit verbundene geringe Helligkeit. Zur Steigerung der Effizienz wird eine Strategie vorgestellt, die einen erhöhten Sensibilisatorgehalt zur Verbesserung der NIR-Absorptionsrate mit einer Blockierung der Energiemigration durch eine optisch inaktive Hülle kombiniert. Dabei weisen 8,5 nm große UCNPs aus $NaYbF_4$(20%Er) mit einer 2 nm dicken $NaYF_4$-Hülle eine deutlich verbesserte Lumineszenz im roten Spektralbereich auf, verglichen mit üblicherweise verwendeten Partikeln mit nur 20% Yb^{3+} und 2% Er^{3+}. Die Auswirkungen von Partikelgröße, Zusammensetzung und Kern-Hülle-Architektur auf die photophysikalischen Eigenschaften werden untersucht. Dabei zeigt sich, dass durch höhere Dotierungen die Entwicklung von kleinen, hellen UCNPs mit immensem Potenzial für Bioanwendungen ermöglicht wird. Für die tatsächliche Anwendung solcher Partikel ist eine ausgefeilte Oberflächenchemie von grundlegender Bedeutung. Dazu wird eine Strategie vorgestellt, die durch Bildung von Doppelschichten eine ausgezeichnete kolloidale Stabilität in wässriger Umgebung bietet und gleichzeitig Oberflächenfunktionalisierung durch einfache Carbodiimidchemie ermöglicht. Dies wird anhand von ursprünglich hydrophoben, mit Oleat beschichteten UCNPs demonstriert, bei denen sich nach Zugabe von weiterem Oleat im Überschuss eine Doppelschicht bildet. Die dabei entstehende hydrophobe Zwischenschicht verhindert die Diffusion von Wasser oder anderen hydrophilen Molekülen an die Partikeloberfläche und verringert somit Lumineszenzlöschung. Ein Einbau von zusätzlichen Aminen erhöht die kolloidale Stabilität und erleichtert spätere Anknüpfung gewünschter Funktionalitäten. Dies wurde experimentell in zwei Proof-of-Concept-Studien mit einem Photosensibilisator und einer Stickstoffmonoxid (NO)-Sonde nachgewiesen. Die Funktionalität dieser Moleküle für die Singulett-Sauerstoffproduktion und den Nachweis von intrazellulärem NO bleibt auch nach der Bindung an die Partikeloberfläche erhalten.

Das Design von UCNPs erfordert grundsätzlich eine ausgefeilte Partikelzusammensetzung und -architektur, sowie gut durchdachte Oberflächenchemie. Wird beides erfolgreich kombiniert, bieten sich UCNPs als Nanolampen für Anwendungen an, bei denen ein tiefes Eindringen in das Gewebe erforderlich ist, wie z. B. die photodynamische Therapie oder die Optogenetik.

1 Introduction

1.1 Luminescent Nanoprobes for Bioapplications

1.1.1 The Role of Light in Medicine

The development of non-invasive imaging techniques or diagnostic tools is one of the most elementary research goals in medicine. For the accomplishment of this goal, optical probes have become an indispensable tool. As tracking the interaction of light with cells or biomolecules can be usually done in a simple manner without causing a patient harm, this principle is extremely attractive. Several areas of medicine or molecular biology work with light, either in diagnosis by reading light information or in therapy by irradiation with light. Optical probes can be applied to stain certain regions in cells and tissues, and therefore eventually help to diagnose illnesses. Techniques such as confocal microscopy or fluorescence imaging are used, for example, for early cancer detection.[2,3] Light-based techniques also allow real-time monitoring of physiological parameters like glucose levels, pH, blood pressure, or blood saturation, which are important to determine in daily medicine.[4,5]

However, optical systems can not only be used for imaging and diagnostic purposes. New methods have emerged in the past years which use light as therapeutic agent. Among them are approaches like light-induced drug delivery or photodynamic therapy, which all involve the use of light to trigger light sensitive drugs or selectively target and destroy cancer cells upon light irradiation.[6,7] It is even possible to manipulate neurons with light in a method called optogenetics, which is a promising technique for the therapy of neuronal diseases.[8]

The concept is of course extremely tempting: Diagnosis and therapy with pure light. However, to realize this, some questions need to be answered and concepts have to be developed: How can the optical probe or therapeutic agent travel through the organism even if the compound is not water soluble? How is it possible to create a probe with a therapeutic function that attacks only the target cells? How is it possible to create a self-referencing optical probe? To address these challenges, single molecules are no longer sufficient; instead, small mobile nano-sized platforms are needed with tailored optical features as well as the ability to attach various functions. To meet these requirements, luminescent nanoparticles were developed.

1.1.2   Luminescent Nanomaterials

Nanomaterials come in the range of usually 1-100 nm in size in at least one dimension, which places them somewhere between molecules and bulk materials.[9] This can be advantageous in several respects. Much more complex structures can be established in nanoparticles compared to single molecules, such as the combinations of different materials to obtain special optical, electrical, mechanical, or chemical properties, which differ strongly from bulk materials.[10] At the same time, they are small enough to be dispersible in solvents without showing significant scattering and to move reasonably freely in organisms, which is what makes them very attractive for medical applications.[11]

The main advantage of nanoparticles in comparison to simple molecules, complexes, or proteins is that they have in total a large surface, which can be functionalized with receptors, targeting moieties, or drugs and hereby often achieve a higher bioavailability compared to direct administration.[12,13] The application of nanoparticles for medical purposes is not only advantageous in terms of creating a nanocarrier; depending on the material chosen for nanoparticle preparation, the particles can have fascinating optical properties, allowing them to function not only as transporters but also as so-called small luminescent nanolamps.

Several luminescent nanomaterials are already broadly used in medical research with very different properties, which can be based on either organic or inorganic materials. Well-known examples for organic materials are fluorescent proteins, which are used as markers for gene expression[14] or liposomes that are known to be excellent transporters.[15] Such materials usually profit from low toxicity but *e.g.*, organic fluorescent dyes or proteins generally have the disadvantage of suffering from photobleaching. Another example are carbon-based nanoparticles like carbon dots, which also represent an important class of organic luminescent nanomaterials and are used in a wide range of biomedical applications.[16] They also show low toxicity and unlike other organic materials relatively high photostability.[17] The most famous example of inorganic luminescent nanoparticles are semiconductor quantum dots, which are based on semiconducting materials like CdSe or PbS. Their potential for *in vivo* and *in vitro* applications is also extensively exploited due to their excellent photostability and their possibility for surface functionalization. However, since most quantum dots contain toxic elements like Cd or Pb, their organic counterpart, the aforementioned carbon dots, have received more attention in recent years when it comes to biological applications.[16]

Beside these numerous advantages for using light-based technologies in medicine, a question remains: How is the light penetrating the body? Most of the methods are claimed to be non-invasive, however, light in the UV and visible range, as required to excite most optical probes, is barely able to penetrate the uppermost skin layers.[18] While this may be less of an issue when working outside of organisms, such as in cell cultures or with collected samples, it would be desirable for many applications if the light could penetrate deeper into the tissue, thus avoiding the need to implant optical fibers. The penetration of light into a medium depends on several factors, in particular absorption and light scattering. Absorption in tissue is mainly attributed to the absorption bands of hemoglobin, melanin, and water. In contrast, light scattering, decreases continuously with increasing wavelength ($\sim\lambda^{-4}$ for Rayleigh scattering, $\sim\lambda^{-b}$ for Mie scattering, where b is a material dependent variable), leading to higher penetration depths with increasing wavelength (Figure 1.1).[18,19] Since every skin layer has different scattering and absorption properties and the intensity of the light has additional influence, different values for penetration depths can be found in literature but they generally range from 1 mm (for shorter wavelength close to UV) to 5 mm (for wavelengths close to the NIR),[18,20] what means that NIR light, for example, can be used to reach blood vessels to enable biosensing or therapeutic approaches there.
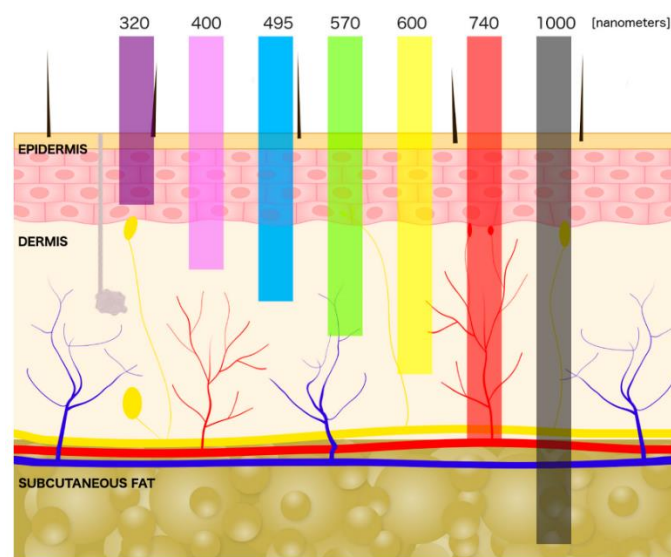
Figure 1.1. Penetration of light with different wavelength into the skin. The graphic was reprinted from Ref.[21]

To exploit the higher penetration depths of low-energy light for medical applications, a special class of luminescent materials has been brought into the light: The so-called upconversion nanoparticles. These are lanthanide-doped crystals, which are excitable with near infrared (NIR) light and emit in the visible and UV range. This feature makes them highly attractive for all kinds of bioapplications, where deeper light penetration is desired.[22]

1.2 Lanthanide Luminescence

1.2.1 Rare-Earth Elements

Lanthanides, which belong to the rare earth elements, occupy the f-block of the periodic table. Unlike the name rare earth says, they are not particularly rare, as the abundance is partly even higher compared to cobalt or lead.[23] However, they are broadly spread around the world in relatively small concentrations and are often found together in minerals. Thus, they are difficult to extract and it is challenging to purify them due to their very similar chemical properties.[23]

Lanthanides are indispensable for today's world, what is attributable to their unique properties and characteristics. Due to their special luminescent properties, they are used for lasers and lighting applications like LEDs. They are also employed in display technologies and are therefore required for smartphones, computer monitors, or flat screens. Additionally, they have special importance in catalysis and due to their magnetic properties also in the production of high-performance magnets.[23,24]

Besides those more industrial applications, they have gained great importance for medical applications. Gadolinium, for example, is widely used in magnetic resonance imaging (MRI) as contrast agent, or the radioactive isotope of lutetium (^{177}Lu) is applied in targeted radiation therapy for prostate cancer. By combining this isotope with targeting molecules, it is possible to selectively reach tumor cells, which are then destroyed by the radioactive radiation.[25] A wide range of applications naturally results from the excellent optical properties. The research in luminescence imaging, design of luminescent probes, or sensors and therapeutic methods such as drug delivery, photodynamic therapy, or photothermal therapy is expanding strongly.[26]

1.2.2 Optical Properties of Lanthanide Ions

Lanthanides, especially trivalent lanthanides (Ln^{3+}) with the electronic configuration [Xe]f^n (n = 0 - 14), have very special optical properties since the occupation of 4f-orbitals generates a high number of possible electronic states (up to 327 for Gd^{3+}) (Figure 1.2).[27] Those energy levels originate from different distributions of the valence electrons in the seven f-orbitals and are split due to spin-orbit coupling. In spin-orbit coupling, the magnetic field originating from the movement of the electron around the nucleus interacts with the magnetic field generated by the electron spin. Depending on how the spin and the orbital angular momentum are aligned to each other (parallel or antiparallel), the state is higher or lower in energy. The levels are

described by the term symbols $^{2S+1}L_J$, where 2S+1 equals the total spin (S) multiplicity, L is the total orbital angular momentum, and J the total angular momentum.[24]

Figure 1.2. Energy level diagram of trivalent lanthanide ions. The graphic was adapted from Ref.[28] with permission from the royal society of chemistry. UV (350 nm), blue (470 nm) green (540 nm), and red (650 nm) light is depicted in the same energy scale for comparison.

This large number of electronic states already gives an indication of the diverse optical properties of the Ln^{3+} elements. However, most of the transitions are in principle not very probable, which is mainly caused by selection rules, like the spin selection rule or the Laporte's rule.[29] The Laporte's rule states that particularly electric dipole (ED) transitions are only allowed if the parity changes and $\Delta L = \pm 1$ holds,[30] which is not the case for 4f-4f transitions. In an ED-allowed transition, the electronic charges of the orbitals are redistributed during the transition, resulting in a change in ED-moment. For 4f-4f transitions, there is no change in dipole moment, making the transition ED-forbidden. Instead, a change in the electric quadrupole (EQ) moment is observed. EQ-transitions are by far not as intense as ED-transitions (about 10^7-10^{10} times weaker).[31] However, the environment plays an extremely important role here. It is assumed that especially in low-symmetry environments a mixing of the f and d orbitals can take place, which gives the transition 4f-5d character and thus increases the probability of the transition.[31] This was for instance demonstrated by Bünzli *et al.*, who found an increase of luminescent quantum yield from 35 - 39% to

50% by changing the symmetry from C_3 to C_1 in europium complexes.[32] Hence, it is almost inevitable to deal with the symmetry of the environment of the ions, regardless of whether one works with lanthanide complexes or with solids, since this strongly influences the photophysics.[32,33]

Throughout this work, lanthanide emissions are described as "luminescence". Luminescence is a quite general term for the emission of light, and usually the terms fluorescence or phosphorescence are used to describe specific phenomena. While fluorescence describes spin-allowed, very fast transitions, phosphorescence describes spin-forbidden transitions with long lifetimes.[29] According to this definition, transitions like $^2F_{5/2} \rightarrow {}^2F_{7/2}$ in Yb^{3+}, which are spin-allowed, are denoted as fluorescence, while the Eu^{3+} emission $^5D_0 \rightarrow {}^7F_2$ is phosphorescent. In case of upconversion processes, which are explained in the next section, both descriptions are not particularly adequate. Thus, for simplicity the term luminescence is used for all occurring light emissions.

1.2.3   The Upconversion Mechanism

Beside the described luminescence properties of Ln^{3+} ions, they feature a phenomenon which makes them extremely attractive, especially for bioapplications. It was pioneered by François Auzel in the 1960s that under certain conditions, lanthanides can also have anti-Stokes emissions, the so-called upconversion luminescence (UCL).[34] This special effect is enabled by the energy levels being close to each other, literally forming a ladder, combined with long lifetimes of the intermediate states.[35] By subsequent absorption of several photons, high excited states can be reached. Due to this effect, the Ln^{3+} can be excited in the NIR and emit in the visible range up to the UV range.[22,36] There are three main pathways described in the literature, which enable the upconversion effect: excited state absorption (ESA), energy transfer upconversion (ETU), and photon avalanche (PA) (Figure 1.3). In ESA, an excited-state ion must absorb a second photon to achieve upconversion, which is a process with low probability and therefore requires high excitation power densities to achieve efficient UCL. The main effect with the largest contribution is therefore ETU, which is about two orders of magnitude more efficient compared to ESA.[36] Here, two different types of lanthanide ions are usually combined, a sensitizer with a high absorption cross-section, serving as energy harvester, and an activator ion that serves as the emitter.
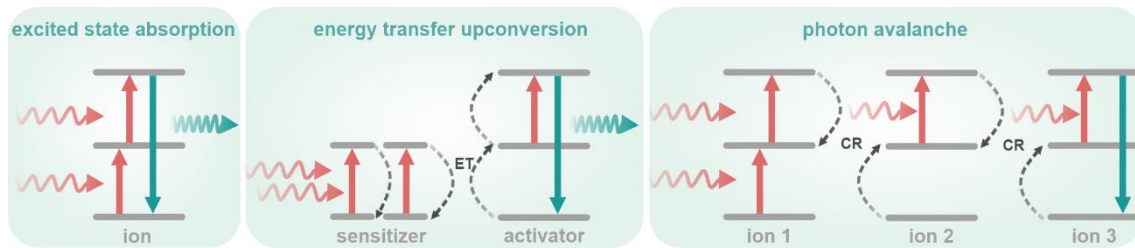
Figure 1.3. The three main mechanisms for upconversion: Excited state absorption (ESA), energy transfer upconversion (ETU), and photon avalanche (PA).

By far the most used sensitizer among the lanthanides is Yb^{3+}, which has only one excited state level that can be reached after NIR absorption. Therefore, competing side processes within the Yb^{3+} ions are limited, resulting in high energy transfer efficiencies. Transfer of energy from the surrounding sensitizer ions to an activator ion can consequently allow high excited states to be reached quite easily.[36] The last process that shall be discussed here, is photon avalanche. This process is rather a special case since high power densities are required and the contribution should be relatively small under moderate conditions. The process begins with ESA, followed by cross-relaxation with another ion in ground state (CR), ending with both ions in medium excited states. This process repeats until all ions are in the medium excited state. From this point on CRs are not possible anymore, and every further occurring ESA leads to population of high-excited states, followed by a strong emission of UCL.[37]

By combining different 4f-elements, a huge variety of excitation and emission wavelengths is in principle possible (Figure 1.4). The most common lanthanide combinations are Yb^{3+}/Er^{3+} or Yb^{3+}/Tm^{3+}, where Yb^{3+} acts as sensitizer ion and absorbs NIR light with a wavelength of 980 nm, while Tm^{3+} or Er^{3+} act as activators, which emit UV or visible light.[38]
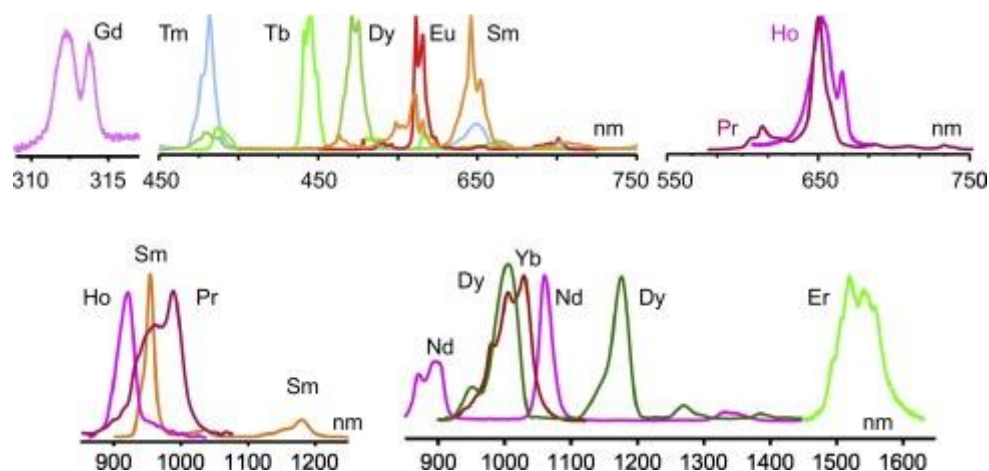

Figure 1.4. Emissions of trivalent lanthanide ions. The graphic was reprinted with permission from Ref. [29], ©2016 Elsevier.

1.3 Upconversion Nanoparticles

One of many possibilities to exploit the unique optical abilities of lanthanides, especially the ability of creating upconverted light, is to dope the Ln^{3+} ions into nanoparticles. By co-doping of sensitizers and activators the upconversion effect can be achieved and simultaneously, the suitability for bioapplications due to the small size of the nanoparticles is ensured. Hence, those upconversion nanoparticles (UCNPs) have gained special attention among the vast field of nanotechnology and an incredible number of possible applications for such particles have emerged in recent years, ranging from bioimaging and biosensing to therapeutic methods such as drug delivery, photodynamic or photothermic therapy, and optogenetics.[39]

The main feature, making those nanoconstructs so attractive for applications in the biological world, is the NIR-excitation. Using excitation wavelengths that lie in optically silent regions comes with great benefits: The scattering is reduced with increasing wavelength and most biomolecules show no absorption in the NIR range. This leads to higher penetration depth in biological tissues and to reduced autofluorescence, and therefore high signal-to-noise ratios.[40] The upconversion emission bands are quite narrow since the 4f-orbitals are barely affected by the chemical environments and they do not show blinking like quantum dots, for example, or suffer from photobleaching.[41] Since each Ln^{3+} ion has its characteristic emission bands, a wide range of possible emission bands is available for selection; by combining Er^{3+} and Tm^{3+} activators, for example, emission bands in the UV, blue, green, and red range of the spectrum can be achieved, with intensity ratios that can be tuned dependent on the respective concentrations (Figure 1.5).
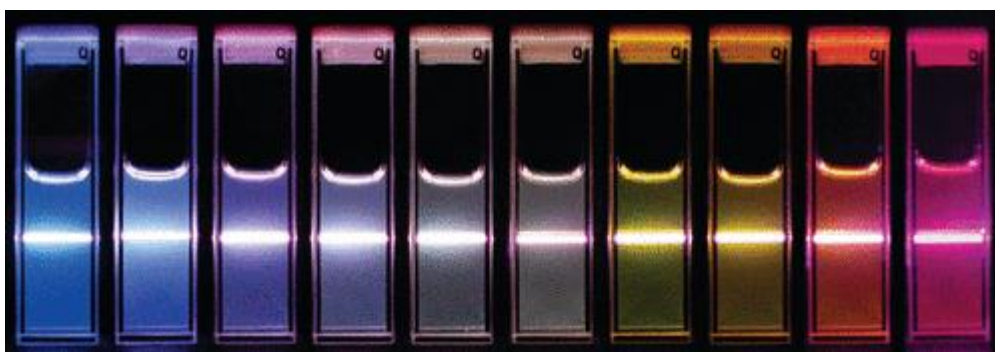

Figure 1.5. Upconversion colors under 980 nm excitation of $NaYF_4$ particles with different doping concentrations of Yb^{3+}, Er^{3+}, and Tm^{3+} ions. The graphic is reprinted with permission from Ref.[38]

The fact that the photophysical properties of lanthanides are so versatile is a great advantage, but it also requires an extremely precise particle design. As the transitions between the energy levels are not allowed according to the Laporte rule they are in

general improbable. However, this can be partially circumvented by asymmetric environments of the Ln^{3+} ions. In addition, many non-radiative competing processes such as unwanted cross-talk between lanthanides or with quenchers in the environment can greatly reduce the upconversion efficiency.[42,43] Therefore, one of the main goals in upconversion research is to design the particles in a way that such competitive processes are suppressed and the efficiency is maximized so that the particles are bright enough for biomedical applications.

1.3.1 Preparation of Upconversion Nanoparticles

1.3.1.1 Choice of Host Material

For the creation of lanthanide-based nanoparticles, it is necessary to build a solid host matrix in which the lanthanide ions can be chemically embedded. The choice of such a host material is actually highly important, since it should interfere as little as possible with the excitation and emission wavelengths of the lanthanides. Moreover, the host material should be non-toxic and chemically inert under relevant biological conditions. The most important parameter that must be considered are phonon energies. These correspond to the lattice vibrations in solids, whose frequencies are highly dependent on the material. Those vibrations are the main reason for non-radiative relaxations within upconversion materials. However, luminescence loss can be minimized in host materials with low phonon energies, since then the probability of phonon relaxations is reduced.[41]

Table 1.1. Phonon energies of selected host materials for lanthanide doping.

material	highest phonon energy / cm^{-1}	Ref.
phosphate glass (*e.g.*, YPO$_4$)	1200	44
silicates	1100	45
fluoride glass	550	45
Gd$_2$O$_3$	700	46
YVO$_4$	890	47
NaYF$_4$	360	46
LaF$_3$	300	48
LaCl$_3$	240	49

Comparing different host materials (Table 1.1), it has been shown that fluoride-based crystal lattices have one of the lowest phonon energies combined with excellent chemical stability.[50,51] The most extensively studied among them is NaYF$_4$, which is proven to have excellent optical properties and matches the mentioned criteria for

host materials. It occurs in a cubic and hexagonal crystal system, which structures can both be easily synthesized depending on the synthesis temperature. Since the hexagonal crystal structure has a lower crystal symmetry, the UCL is usually much brighter, which is why this crystal structure is most often chosen for particle design.[52] Alternatives to $NaYF_4$ with similar upconversion properties are $LiYF_4$ or LaF_3, for example.[50] Even though $NaYF_4$ is superior in many cases, $LiYF_4$ can be advantageous, *e.g.*, in combination with Tm^{3+} doping since this crystal structure seems to promote the Tm^{3+} UV-emission.[53] This example shows that there is no universal choice of host lattice, but instead it is dependent on the desired optical output and on the lanthanides, which shall be doped inside the lattice.

1.3.1.2   Synthesis Strategies

Over time, various strategies for UCNP production have evolved. The best known procedure is certainly the thermal decomposition method, since high quality UCNPs with controllable size, shape, and composition can be produced.[54] For thermal decomposition, precursor materials are dissolved in high boiling organic solvents, usually oleic acid and octadecene. As precursor salts, lanthanide trifluoroacetates or the less toxic lanthanide chlorides can be used to introduce the lanthanides.[55,56] In the first reaction step, lanthanide oleates are formed and solvent as well as water residues are removed (Figure 1.6). Under precisely controlled temperature increase and inert atmosphere, the nanoparticles start to nucleate in the cubic crystal structure above 240 °C and in hexagonal crystal structure about 300 °C, in case of $NaLnF_4$ materials.[57] Since this method is the most popular one, it is very well investigated and the knowledge about tuning the parameters to obtain defined architectures is high.
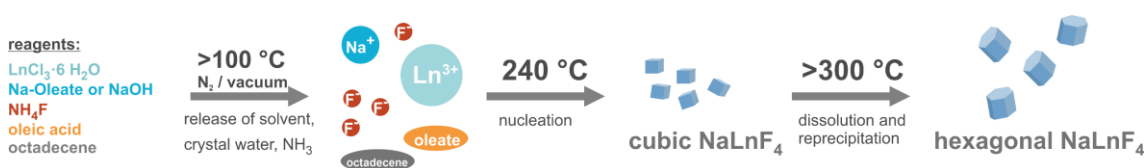

Figure 1.6. The basic protocol of upconversion nanoparticle synthesis *via* thermal decomposition using lanthanide chlorides. Synthesis procedure is drawn schematically according to an often used protocol.[58]

Another method for UCNP preparation is the hydrothermal synthesis, where the precursors are heated in aqueous, sometimes organic solvents at a controlled temperature and under high pressure.[59] This method is also frequently used even though it suffers from quite long reaction times (12-60 h) and requires special reaction vessels.[60] Co-precipitation is also a method investigated for UCNP production, which works with very gentle reaction conditions, since the precipitation of the nanoparticles is induced by the addition of precipitation agents, for example, rather than by high temperatures and pressure. This makes the method very easy to

perform, but the size distributions are usually much broader compared to the methods already mentioned.[60] The last method worth mentioning is the microwave-assisted nanoparticle synthesis. Since this method is relatively new, it has not yet received much attention from the research community, although some groups have already shown that it can produce nanoparticles with well-controlled architectures.[61,62] The underlying principle and also the chemicals used are identical to the thermal decomposition method but by using the microwave the synthesis is comparatively faster (a few minutes), and therefore more energy efficient compared to the classical thermal decomposition method.

Looking back at the last decades of UCNP research, it can be said that synthesis techniques have evolved a lot. After the principle of upconversion became known in the 1960s, it took about 40 years until the first high-quality monodisperse UCNPs could be produced. However, the development did not end there; the synthesis knowledge was further expanded until more complex architectures, such as core-shell, core-multishell, or anisotropic structures were also made possible.[63–65] The new architectural designs have generated a lot more opportunities for the design of UCNPs to achieve higher efficiencies and more versatile optical properties.

1.3.1.3   Composition and Architecture

Before starting the UCNP synthesis, it must be decided which lanthanides will be used as dopants and in which concentrations. For activator ions, which determine the emission wavelengths as depicted in Figure 1.4, Er^{3+}, Tm^{3+}, and sometimes Ho^{3+} are the most frequently used ions, which are in most cases combined with Yb^{3+} as sensitizer ion. The resulting most common particle compositions are hence $NaYF_4$(18-20%Yb, 2%Er) and $NaYF_4$(20-25%Yb, 0.3%Tm). Particles with such doping levels were proven to show efficient upconversion without inducing concentration quenching, caused by cross-relaxations and energy migration between the lanthanide ions.[22] The low content of optically active lanthanide ions in the crystals represents a limiting factor for the absorption-cross section of the nanoparticle as well as limited luminescence due to the low amount of emitting ions. As a consequence, the research community has recently started to rethink the low doping ratios and tried to optimize the composition of the particles.[66] The precise effects of enhancing lanthanide compositions have merely been addressed in detail so far, but it is obvious that the photophysical properties of the particles are somehow influenced. Therefore, this is a very current topic, which demands further research.

Beside the lanthanide doping, the particle architecture should be carefully designed as well. One strategy that has proven to be particularly efficient and important for UCNPs is core-shell architecture. In this approach, doped or undoped host material is grown onto the original nanoparticle within the framework of a core-shell synthesis. This strategy has been proven to be useful, for example, to increase the absorption cross-section of the particles by doping Yb^{3+} into an additional, so-called active shell, or for Nd^{3+}-sensitized systems, where a spatial separation of Nd^{3+} and the activator ion in different compartments of the UCNP has proven beneficial.[67,68] However, the growth of undoped shells is a frequently used method to increase upconversion brightness. Those shells, which are based on $NaYF_4$, for example, do not have optical properties by themselves but provide excellent protection of the particles from the environment and thus from quenching molecules and help to heal surface defects. This beneficial effect of inert shell growth usually results in a significant increase of the UCL of several orders of magnitude depending on the shell thickness and the particle size.[42]

Mainly due to the larger surface-to-volume ratio of small particles, the particle size itself strongly influences the particle properties (Figure 1.7), which means more options for quenching by solvent molecules, ligand molecules, or crystal defects on the surface.[69] As a result, the UCL of small UCNPs, especially below 10 nm size is usually low.[70] However, small sizes are often preferred for many applications, especially in the biological field. Therefore, efforts to improve the brightness of the particles, *e.g.*, by core-shell architecture, by co-doping with other ions such as Li^+ to change the crystal symmetry, or by increasing the concentration of sensitizer or activator, are high and still ongoing.[71–74]
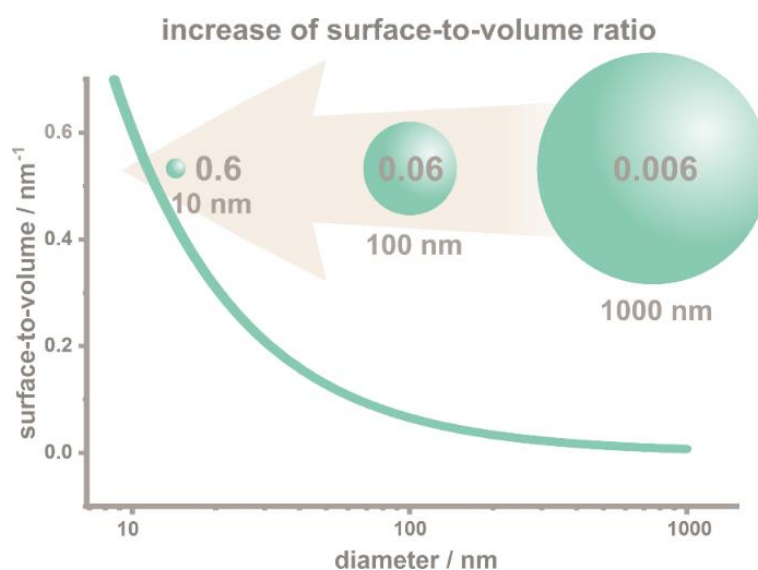

Figure 1.7. Dependence of surface-to-volume ratio on the nanoparticle diameter (for spherical particles).

1.3.1.4   Surface Engineering

The extraordinarily high surface-to-volume ratio of especially small nanoparticles (Figure 1.7) has also quite beneficial effects regarding the application of the UCNPs. Decreasing a particle size from one micron to 10 nm increases the surface area a thousandfold if the total volume of material remains constant. For medical applications, this means a thousandfold larger platform for attaching functional molecules to the particle. Such molecules, which can be either hydrophilic or hydrophobic, can be attached in high amounts, as long as the colloidal stability of the particle is maintained. Thus, biosensors can be created by coupling receptor molecules to the particle surface that induce a signal change in the presence of an analyte molecule.[12] Nanoparticles can also be used as transporters by loading them with therapeutic agents which are then released in a controlled manner. In such approaches, a higher drug bioavailability and thereby a higher drug efficiency is achieved compared to direct drug administration.[13] If additionally targeting ligands are attached to the nanoparticle surface, the target cells (*e.g.*, cancer cells) can be recognized, leading to a more specific and local therapeutic effect.[12]

Until UCNPs are ready to be applied, there is a long way to go. After the initial particle synthesis, the particles are usually coated with a hydrophobic ligand, such as oleic acid.[58] Thus, before UCNPs become accessible for biological applications at all, the surface must be modified so that the particles are dispersible in aqueous solutions. There are several requirements that should all be met by the surface ligands. The particles must not aggregate in pure water, nor under physiologically relevant conditions in the presence of salts or proteins. This issue of colloidal stability is also a direct result of the high surface-to-volume ratio, as high surface area means high surface energy. To minimize this energy, the nanoparticles form aggregates. This process can only be prevented by attaching stabilizing ligands to the nanoparticle surface, which are either highly charged or protect the particle sterically, as polymers do, for example.[75] The main challenge, when working in biological matrices is that many ions are present there, which weaken the electrostatic repulsion forces between the particles, and that biomolecules are sometimes able to displace ligand molecules.[76] In addition to colloidal stabilization, a protective barrier should be created around the particle to prevent water molecules from diffusing unhindered to the surface, because water has a strong quenching effect on the UCL.[77,78] Such a barrier can also mitigate dissolution processes of the nanoparticles that are triggered in high dilution.[79] In addition to all these tasks that a good ligand coating must fulfill, it is also important that the option of further functionalization is maintained, *e.g.*, for

attaching specific targeting ligands, drugs, organic dyes, or molecular probes, so that the above-mentioned applications are made possible.[80]

One of the biggest challenges in surface engineering of nanoparticles is that it is difficult to observe what processes really take place on the particle surface. To be able to improve the surface design, good analytical methods are needed to draw conclusions about the surface properties. Before modifying the surface, one should be able to estimate the amount of ligand needed to obtain reasonable and reproducible results. For this purpose, the number of particles in the dispersion and their total surface area should be determined. This can be achieved by a combination of size determination *via* transmission electron microscopy (TEM) and concentration determination of the lanthanides *via* elemental analysis, *e.g.*, with inductively coupled plasma optical emission spectroscopy (ICP-OES). After the surface is modified, the colloidal stability can be checked by measuring dynamic light scattering (DLS). Depending on the hydrodynamic diameter and polydispersity index, good estimations can be made regarding the degree of agglomeration and the size of the attached ligands.[81] To ensure the ligand attachment to the nanoparticle surface, zeta potentials can additionally be determined, where information on the electric potential (in mV) of the particle surface can be obtained, or, more precisely, the potential, which is formed at the stationary charge layer surrounding the particle, is measured.[82] Based on the change in zeta potential before and after surface modification, sometimes conclusions can be drawn about the success of a modification. In addition, it can give an indication of whether the colloidal dispersion is sufficiently stabilized since a zeta potential of at least ± 30 mV is assumed to be sufficient for electrostatic stabilization.[83] In case the attached ligand has absorbing or fluorescent properties, optical analytical techniques are also a common method to determine ligand concentration. These techniques are only a fraction of the analytical methods that can be used for surface characterizations depending on the exact ligand properties, however, they are probably the most important and most widely used.

Regarding the protocol of surface modification, there are already countless possibilities how the surface of UCNPs can be customized.[78,84] Which of these possibilities is chosen in the end usually depends on the subsequent purpose of the particles. For example, there are very simple particle modifications, like ligand exchange procedures,[78] that work in a simple and reliable manner but offer little protection in biological media regarding colloidal stability and water quenching. However, ligand exchange strategies are extremely versatile and allow attachment of small molecules as well as polymers, which is why many researchers choose this

method. Strategies that form a better barrier against external influences, by forming amphiphilic layers, for example, are in contrast often expensive and/or very complex, like methods involving amphiphilic polymers or the creation of a phospholipid bilayer.[77,79] The good results achieved with such protocols regarding colloidal stability and UCL brightness demonstrate that amphiphilic approaches in general could be very promising and may be a good way to proceed with research to identify an ideal surface that works in a simple and reliable manner with sufficient protection of the UCNP from aggregation and water quenching.

Figure 1.8 summarizes the key parameters one has to face when designing UCNPs. Since the high goal of UCNP research is to make the particles more efficient and applicable for biological purposes, the question arises where the screws should be turned to get closer to this goal. Regarding particle architecture and composition, higher lanthanide concentrations seem to be a new promising trend. Since the exact effects of high lanthanide content on the luminescent properties of the particles have not yet been studied in detail and it is not clear whether this can be beneficial for biological applications with moderate power densities (compared to the already established particles), this topic needs to be investigated. Furthermore, there is great potential for improvement in the surface design of particles as this determines whether the UCNPs are suitable and accessible for biological systems at all. Amphiphilic strategies seem to be the most promising among the surface modifications, for which the development of a simple, inexpensive, and versatile method is highly demanded.
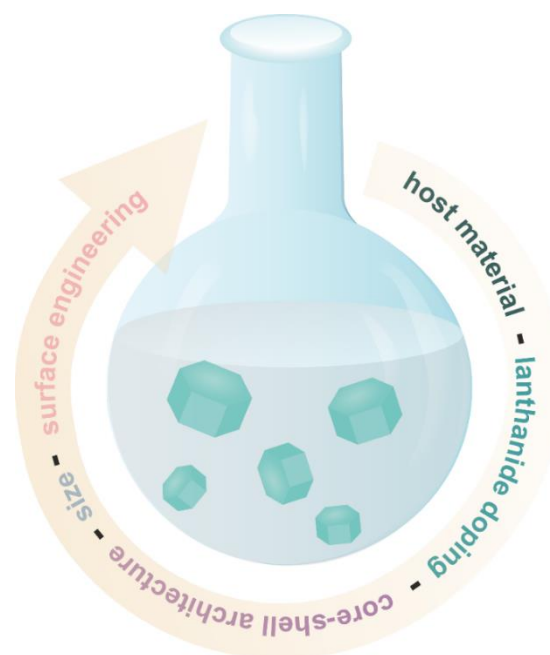

Figure 1.8. Different key steps in designing an upconversion nanoparticle.

1.4   References

[1] Frangioni, J. V. New Technologies for Human Cancer Imaging. *J. Clin. Oncol.* **2008**, *26* (24), 4012–4021. DOI: 10.1200/JCO.2007.14.3065.

[2] Ahlgrimm-Siess, V.; Laimer, M.; Rabinovitz, H. S.; Oliviero, M.; Hofmann-Wellenhof, R.; Marghoob, A. A.; Scope, A. Confocal Microscopy in Skin Cancer. *Curr. Dermatol. Rep.* **2018**, *7* (2), 105–118. DOI: 10.1007/s13671-018-0218-9.

[3] Tipirneni, K. E.; Rosenthal, E. L.; Moore, L. S.; Haskins, A. D.; Udayakumar, N.; Jani, A. H.; Carroll, W. R.; Morlandt, A. B.; Bogyo, M.; Rao, J.; Warram, J. M. Fluorescence Imaging for Cancer Screening and Surveillance. *Mol Imaging Biol* **2017**, *19* (5), 645–655. DOI: 10.1007/s11307-017-1050-5.

[4] Yu, Z.; Jiang, N.; Kazarian, S. G.; Tasoglu, S.; Yetisen, A. K. Optical Sensors for Continuous Glucose Monitoring. *Prog. Biomed. Eng.* **2021**, *3* (2), 22004. DOI: 10.1088/2516-1091/abe6f8.

[5] Bockholt, R.; Paschke, S.; Heubner, L.; Ibarlucea, B.; Laupp, A.; Janićijević, Ž.; Klinghammer, S.; Balakin, S.; Maitz, M. F.; Werner, C.; Cuniberti, G.; Baraban, L.; Spieth, P. M. Real-Time Monitoring of Blood Parameters in the Intensive Care Unit: State-of-the-Art and Perspectives. *J. Clin. Med.* **2022**, *11* (9), 2408. DOI: 10.3390/jcm11092408.

[6] Linsley, C. S.; Wu, B. M. Recent Advances in Light-responsive On-demand Drug-delivery Systems. *Ther. Deliv.* **2017**, *8* (2), 89–107. DOI: 10.4155/tde-2016-0060.

[7] Algorri, J. F.; Ochoa, M.; Roldán-Varona, P.; Rodríguez-Cobo, L.; López-Higuera, J. M. Photodynamic Therapy: A Compendium of Latest Reviews. *Cancers (Basel)* **2021**, *13* (17), 4447. DOI: 10.3390/cancers13174447.

[8] Tan, P.; He, L.; Huang, Y.; Zhou, Y. Optophysiology: Illuminating Cell Physiology with Optogenetics. *Physiol. Rev.* **2022**, *102* (3), 1263–1325. DOI: 10.1152/physrev.00021.2021.

[9] Najahi-Missaoui, W.; Arnold, R. D.; Cummings, B. S. Safe Nanoparticles: Are We There Yet? *Int. J. Mol. Sci.* **2020**, *22* (1), 385. DOI: 10.3390/ijms22010385.

[10] Huang, C.; Chen, X.; Xue, Z.; Wang, T. Effect of Structure: A New Insight Into Nanoparticle Assemblies from Inanimate to Animate. *Sci. Adv.* **2020**, *6* (20), eaba1321. DOI: 10.1126/sciadv.aba1321.

[11] Behzadi, S.; Serpooshan, V.; Tao, W.; Hamaly, M. A.; Alkawareek, M. Y.; Dreaden, E. C.; Brown, D.; Alkilany, A. M.; Farokhzad, O. C.; Mahmoudi, M. Cellular Uptake of Nanoparticles: Journey Inside the Cell. *Chem. Soc. Rev.* **2017**, *46* (14), 4218–4244. DOI: 10.1039/c6cs00636a.

[12] McNamara, K.; Tofail, S. A. M. Nanoparticles in Biomedical Applications. *Adv. Phys.: X* **2017**, *2* (1), 54–88. DOI: 10.1080/23746149.2016.1254570.

[13] Gelperina, S.; Kisich, K.; Iseman, M. D.; Heifets, L. The Potential Advantages of Nanoparticle Drug Delivery Systems in Chemotherapy of Tuberculosis. *Am. J. Respir. Crit. Care Med.* **2005**, *172* (12), 1487–1490. DOI: 10.1164/rccm.200504-613PP.

[14] Kremers, G.-J.; Gilbert, S. G.; Cranfill, P. J.; Davidson, M. W.; Piston, D. W. Fluorescent Proteins at a Glance. *J. Cell Sci.* **2011**, *124* (Pt 2), 157–160. DOI: 10.1242/jcs.072744.

[15] Xing, H.; Hwang, K.; Lu, Y. Recent Developments of Liposomes as Nanocarriers for Theranostic Applications. *Theranostics* **2016**, *6* (9), 1336–1352. DOI: 10.7150/thno.15464.

[16] Liu, Y.; Huang, H.; Cao, W.; Mao, B.; Liu, Y.; Kang, Z. Advances in Carbon Dots: From the Perspective of Traditional Quantum Dots. *Mater. Chem. Front.* **2020**, *4* (6), 1586–1613. DOI: 10.1039/D0QM00090F.

[17] Wang, W.; Damm, C.; Walter, J.; Nacken, T. J.; Peukert, W. Photobleaching and Stabilization of Carbon Nanodots Produced by Solvothermal Synthesis. *Phys. Chem. Chem. Phys.* **2016**, *18* (1), 466–475. DOI: 10.1039/c5cp04942c.

[18] Ash, C.; Dubec, M.; Donne, K.; Bashford, T. Effect of Wavelength and Beam Width on Penetration in Light-tissue Interaction Using Computational Methods. *Lasers Med. Sci.* **2017**, *32* (8), 1909–1918. DOI: 10.1007/s10103-017-2317-4.

[19] Jacques, S. L. Optical Properties of Biological Tissues: A Review. *Phys. Med. Biol.* **2013**, *58* (11), R37-61. DOI: 10.1088/0031-9155/58/11/R37.

[20] Finlayson, L.; Barnard, I. R. M.; McMillan, L.; Ibbotson, S. H.; Brown, C. T. A.; Eadie, E.; Wood, K. Depth Penetration of Light into Skin as a Function of Wavelength from 200 to 1000 nm. *Photochem. Photobiol.* **2022**, *98* (4), 974–981. DOI: 10.1111/php.13550.

[21] Cios, A.; Cieplak, M.; Szymański, Ł.; Lewicka, A.; Cierniak, S.; Stankiewicz, W.; Mendrycka, M.; Lewicki, S. Effect of Different Wavelengths of Laser Irradiation on the Skin Cells. *Int. J. Mol. Sci.* **2021**, *22* (5), 2437. DOI: 10.3390/ijms22052437.

[22] Haase, M.; Schäfer, H. Upconverting Nanoparticles. *Angew. Chem., Int. Ed.* **2011**, *50* (26), 5808–5829. DOI: 10.1002/anie.201005159.

[23] Bünzli, J.-C. G.; Mcgill, I. Rare Earth Elements. In *Ullmann's Encyclopedia of Industrial Chemistry;* Wiley, **2003**; pp 1–53. DOI: 10.1002/14356007.a22_607.pub2.

[24] Werts, M. H. V. Making Sense of Lanthanide Luminescence. *Sci. Prog.* **2005**, *88* (Pt 2), 101–131. DOI: 10.3184/003685005783238435.

[25] Fendler, W. P.; Rahbar, K.; Herrmann, K.; Kratochwil, C.; Eiber, M. 177Lu-PSMA Radioligand Therapy for Prostate Cancer. *J. Nucl. Med.* **2017**, *58* (8), 1196–1200. DOI: 10.2967/jnumed.117.191023.

[26] Zhang, Q.; O'Brien, S.; Grimm, J. Biomedical Applications of Lanthanide Nanomaterials, for Imaging, Sensing and Therapy. *Nanotheranostics* **2022**, *6* (2), 184–194. DOI: 10.7150/ntno.65530.

[27] Ogasawara, K.; Watanabe, S.; Toyoshima, H.; Brik, M. G. Chapter 231 First-principles Calculations of 4fn→4fn−15d Transition Spectra. In *Handbook on the Physics and Chemistry of Rare Earths*; Gschneidner, K. A., Bünzli, J.-C., Pecharsky, V. K., Eds.; Elsevier, **2007**; pp 1–59. DOI: 10.1016/S0168-1273(07)37031-1.

[28] Eliseeva, S. V.; Bünzli, J.-C. G. Lanthanide Luminescence for Functional Materials and Bio-sciences. *Chem. Soc. Rev.* **2010**, *39* (1), 189–227. DOI: 10.1039/B905604C.

[29] Bünzli, J.-C. G. Lanthanide Luminescence: From a Mystery to Rationalization, Understanding, and Applications. In *Handbook on the Physics and Chemistry of Rare Earths*; Gschneidner, K. A., Bünzli, J.-C., Pecharsky, V. K., Eds.; Elsevier, **2016**; 141–176. DOI: 10.1016/bs.hpcre.2016.08.003.

[30] Laporte, O.; Meggers, W. F. Some Rules of Spectral Structure*. *J. Opt. Soc. Am.* **1925**, *11* (5), 459. DOI: 10.1364/JOSA.11.000459.

[31] Tanner, P. A.; Zhou, L.; Duan, C.; Wong, K.-L. Misconceptions in Electronic Energy Transfer: Bridging the Gap Between Chemistry and Physics. *Chem. Soc. Rev.* **2018**, *47* (14), 5234–5265. DOI: 10.1039/c8cs00002f.

[32] Shavaleev, N. M.; Eliseeva, S. V.; Scopelliti, R.; Bünzli, J.-C. G. Influence of Symmetry on the Luminescence and Radiative Lifetime of Nine-coordinate Europium Complexes. *Inorg. Chem.* **2015**, *54* (18), 9166–9173. DOI: 10.1021/acs.inorgchem.5b01580.

[33] Shin, S. H.; Kang, J. H.; Jeon, D. Y.; Sik Zang, D. Enhancement of Cathodoluminescence Intensities of Y_2O_3:Eu and Gd_2O_3:Eu Phosphors by Incorporation of Li Ions. *J. Lumin.* **2005**, *114* (3-4), 275–280. DOI: 10.1016/j.jlumin.2005.02.002.

[34] Auzel, F. History of Upconversion Discovery and its Evolution. *J. Lumin.* **2020**, *223*, 116900. DOI: 10.1016/j.jlumin.2019.116900.

[35] Wang, F.; Liu, X. Rare-Earth Doped Upconversion Nanophosphors. In *Comprehensive nanoscience and technology*; Adrews, D. L., Scholes, G. D., Wiederrecht, G. P., Eds.; Elsevier, **2011**; 607–635. DOI: 10.1016/B978-0-12-374396-1.00146-X.

[36] Auzel, F. Upconversion and Anti-Stokes Processes with f and d Ions in Solids. *Chem. Rev.* **2004**, *104* (1), 139–173. DOI: 10.1021/cr020357g.

[37] Bednarkiewicz, A.; Chan, E. M.; Kotulska, A.; Marciniak, L.; Prorok, K. Photon Avalanche in Lanthanide Doped Nanoparticles for Biomedical Applications: Super-resolution Imaging. *Nanoscale Horiz.* **2019**, *4* (4), 881–889. DOI: 10.1039/C9NH00089E.

[38] Wang, F.; Liu, X. Upconversion Multicolor Fine-tuning: Visible to Near-infrared Emission from Lanthanide-doped $NaYF_4$ Nanoparticles. *J. Am. Chem. Soc.* **2008**, *130* (17), 5642–5643. DOI: 10.1021/ja800868a.

[39] Zheng, K.; Loh, K. Y.; Wang, Y.; Chen, Q.; Fan, J.; Jung, T.; Nam, S. H.; Suh, Y. D.; Liu, X. Recent Advances in Upconversion Nanocrystals: Expanding the Kaleidoscopic Toolbox for Emerging Applications. *Nano Today* **2019**, *29*, 100797. DOI: 10.1016/j.nantod.2019.100797.

[40] Hemmer, E.; Benayas, A.; Légaré, F.; Vetrone, F. Exploiting the Biological Windows: Current Perspectives on Fluorescent Bioprobes Emitting Above 1000 nm. *Nanoscale Horiz.* **2016**, *1* (3), 168–184. DOI: 10.1039/C5NH00073D.

[41] Chen, G.; Qiu, H.; Prasad, P. N.; Chen, X. Upconversion Nanoparticles: Design, Nanochemistry, and Applications in Theranostics. *Chem. Rev.* **2014**, *114* (10), 5161–5214. DOI: 10.1021/cr400425h.

[42] Würth, C.; Fischer, S.; Grauel, B.; Alivisatos, A. P.; Resch-Genger, U. Quantum Yields, Surface Quenching, and Passivation Efficiency for Ultrasmall Core/Shell Upconverting Nanoparticles. *J. Am. Chem. Soc.* **2018**, *140* (14), 4922–4928. DOI: 10.1021/jacs.8b01458.

[43] Teitelboim, A.; Tian, B.; Garfield, D. J.; Fernandez-Bravo, A.; Gotlin, A. C.; Schuck, P. J.; Cohen, B. E.; Chan, E. M. Energy Transfer Networks within Upconverting Nanoparticles Are Complex Systems with Collective, Robust, and History-Dependent Dynamics. *J. Phys. Chem. C* **2019**, *123* (4), 2678–2689. DOI: 10.1021/acs.jpcc.9b00161.

[44] Zheng, W.; Zhu, H.; Li, R.; Tu, D.; Liu, Y.; Luo, W.; Chen, X. Visible-to-infrared Quantum Cutting by Phonon-assisted Energy Transfer in YPO_4:Tm^{3+}, Yb^{3+} Phosphors. *Phys. Chem. Chem. Phys.* **2012**, *14* (19), 6974–6980. DOI: 10.1039/c2cp24044k.

[45] Taylor, E. R.; Ng, L. N.; Sessions, N. P.; Buerger, H. Spectroscopy of Tm^{3+}-doped Tellurite Glasses for 1470 nm Fiber Amplifier. *J. Appl. Phys.* **2002**, *92* (1), 112–117. DOI: 10.1063/1.1483391.

[46] Shan, J.; Kong, W.; Wei, R.; Yao, N.; Ju, Y. An Investigation of the Thermal Sensitivity and Stability of the β-NaYF$_4$:Yb,Er Upconversion Nanophosphors. *J. Appl. Phys.* **2010**, *107* (5), 54901. DOI: 10.1063/1.3298905.

[47] Gao, G.; Turshatov, A.; Howard, I. A.; Busko, D.; Joseph, R.; Hudry, D.; Richards, B. S. Up-Conversion Fluorescent Labels for Plastic Recycling: A Review. *Adv. Sustainable Syst.* **2017**, *1* (5), 1600033. DOI: 10.1002/adsu.201600033.

[48] Pi, D.; Wang, F.; Fan, X.; Wang, M.; Zhang, Y. Luminescence Behavior of Eu^{3+} Doped LaF$_3$ Nanoparticles. *Spectrochim. Acta A Mol. Biomol. Spectrosc.* **2005**, *61* (11-12), 2455–2459. DOI: 10.1016/j.saa.2004.09.009.

[49] Soga, K.; Wang, W.; Riman, R. E.; Brown, J. B.; Mikeska, K. R. Luminescent Properties of Nanostructured Dy^{3+}- and Tm^{3+}-Doped Lanthanum Chloride Prepared by Reactive Atmosphere Processing of Sol-gel Derived Lanthanum Hydroxide. *J. Appl. Phys.* **2003**, *93* (5), 2946–2951. DOI: 10.1063/1.1540229.

[50] Gulzar, A.; Xu, J.; Yang, P.; He, F.; Xu, L. Upconversion Processes: Versatile Biological Applications and Biosafety. *Nanoscale* **2017**, *9* (34), 12248–12282. DOI: 10.1039/c7nr01836c.

[51] Liang, G.; Wang, H.; Shi, H.; Wang, H.; Zhu, M.; Jing, A.; Li, J.; Li, G. Recent Progress in the Development of Upconversion Nanomaterials in Bioimaging and Disease Treatment. *J. Nanobiotechnol.* **2020**, *18* (1), 154. DOI: 10.1186/s12951-020-00713-3.

[52] Naccache, R.; Yu, Q.; Capobianco, J. A. The Fluoride Host: Nucleation, Growth, and Upconversion of Lanthanide-Doped Nanoparticles. *Adv. Opt. Mater.* **2015**, *3* (4), 482–509. DOI: 10.1002/adom.201400628.

[53] Misiak, M.; Pavlosiuk, O.; Szalkowski, M.; Kotulska, A.; Ledwa, K.; Bednarkiewicz, A. On the Role of Gd^{3+} ions in Enhancement of UV Emission from Yb^{3+}-Tm^{3+}Up-converting LiYF$_4$ Nanocrystals. *Nanotechnology* **2023**, *34* (34). DOI: 10.1088/1361-6528/acd701.

[54] Zhu, X.; Zhang, J.; Liu, J.; Zhang, Y. Recent Progress of Rare-Earth Doped Upconversion Nanoparticles: Synthesis, Optimization, and Applications. *Adv. Sci.* **2019**, *6* (22), 1901358. DOI: 10.1002/advs.201901358.

[55] Li, Z.; Zhang, Y.; Jiang, S. Multicolor Core/Shell‐Structured Upconversion Fluorescent Nanoparticles. *Adv. Mater.* **2008**, *20* (24), 4765–4769. DOI: 10.1002/adma.200801056.

[56] Boyer, J.-C.; Vetrone, F.; Cuccia, L. A.; Capobianco, J. A. Synthesis of Colloidal Upconverting NaYF$_4$ Nanocrystals Doped with Er^{3+}, Yb^{3+} and Tm^{3+}, Yb^{3+} via Thermal Decomposition of Lanthanide Trifluoroacetate Precursors. *J. Am. Chem. Soc.* **2006**, *128* (23), 7444–7445. DOI: 10.1021/ja061848b.

[57] Shan, J.; Ju, Y. A Single-step Synthesis and the Kinetic Mechanism for Monodisperse and Hexagonal-phase NaYF$_4$:Yb,Er Upconversion Nanophosphors. *Nanotechnology* **2009**, *20* (27), 275603. DOI: 10.1088/0957-4484/20/27/275603.

[58] Wiesholler, L. M.; Genslein, C.; Schroter, A.; Hirsch, T. Plasmonic Enhancement of NIR to UV Upconversion by a Nanoengineered Interface Consisting of NaYF$_4$:Yb,Tm Nanoparticles and a Gold Nanotriangle Array for Optical Detection of Vitamin B12 in Serum. *Anal. Chem.* **2018**, *90* (24), 14247–14254. DOI: 10.1021/acs.analchem.8b03279.

[59] Rafique, R.; Baek, S. H.; Le Phan, M. T.; Chang, S.-J.; Gul, A. R.; Park, T. J. A Facile Hydrothermal Synthesis of Highly Luminescent NaYF$_4$:Yb^{3+}/Er^{3+} Upconversion Nanoparticles and their Biomonitoring Capability. *Mater. Sci. Eng. C* **2019**, *99*, 1067–1074. DOI: 10.1016/j.msec.2019.02.046.

[60] Jiao, Y.; Ling, C.; Wang, J.-X.; Amanico, H.; Saczek, J.; Wang, H.; Sridhar, S.; Xu, B. B.; Wang, S.; Wang, D. Controllable Synthesis of Upconversion Nanophosphors toward Scale‐Up Productions. *Part. Part. Syst. Charact.* **2020**, *37* (9), 2000129. DOI: 10.1002/ppsc.202000129.

[61] Wang, H.-Q.; Nann, T. Monodisperse Upconverting Nanocrystals by Microwave-Assisted Synthesis. *ACS Nano* **2009**, *3* (11), 3804–3808. DOI: 10.1021/nn9012093.

[62] Nannuri, S. H.; Singh, S.; Misra, S. K.; C, S.; George, S. D. Microwave-assisted Synthesis and Upconversion Luminescence of NaYF$_4$:Yb, Gd, Er and NaYF$_4$:Yb, Gd, Tm Nanorods. *Methods Appl. Fluoresc.* **2022**, *10* (2), 024004. DOI: 10.1088/2050-6120/ac58e6.

[63] Wang, H.; Yi, Z.; Rao, L.; Liu, H.; Zeng, S. High Quality Multi-functional NaErF$_4$ Nanocrystals: Structure-controlled Synthesis, Phase-induced Multi-color Emissions and Tunable Magnetic Properties. *J. Mater. Chem. C* **2013**, *1* (35), 5520. DOI: 10.1039/c3tc30796d.

[64] Hudry, D.; Howard, I. A.; Popescu, R.; Gerthsen, D.; Richards, B. S. Structure-Property Relationships in Lanthanide-Doped Upconverting Nanocrystals: Recent Advances in Understanding Core-Shell Structures. *Adv. Mater.* **2019**, *31* (26), e1900623. DOI: 10.1002/adma.201900623.

[65] Liu, D.; Xu, X.; Du, Y.; Qin, X.; Zhang, Y.; Ma, C.; Wen, S.; Ren, W.; Goldys, E. M.; Piper, J. A.; Dou, S.; Liu, X.; Jin, D. Three-dimensional Controlled Growth of Monodisperse Sub-50 nm Heterogeneous Nanocrystals. *Nat. Commun.* **2016**, *7*, 10254. DOI: 10.1038/ncomms10254.

[66] Wen, S.; Zhou, J.; Zheng, K.; Bednarkiewicz, A.; Liu, X.; Jin, D. Advances in Highly Doped Upconversion Nanoparticles. *Nat. Commun.* **2018**, *9* (1), 2415. DOI: 10.1038/s41467-018-04813-5.

[67] Wiesholler, L. M.; Frenzel, F.; Grauel, B.; Würth, C.; Resch-Genger, U.; Hirsch, T. Yb,Nd,Er-doped Upconversion Nanoparticles: 980 nm Versus 808 nm Excitation. *Nanoscale* **2019**, *11* (28), 13440–13449. DOI: 10.1039/c9nr03127h.

[68] Vetrone, F.; Naccache, R.; Mahalingam, V.; Morgan, C. G.; Capobianco, J. A. The Active-Core/Active-Shell Approach: A Strategy to Enhance the Upconversion Luminescence in Lanthanide-doped Nanoparticles. *Adv. Funct. Mater.* **2009**, *19* (18), 2924–2929. DOI: 10.1002/adfm.200900234.

[69] Tessitore, G.; Mandl, G. A.; Brik, M. G.; Park, W.; Capobianco, J. A. Recent Insights Into Upconverting Nanoparticles: Spectroscopy, Modeling, and Routes to Improved Luminescence. *Nanoscale* **2019**, *11* (25), 12015–12029. DOI: 10.1039/c9nr02291k.

[70] Kraft, M.; Würth, C.; Muhr, V.; Hirsch, T.; Resch-Genger, U. Particle-size-dependent Upconversion Luminescence of NaYF$_4$: Yb, Er Nanoparticles in Organic Solvents and Water at Different Excitation Power Densities. *Nano Res.* **2018**, *11* (12), 6360–6374. DOI: 10.1007/s12274-018-2159-9.

[71] Cheng, T.; Marin, R.; Skripka, A.; Vetrone, F. Small and Bright Lithium-based Upconverting Nanoparticles. *J. Am. Chem. Soc.* **2018**, *140* (40), 12890–12899. DOI: 10.1021/jacs.8b07086.

[72] Lin, H.; Xu, D.; Cheng, Z.; Li, Y.; Xu, L.; Ma, Y.; Yang, S.; Zhang, Y. Small-sized Red-emitting Core/shell/shell Nanoparticles Nhrough an Efficient Energy Back Transfer Process. *Appl. Surf. Sci.* **2020**, *514*, 146074. DOI: 10.1016/j.apsusc.2020.146074.

[73] Gargas, D. J.; Chan, E. M.; Ostrowski, A. D.; Aloni, S.; Altoe, M. V. P.; Barnard, E. S.; Sanii, B.; Urban, J. J.; Milliron, D. J.; Cohen, B. E.; Schuck, P. J. Engineering Bright Sub-10-nm Upconverting Nanocrystals for Single-molecule Imaging. *Nat. Nanotechnol.* **2014**, *9* (4), 300–305. DOI: 10.1038/nnano.2014.29.

[74] Zhao, C.; Kong, X.; Liu, X.; Tu, L.; Wu, F.; Zhang, Y.; Liu, K.; Zeng, Q.; Zhang, H. Li$^+$ Ion Doping: An Approach for Improving the Crystallinity and Upconversion Emissions of NaYF$_4$:Yb^{3+}, Tm^{3+} Nanoparticles. *Nanoscale* **2013**, *5* (17), 8084–8089. DOI: 10.1039/c3nr01916k.

[75] Shrestha, S.; Wang, B.; Dutta, P. Nanoparticle Processing: Understanding and Controlling Aggregation. *Adv. Colloid Interface Sci.* **2020**, *279*, 102162. DOI: 10.1016/j.cis.2020.102162.

[76] Lazzari, S.; Moscatelli, D.; Codari, F.; Salmona, M.; Morbidelli, M.; Diomede, L. Colloidal Stability of Polymeric Nanoparticles in Biological Fluids. *J. Nanopart. Res.* **2012**, *14* (6), 920. DOI: 10.1007/s11051-012-0920-7.

[77] Märkl, S.; Schroter, A.; Hirsch, T. Small and Bright Water-Protected Upconversion Nanoparticles with Long-time Stability in Complex, Aqueous Media by Phospholipid Membrane Coating. *Nano Lett.* **2020**, *20* (12), 8620–8625. DOI: 10.1021/acs.nanolett.0c03327.

[78] Wilhelm, S.; Kaiser, M.; Würth, C.; Heiland, J.; Carrillo-Carrion, C.; Muhr, V.; Wolfbeis, O. S.; Parak, W. J.; Resch-Genger, U.; Hirsch, T. Water Dispersible Upconverting Nanoparticles: Effects of Surface Modification on their Luminescence and Colloidal Stability. *Nanoscale* **2015**, *7* (4), 1403–1410. DOI: 10.1039/c4nr05954a.

[79] Plohl, O.; Kralj, S.; Majaron, B.; Fröhlich, E.; Ponikvar-Svet, M.; Makovec, D.; Lisjak, D. Amphiphilic Coatings for the Protection of Upconverting Nanoparticles Against Dissolution in Aqueous Media. *Dalton Trans.* **2017**, *46* (21), 6975–6984. DOI: 10.1039/c7dt00529f.

[80] Del Rosal, B.; Jaque, D. Upconversion Nanoparticles for in Vivo Applications: Limitations and Future Perspectives. *Methods Appl. Fluoresc.* **2019**, *7* (2), 22001. DOI: 10.1088/2050-6120/ab029f.

[81] Stetefeld, J.; McKenna, S. A.; Patel, T. R. Dynamic Light Scattering: A Practical Guide and Applications in Biomedical Sciences. *Biophys. Rev.* **2016**, *8* (4), 409–427. DOI: 10.1007/s12551-016-0218-6.

[82] Delgado, A. V.; González-Caballero, F.; Hunter, R. J.; Koopal, L. K.; Lyklema, J. Measurement and Interpretation of Electrokinetic Phenomena. *J. Colloid Interface Sci.* **2007**, *309* (2), 194–224. DOI: 10.1016/j.jcis.2006.12.075.

[83] Raval, N.; Maheshwari, R.; Kalyane, D.; Youngren-Ortiz, S. R.; Chougule, M. B.; Tekade, R. K. Importance of Physicochemical Characterization of Nanoparticles in Pharmaceutical Product Development. In *Basic Fundamentals of Drug Delivery*; Elsevier, **2019**; pp 369–400. DOI: 10.1016/B978-0-12-817909-3.00010-8.

[84] Zhu, X.; Zhang, H.; Zhang, F. Ligand-Based Surface Engineering of Lanthanide Nanoparticles for Bioapplications. *ACS Materials Lett.* **2022**, *4* (9), 1815–1830. DOI: 10.1021/acsmaterialslett.2c00528.

2 Motivation and Aim of the Work

The potential of upconversion nanoparticles (UCNPs) in biomedical applications is significant, however, their limited brightness poses a challenge. Thus, improving upconversion efficiency is a key goal. Previous research kept lanthanide concentrations low to avoid quenching effects, but recent studies suggest that increasing sensitizer and activator doping could be beneficial. However, the impact of this increased doping on the energetic processes within the particles remains poorly investigated, yet crucial for optimizing UCNPs. Therefore, in this thesis, various UCNPs with high Yb^{3+} and Er^{3+} content will be synthesized, characterized, and compared to particles with low doping. The brightness of UCNPs is not the only challenge; their strong tendency to aggregate in biological environments must be stopped to make them attractive for medical applications. Surface engineering plays a vital role in addressing this issue by designing precise surface coatings that ensure colloidal stability, minimize water quenching effects, and enable further functionalization with molecules such as dyes or receptors. Although no ultimate strategy exists for achieving good surface protection and functionalization, amphiphilic surface coatings are promising. Addressing those challenges by developing a simple method for surface design is an objective of this thesis so that eventually bright, colloidal stable, and functional particles are obtained by a combination of thoughtful particle design with precise surface engineering (Figure 2.1).
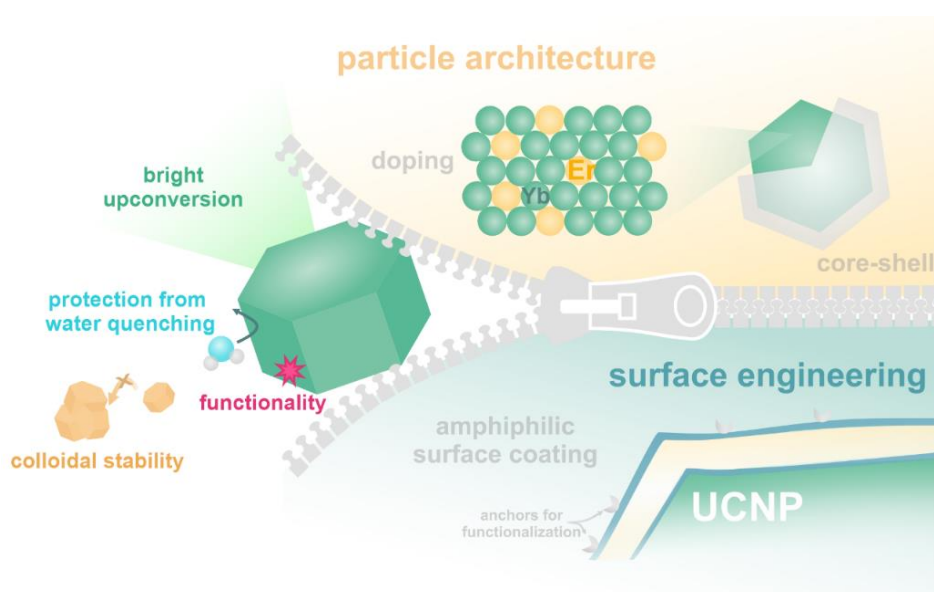

Figure 2.1. Bright upconversion, colloidal stability, and functionality achieved by combination of improved particle architecture and precise surface engineering.

3 Upconversion Nanocrystals with High Lanthanide Content: Luminescence Loss by Energy Migration versus Luminescence Enhancement by Increased NIR Absorption

3.1 Abstract

Lanthanide-doped upconversion nanoparticles (UCNPs) have attracted a lot of interest due to their benefits in biological applications: They are not suffering from intermittence and provide nearly background free luminescence. The progress in synthesis nowadays enables access to complex core-shell particles of controlled size and composition. Nevertheless, the frequently used doping ratio dates back where mostly core-only particles of relatively large size have been studied. Especially at low power excitation as needed in biology, a decrease in particle size leads to a drastically decrease in the upconversion efficiency. An enhancement strategy based on an increased absorption-rate of NIR light provided by an increase of the sensitizer content, together with the simultaneous blocking of the energy migration pathways to the particle surface is presented. $NaYbF_4(20\%Er)$ particles of 8.5 nm in diameter equipped with an about 2 nm thick $NaYF_4$ shell show significantly enhanced upconversion luminescence in the red (660 nm) when compared to the most common used particles with only 20% Yb^{3+} and 2% Er^{3+}. The impact of size, the composition, and the core-shell architecture on the photophysical properties was studied. The findings demonstrate that an increase in doping rates enables the design of small, bright UCNPs useful for biological applications.

3.2 Introduction

Luminescent probes have established themselves as important reporters in biosensing and biomedicine, including organic dyes, fluorescent proteins, metal complexes, and semiconductor quantum dots. One promising class of luminescent probes are upconversion nanoparticles (UCNPs), which can overcome some drawbacks of common fluorophores. Those lanthanide-based nanocrystals absorb near-infrared (NIR) light and convert it into higher-energy visible or ultraviolet (UV) light.[6–9] Since the excitation lies in a wavelength range, where scattering and autofluorescence of biomolecules are very low, UCNPs allow deep tissue penetration and have the benefit of high signal-to-noise ratios additional to their photostability and sharp and tunable emission bands.[10,11] The nanocrystals usually include a sensitizer – activator pair of lanthanide ions doped inside an $NaYF_4$ host lattice. The sensitizer absorbs NIR excitation light, transfers the energy of one, two or three photons to the activator, which subsequently emits the upconversion luminescence.[12,13] Many applications require strong upconversion to achieve high signal intensities and to keep the amount of nanoparticles in the organism low, which is why high efficiency of the upconversion process is probably the most important issue when UCNPs are designed for biological applications.[14,15] Several strategies such as energy harvesting, plasmonic enhancement, or triplet excited states in order to improve the upconversion efficiency were already discussed in the literature.[16–23] One essential strategy is the protection of the lanthanide ions from the environment by passivating the nanoparticle surface with a non-doped $NaYF_4$ shell. High energy vibrations of ligand or solvent molecules as well as crystal lattice defects, changing the local field around the lanthanides, lead to non-radiative decay processes that reduce the luminescence intensity.[24] As shell growth enlarges the distance between the lanthanides and surface quenchers, strong increases of luminescence intensities and quantum yields can be achieved.[24,25]

To increase the upconversion efficiencies one should also reconsider the content of sensitizer and activator ions. For many years (or decades), low doping of lanthanide ions inside nanocrystals was believed the best for efficient upconversion luminescence. To achieve green upconversion luminescence, the lanthanide doping inside a $NaYF_4$ crystal was once optimized to 18% Yb^{3+} (sensitizer ion) and 2% Er^{3+} (activator ion).[13] The reason for the relative low lanthanide concentrations is the theory of concentration quenching, where higher concentrations of lanthanide dopants lead to cross-relaxations between the ions as well as energy migration to surface quenchers – and hence reduced upconversion emission intensities.[26,27] Even

if the optimized composition was proposed for powders with crystals in the micrometer-range, these concentrations are still prominent for nanoparticle dispersions with diameters < 50 nm,[26] where non-radiative decay processes on the surface become dominant, resulting in low upconversion efficiency.[28] To compensate for the loss of luminescence caused by quenching processes, strategies emerged to increase the absorption cross-sections of the particles through higher lanthanide doping.[29] It was found that concentration quenching can be overcome by high excitation power densities since cross relaxation and energy migration processes are hindered when all lanthanide ions are in excited state.[27] Increasing the activator concentration with constant sensitizer concentration was demonstrated to lead to improved luminescence intensities.[30,31] Similar results were achieved by increasing the Yb^{3+} concentration, where it was discovered that the higher the Yb^{3+} content, the higher are the luminescence intensities. High excitation power densities should be avoided for applications in living organisms,[32] therefore it was an significant step when it was discovered, that not only high excitation power densities enable high lanthanide doping but also inert shell growth around the particles, what protects them from energy migration to surface quenchers.[33–36] Core-shell structures with high lanthanide content were synthesized,[37–39] which all showed improved luminescence intensities compared to similar particle architectures with lower lanthanide doping. One very promising approach was the synthesis of so-called "alloyed" nanocrystals by Cohen *et al.*, where different Yb/Er ratios in a sodium lanthanide fluoride lattice equipped with an $NaYF_4$(20%Gd) shell were monitored at different power densities.[40] They introduced alloyed UCNPs for low irradiance imaging, only composed of $NaYbF_4$ and $NaErF_4$ without the need of $NaYF_4$ as host lattice.

Enhancing the absorption of UCNPs is clearly beneficial for the upconversion performance, but higher lanthanide doping also facilitates energy transfer processes between the single ions due to decreasing ion-ion distances.[41] While on the one hand energy migration can be useful, *e.g.* for the transportation of energy across core-shell interfaces,[42–49] it can on the other hand strongly limit upconversion intensities. For example, $NaErF_4$ nanoparticles suffer from low luminescence intensities if they are not equipped with an $NaYF_4$ shell since the energy migrates through the crystal lattice until it gets quenched on the particle surface.[35,50–53] The reduction of upconversion efficiency due to energy migration followed by surface quenching is an issue which should be valid for all systems with high concentrations of lanthanide ions. Consequently, it's unavoidable to get control over the energy migration and hinder the quenching processes to achieve bright luminescence.

Within this publication, the two main impacts of high lanthanide content in UCNPs will be discussed: higher absorption cross-sections on the one hand and increased energy migration between the lanthanide ions on the other hand. Ytterbium as sensitizer and erbium as activator ions were chosen to enable the energy transfer upconversion process (Figure 3.1a) leading to luminescence emissions in the green and red range of the electromagnetic spectrum, attractive for a broad variety of applications in biosensing and theranostics.[54–56] For this, core-shell nanoparticles with high sensitizer and activator content were synthesized. Those UCNPs consist of β-NaYbF$_4$(20%Er) equipped with NaYF$_4$. Inspired by the approach of Cohen *et al.*,[40] who used similar particles for low-irradiance imaging, those particles are referred to as *alloyed* UCNPs, whereas reference particles based on β-NaYF$_4$ doped with 20% Yb^{3+} and 2% Er^{3+} are titled as *doped* UCNPs (Figure 3.1b). The influence of nanoparticle size and the surface passivation effect depending on the shell material and shell thickness will be thoroughly discussed to give an insight on what parameters are important during particle design.
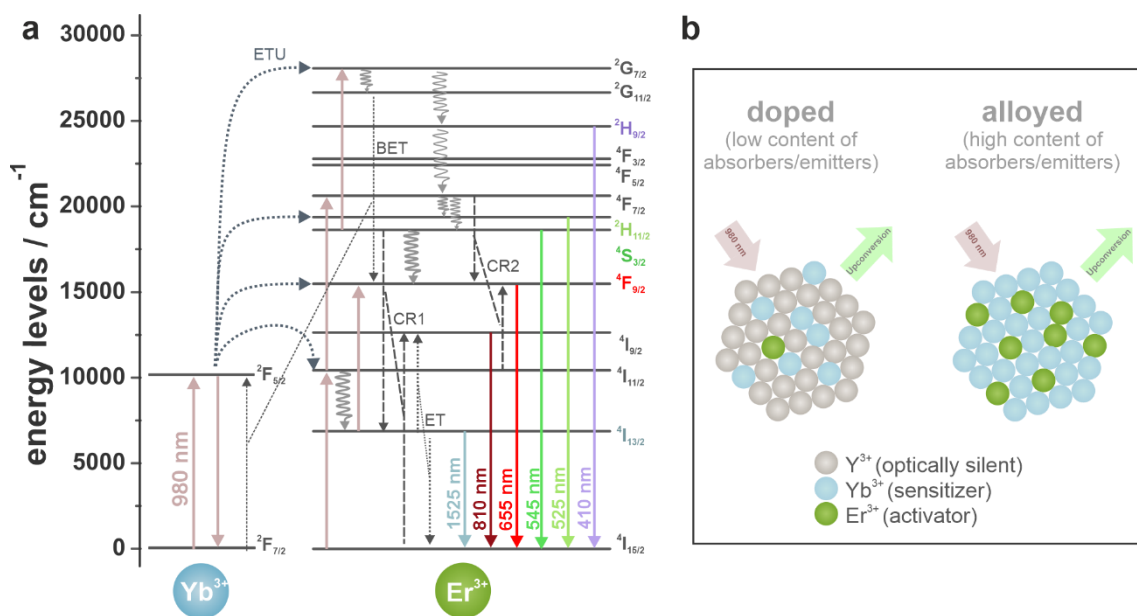

Figure 3.1. (a) Energy level diagram of Yb^{3+} and Er^{3+} ions inside an upconversion nanocrystal. Wavenumbers of the electronic states are from Reference [57]. ETU: energy transfer upconversion, BET: back energy transfer and CR: cross relaxations. Curly arrows indicate non-radiative decay processes. (b) Schematic representation of nanocrystals with high lanthanide content vs low lanthanide content (*alloyed* vs. *doped*).

3.3 Results and Discussion

Enhancing the lanthanide content inside the UCNPs brings one obvious advantage in contrast to low-doped UCNPs: the high number of sensitizer ions is accompanied by a higher absorption of the excitation light. Comparing small alloyed β-NaYbF$_4$(20%Er) (diameter: 8.5 ± 1.2 nm, Figure 3.2a) and doped β-NaYF$_4$(20%Yb,2%Er) (diameter: 7.6 ± 1.2 nm, Figure S3.5) nanoparticles, one finds absorption cross-sections about six times higher for alloyed compared to doped particles (Figure S3.1a). The slightly larger alloyed particles contain about 5.6 times more Yb^{3+} ions, and 14 times more Er^{3+} ions, which are both capable of absorbing 976 nm light. Since the absorption coefficient of Yb^{3+} is one order of magnitude higher compared to Er^{3+} at 976 nm, the amount of sensitizer is mainly responsible for the difference.[58] In contrast to the high absorption cross-section, upconversion luminescence (UCL) of alloyed UCNPs without a protective shell of NaYF$_4$ revealed a very low brightness (Figure 3.2b and c). The doped UCNPs, which have an about six times less absorption cross-section, show an about 50 times brighter UCL, which emphasizes that high absorption does not necessarily lead to high emission intensity. In contrast, after equipping the alloyed nanoparticles with an approximately 2 nm thin NaYF$_4$ shell, a remarkable luminescence enhancement of a factor of ~ 100,000 was found (integration between 400 - 750 nm).

The intense luminescence of the alloyed core-shell particles is contradictory to the concentration quenching theory, which says that cross-relaxations and energy migration between lanthanide ions in proximity are responsible for low luminescence emissions (Figure 3.2d). The strong impact of surface passivation in core-shell systems on the luminescence intensity leads to the conclusion that cross-relaxation cannot be the main reason for low brightness of the core particles, as the shell has no influence on the cross-relaxation processes between the Er^{3+} ions. In contrast, the concept of energy migration between the lanthanide ions is very plausible: One ion in excited state can transfer the energy to a second ion in ground state, from where again energy is transferred to the next ion. In this way, energy migrates until the surface of the nanoparticle is reached, where surface quenching deactivates the excited lanthanide ion before the upconversion luminescence is emitted. In case of core-shell architecture, the shell shields the particle from the environment and therefore inhibits the last step of energy transfer to quencher molecules, which enables the Er^{3+} ions to emit the upconversion luminescence.
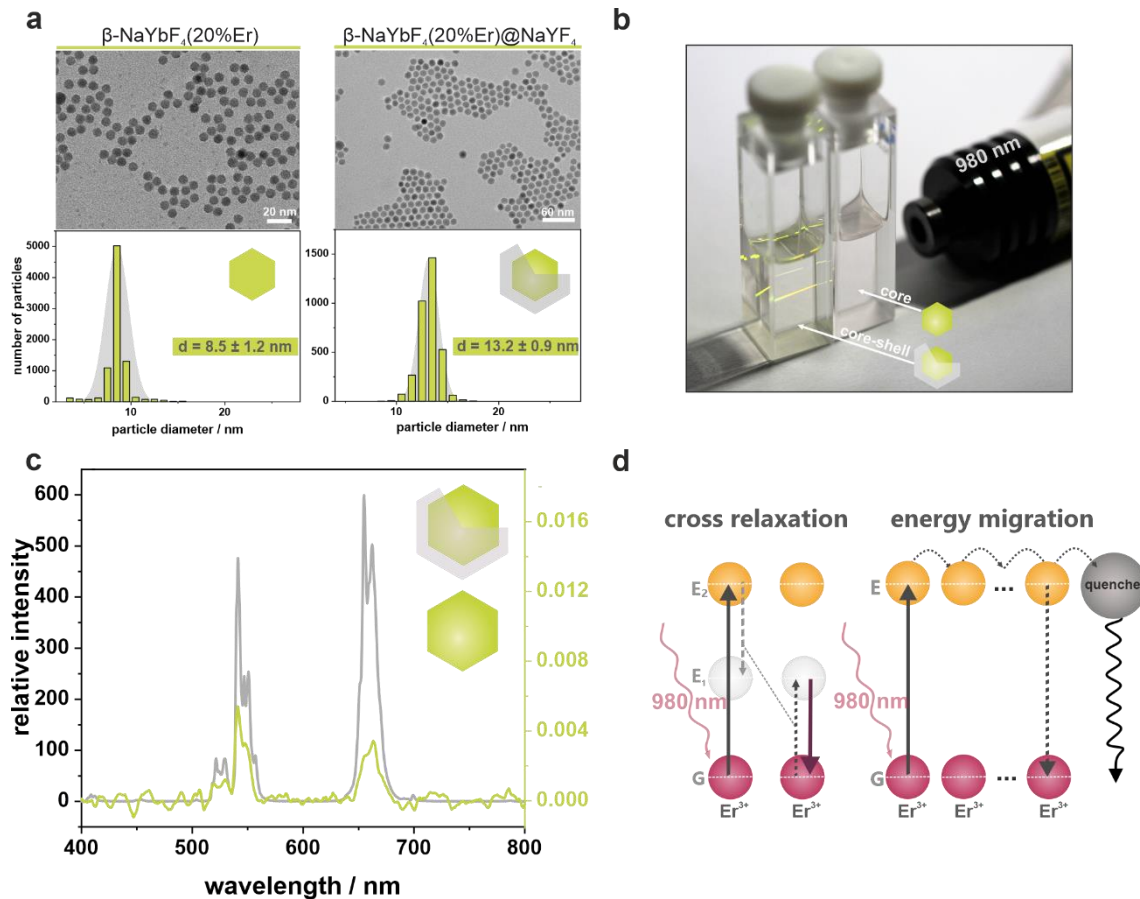
Figure 3.2. (a) TEM micrographs of alloyed core (β-NaYbF$_4$(20%Er)) and core-shell (β-NaYbF$_4$(20%Er)@NaYF$_4$) particles with corresponding size histograms. (b) Alloyed core (right) and core-shell (left) particles dispersed in cyclohexane, illuminated with 980 nm laser (200 mW, cw) in quartz cuvettes. (c) Luminescence comparison of core and core-shell particles at 980 nm irradiation with 140 W·cm^{-2}, spectra are normalized to particle concentration [particles·mL^{-1}] and measured in cyclohexane. (d) Schema of cross-relaxation and energy migration processes between lanthanide ions.

Ytterbium as well as erbium ions are both enabling energy migration. In the alloyed particle system, the number of ions was significantly increased in contrast to conventional doped particles (factor 4 for Yb^{3+}, factor 10 for Er^{3+} for particles with the same size). Since the Yb^{3+} content is already high for doped particles (20%), it can be assumed that the Er^{3+} ions are mainly responsible for the enormous loss of energy for alloyed core-only systems. To prove this hypothesis, two core-shell structures have been synthesized: β-NaYbF$_4$(20%Er)@NaYbF$_4$ and β-NaYbF$_4$(20%Er)@NaErF$_4$ (Figure 3.3a). If one of the lanthanide ions in the shell does not favor energy migration, brighter UCL will be expected similar to the passivation effect known from NaYF$_4$ shells. The luminescence spectra of those particles and the corresponding core particles reveal the effect of the two kinds of shells (Figure 3.3b). An Er-shell has no significant effect on the luminescence since integration over the visible range (400-750 nm) led to an enhancement factor of 1.8 compared to the core particles, both very close to the noise. These results confirm that the Er^{3+} ions promote the energy

to migrate through the shell without a barrier ending up in non-radiative deactivation at the particle surface or at crystal defects.
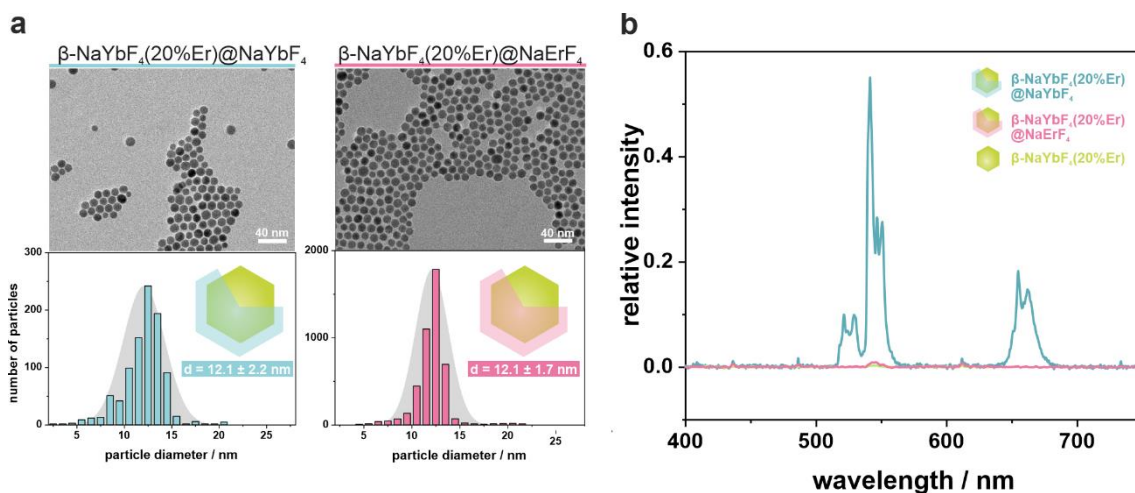

Figure 3.3. (a) TEM micrographs of β-NaYbF$_4$(20%Er)@NaYbF$_4$ and β-NaYbF$_4$(20%Er)@NaErF$_4$ core-shell nanoparticles with corresponding size histograms. (b) Luminescence of core and core-shell particles. Core particles are 8.5 ± 1.2 nm in diameter (see Figure 3.2a). Spectra are recorded at 980 nm excitation with 140 W·cm^{-2} (cw) and normalized to particle concentration [particles·mL^{-1}] in cyclohexane.

Quenching effects by the solvent cannot explain the very low luminescence intensities of the Er-shelled particles, as an H/D exchange in the solvent leads only to an enhancement of approximately factor 5 (Figure S3.2a). Therefore, quenching at crystal defects seems to be the more probable deactivation pathway. For the Yb^{3+} shell one would expect a luminescence enhancement independently from blocking energy migration, as about four times more Yb^{3+} ions are implemented into the particle, which would lead to an about four times higher absorption cross-section and therefore – in a simplified, ideal case – about four times higher luminescence. In fact, a strong luminescence enhancement by a factor of 51 was found for the Yb-shell. Surprisingly, the influence of non-radiative deactivation by C-H quenching of the solvent is comparable to the particles with NaErF$_4$ shell. The ^{2}F$_{5/2}$ level is not known to be influenced by C-H-vibrations[36], but an H/D exchange in the solvent leads to an enhancement factor of 4.5, which can only be caused by quenching of Er-ions in the core (Figure S3.2b). Even when the particles are dispersed in strong quenching media enabling non-radiative deactivation of the ^{2}F$_{5/2}$ level by O-H- vibrations[36], the Yb-shelled particles still show brighter luminescence compared to Er-shelled particles in D$_2$O (Figure S3.2c). The fact that the Yb-shelled particles are still brighter in a high-quenching environment confirms our assumption that energy migration is more facilitated between Er^{3+} ions compared to Yb^{3+} ions, which is why the Yb-shell functions also as surface passivator here. A saturation of Yb ions, which also can suppress energy migration, can be excluded as the power dependent luminescence

tends not to flatten out at the excitation power at 140 W·cm^{-2} (Figure S3.2d). However, as a NaYF$_4$ shell of similar thickness leads to an enhancement factor of about 100,000 (Figure 3.2c), it becomes obvious that the Yb-shielding cannot compete with growing an inert shell despite the higher absorption cross-section.

For a better understanding of the role of Yb^{3+} and Er^{3+} in the process of energy migration and quenching, four particle systems of almost identical sizes with different percentage of Yb^{3+} and Er^{3+} doping have been compared: (80:2, 20:20, 20:2, and alloyed: 80:20). They were all equipped with an ~ 1 nm NaYF$_4$ shell (TEM micrographs in Figure S3.3). The particles with 80% Yb^{3+} should profit from the higher absorption cross-section, while particles with 20% Er^{3+} suffer from stronger energy migration to the particle surface, which is to a certain extend prevented by the NaYF$_4$ shell. Luminescence measurements (Figure S3.4) revealed that the total intensity in the visible range is comparable for particles with 20%Yb^{3+} : 2%Er^{3+}, 80%Yb^{3+} : 20%Er^{3+}, or 80%Yb^{3+} : 2%Er^{3+}, with green-to-red ratio changing from 6.7 to 2.5 to 0.9 for those particles. The stronger green emission of the 80%Yb^{3+}, 20%Er^{3+} particles probably results from the increased number of emitting ions, which is 10-fold higher compared to particles with 80%Yb, 2%Er. As the higher Er^{3+} rate also leads to more C-H quenching, which mainly affects the red emission[59], the green-to-red ratio changes for those particles. The red emission is unexpectedly intense for both systems with 80% Yb^{3+} content and highest for the 80%Yb^{3+} : 2%Er^{3+} system compared to 80%Yb^{3+} : 20%Er^{3+}. This is somehow surprising, since high amounts of Er^{3+} in the particle core are known for small green-to-red ratios.[35,50] Apparently, high Yb^{3+} content also encourages population of the red emitting level, what can be explained with the back-energy-transfer (BET) process (Figure 3.1a). After absorption of three photons, energy can be transferred from Er^{3+} to Yb^{3+}, ending up in the $^4F_{9/2}$ level, where the red emission emerges.[60] The more Yb^{3+} ions are surrounding one Er^{3+} ion, the higher is the probability for this process. According to the theory that Er^{3+} facilitates energy migration, stronger quenching effects for the particles with 20% Er^{3+} were expected.

The UCL of the 20%Yb^{3+} : 20%Er^{3+} particles proves this assumption, as its intensity is much weaker at a green-to-red ratio of 3.5, compared to the 20%Yb^{3+} : 2%Er^{3+} particles (Figure S3.4). For the alloyed system, the two effects of enhanced absorption and enhanced energy migration are both contributing to the luminescence, which is why the total luminescence is similar compared to the doped system (20%Yb^{3+} : 2%Er^{3+}). Since the alloyed system is stronger influenced by energy migration and surface quenching, the degree of surface passivation shall be more

important for this system. Shell growth of a 1 nm $NaYF_4$ shell is already improving the UCL efficiency. This leads to the question in what extent an increasing shell thickness shells prevents the migration.

Alloyed β-$NaYbF_4$(20%Er)@$NaYF_4$ particles with 8.5 nm core size and varying shell thicknesses were synthesized (Figure S3.5). For comparison, also core-shell structures with doped composition in the core (β-$NaYF_4$(20%Yb,2%Er))@$NaYF_4$) were prepared (Figure S3.5). Since the alloyed particles are more influenced by energy migration and surface quenching, a stronger effect from shell growth was expected for those particles with high lanthanide content. This assumption was verified by the experimental data (Figure 3.4).
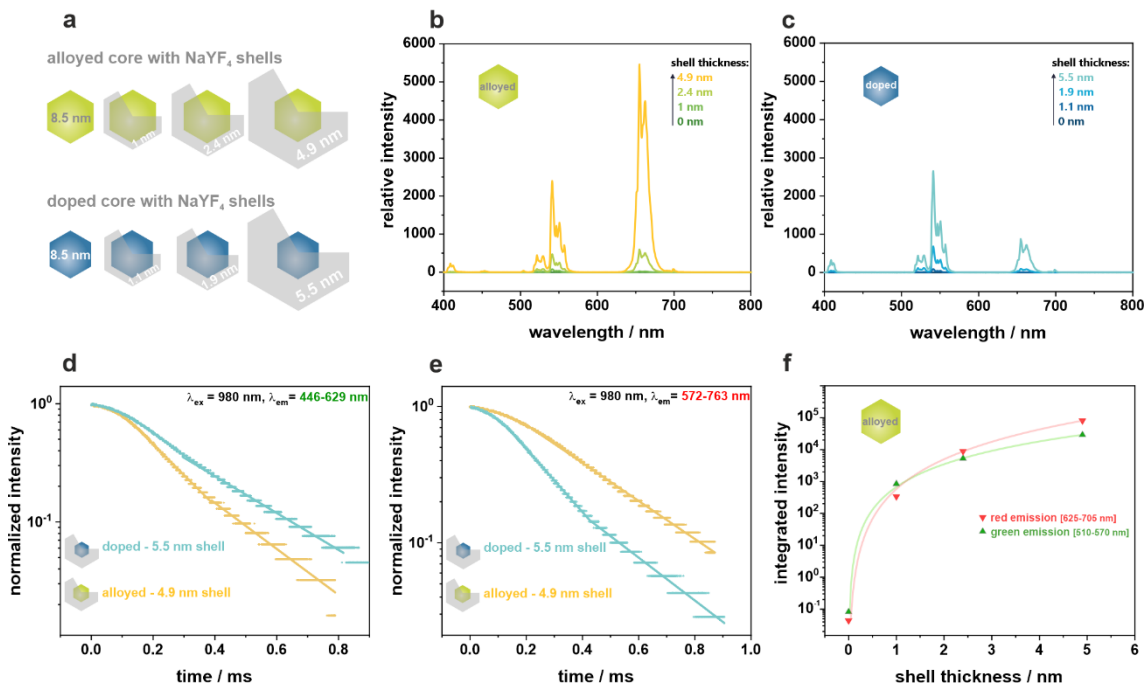
Figure 3.4. (a) Scheme of core-shell structures with different thicknesses of $NaYF_4$ shells. Luminescence spectra of alloyed β-$NaYbF_4$(20%Er)@$NaYF_4$ (b) and doped β-$NaYF_4$(20%Yb,2%Er))@$NaYF_4$ (c) core-shell structures with varying shell thicknesses. Luminescence decay of (d) green and (e) red upconversion emissions of alloyed and doped core-shell particles. (f) Integrated luminescence intensities of green and red emissions of alloyed core-shell structures as a function of the shell thicknesses. Luminescence spectra were recorded in cyclohexane upon 980 nm excitation with 140 W·cm^{-2} (cw) and normalized to the particle concentration [particles·mL^{-1}].

The probably most special difference of alloyed and doped particles is the effect of the first, thin (1 nm) $NaYF_4$ shell. While for doped particles the difference in luminescence intensities between core-shell and core is about two orders of magnitude, the difference is about four orders of magnitude for alloyed nanoparticles (Figure S3.6a). This means, already a thin shell is sufficient to block a large part of the energy transfer processes and therefore leads to an impressing

enhancement of the luminescence intensities, which are then in a comparable range to the doped UCNPs. Surprisingly, further shell growth affects the green emission in a comparable way for alloyed and doped particles, while the red emission undergoes a significant increase of intensity. The strong enhancement of the red emission for alloyed particles with increased shell thickness is also reflected in the green-to-red ratio, which is > 1 for core particles and particles with 1 nm shell, while it changes in favor of the red emission (< 1) for thicker shells (Figure 3.4f). For doped particles, this remarkable change in peak ratios with increasing surface passivation was not observed (Figure S3.7).

Alloyed nanoparticles in general have a much stronger red luminescence compared to doped nanoparticles. To understand this phenomenon, one has to review the processes which feed the red emitting $^4F_{9/2}$ level (Figure 3.5).[60–62] While pathways 1 and 2 should happen more or less equally for both particle systems, pathways 3 and 4 are dominated by cross relaxation and back-energy-transfer processes. The probability of cross-relaxations increases with rising Er^{3+} content, while back-energy-transfer – where energy is transferred back from Er^{3+} to Yb^{3+} – should be facilitated for higher Yb^{3+} content. As in alloyed nanocrystals sensitizer and activator ions are not separated by optical silent ions, one can assume that pathways 3 and 4 play a major role additionally to the popular pathways 1 and 2, which then leads to the intense red emission. According to this theory, the contribution of three-photon-excitation is also increased for alloyed particles compared to doped particles. This was confirmed by excitation power dependent luminescence measurements (Figure S3.6b).
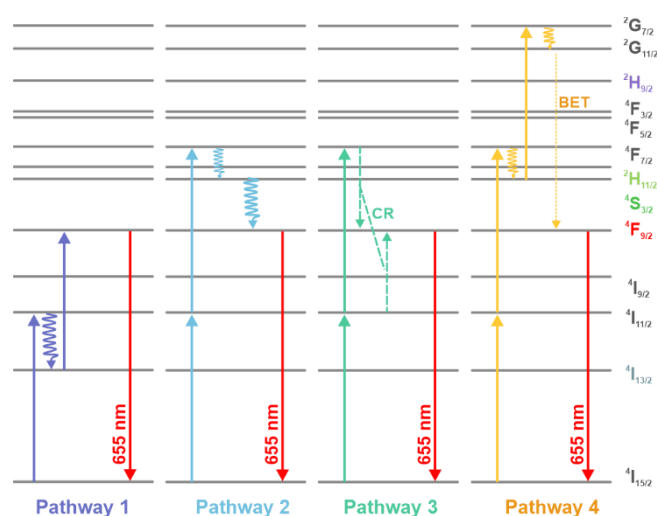

Figure 3.5. Excitation pathways for red upconversion luminescence. BET: back-energy-transfer and CR: cross-relaxations Curled arrows indicate nonradiative decay processes.

The impressive difference in red luminescence for surface protected and unprotected UCNPs is an indication that quenching processes have a strong impact on the population of the red emitting level ($^4F_{9/2}$) in alloyed UCNPs. Meijerink *et al.* have shown that the $^4F_{9/2}$ level is quenched by aliphatic C–H vibrations, while the green emission is stronger influenced by aromatic C–H vibrations.[59] With cyclohexane (twelve C–H bonds) as solvent and oleic acid (33 C–H-bonds) as surface ligand, this is a reasonable explanation for the increase of the red UCL with rising shell thickness. To prove this theory, luminescence of alloyed particles with 1 nm and 4.9 nm shell were both compared with and without oleic acid ligand in cyclohexane and DMF (six C–H-bonds) (Figure S3.8). The change in peak ratio was stronger for the thin shell (36%) compared to the thicker 4.9 nm shell (11%), which supports the hypothesis of strong impact of the interface and the environment of a particle system in dispersions.

The large difference in population pathways of alloyed and doped systems also influences the luminescence lifetimes of the green ($^2H_{11/2}$ and $^4S_{3/2}$) and red ($^4F_{9/2}$) emitting states. The main parameter influencing the visible upconversion decay times is quenching of the 1 μm level, which is also the level where probably most of the energy migration occurs.[63] In an ideal case, where the surface of the alloyed particles is perfectly protected and hence surface quenching is prevented, energy migration still takes place, but is not followed by quenching. This would lead to strong but delayed luminescence, as it was also observed by Zhang *et al.*, who found longer luminescence lifetimes for samples with increased energy migration pathways.[64] The green levels are depopulated by cross-relaxation processes in particles with high Er^{3+} content, leading to shorter lifetimes. Luminescence decay curves were recorded for the core-shell variants with the thickest shell (Figure 3.4d and e). While doped particles possess a longer luminescence lifetime for the green emitting states, the alloyed particles show a longer lifetime for the red emitting state ($^4F_{9/2}$), which confirms the theory. For particles with thin shells, this effect is not as obvious, since the quenching processes of solvents and ligands play a greater role (Figure S3.9).

Surface passivation is inevitable for alloyed nanoparticles to emit bright upconversion luminescence. The high lanthanide content favors energy migration which leads to quenching of excited state levels at the nanoparticle surface. According to this theory, surface processes are responsible for the non-radiative energy loss. Since small nanoparticles have a higher surface-to-volume ratio compared to nanoparticles of larger diameter, alloyed core-shell UCNPs were synthesized with different core diameters to validate this fact (Figure S3.10). An X-ray-diffraction pattern of the

largest core variant is displayed in Figure S3.11 and proves the hexagonal crystal structure of the alloyed particles. For acquiring information from the UCL spectra of dispersions of particles of different size, doping, and concentration it is of greatest importance to carefully choose the method of data normalization. The informative value in normalizing to the particle concentration regarding the influence of surface-to-volume ratio is limited, as a larger particle just contains a higher number of absorbing and emitting ions, which is why higher luminescence intensities are recorded independently from the surface-to-volume ratio (Figure S3.12). Hence, normalization to the concentration of Er^{3+} ions was performed (Figure 3.6), as this results in the relative emission intensity per emitting ion.
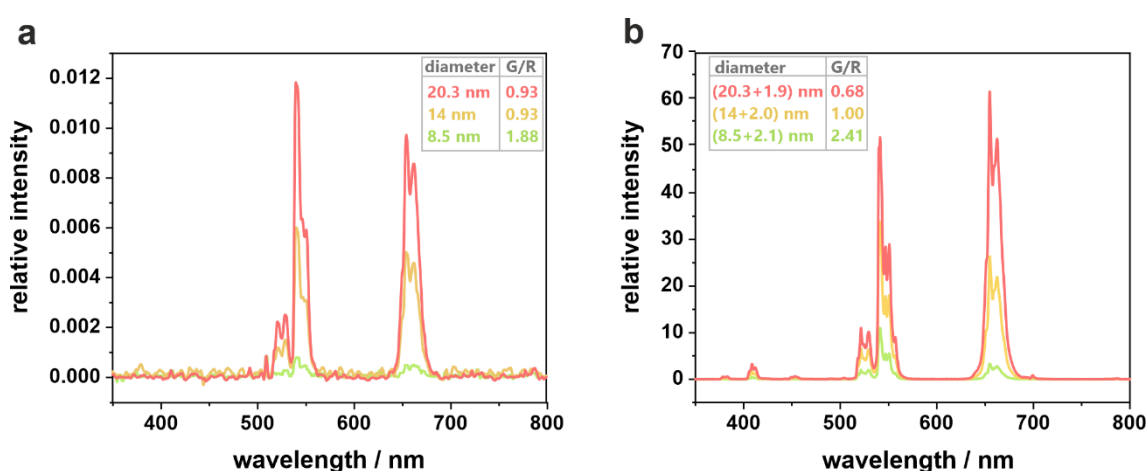
Figure 3.6. Upconversion luminescence spectra of alloyed (a) core and (b) corresponding core-shell particles with varying core diameters and constant shell thickness. Corresponding green-to-red ratios (G/R) of the integrated green and red luminescence emission are indicated in the legend. Measurements were performed in cyclohexane at 980 nm with an excitation power density of 140 W·cm^{-2}. The spectra were normalized to the Er^{3+} concentration which was determined *via* ICP-OES.

In that respect, the largest particles are the brightest and show the longest decay times (Figure S3.13), while smallest nanoparticles show the lowest luminescence intensity and shortest lifetimes, what confirms the impact of surface-to-volume ratio on the photophysical properties. From these results one can expect that shell growth is even more important for small particles with high surface-to-volume ratios to prevent the quenching processes. Indeed, for small (8.5 nm) nanoparticles, the effect, comparing core to core-shell particles, is quite large (~ factor 12,000). For the bigger (20.3 nm) particles an enhancement factor of only ~ 5,800 was found, which is in accordance with the lower surface-to-volume ratio. Additionally, the different degrees of quenching do not only affect the total luminescence intensity but also the green-to-red ratio (Figure 3.6). As it was found for particles with varying shell thicknesses, the influence of C–H-quenching on the red emission is stronger

compared to green, which is why the green-to-red ratio decreases with larger diameter for core-only as well as for core-shell particles.

3.4 Conclusion

This study focusses on the two effects of high lanthanide content inside upconversion nanoparticles affecting their photophysical properties: enhanced absorption cross-section on the one side and enhanced energy migration on the other side. To profit from the higher absorption cross section of alloyed particles with 80% Yb and 20% Er content, it is inevitable to have control about the energy migration as otherwise huge losses in luminescence intensity were observed. Surface passivation by $NaYF_4$ shell growth was demonstrated as a very efficient way to enhance particle luminescence, where luminescence increases with rising shell thickness. Reduction of the surface-to-volume ratio by increasing the particle diameter also helps to increase the particle brightness. Interestingly, depending on size and shell thickness, very different green-to-red-ratios can be achieved. The examination of the influence of particle diameter and shell thickness can also be a decision aid for particle design. If the size plays no roll at all, core particles as large as possible with a shell thickness as thick as possible will give the brightest luminescence. As most applications involve a size limitation one must weigh up whether to choose a small core particle with thick shell or a large core particle with thin shell. Nevertheless, our results suggest equipping alloyed upconversion nanoparticles with a $NaYF_4$ shell of at least 2 nm thickness. As already demonstrated, one can achieve bright UCL at low power in microscopy[40], or if one envisions to use those particles as a reporter in biosensing, a thin shell might be the best choice to improve FRET efficiencies. Hopefully, this work stimulates researchers to rethink the optimal composition of small colloidal dispersed upconversion nanoparticles. Modelling of rate equations for alloyed upconversion nanoparticles might be helpful to find the best combination in lanthanide content and thickness of a $NaYF_4$ shell.

For comparison, also particles with 20% Yb, 2% Er were synthesized, which have similar luminescence intensities for thin $NaYF_4$ shells, while a great increase in the red emission with rising degree of surface passivation was only found for the alloyed system. The very intense red emission can be a great chance for new applications including upconversion nanoparticles. Since scattering effects are about factor two times lower for red compared to green visible light (for *Rayleigh* scattering, ~λ^{-4}),[65] highly doped or alloyed nanoparticles are very suitable for bioimaging applications. There is also a huge application potential in photodynamic therapy, as many

photosensitizer dyes (*e.g.* porphyrines or cyanines) have their absorption maximum in the range of the red upconversion emission.[66]

3.5 Materials and Methods

3.5.1 Chemicals

Oleic acid and 1-octadecene (both of technical grade, ≥ 90%) were obtained from *Alfa Aesar*. Yttrium chloride hexahydrate ($YCl_3 \cdot 6H_2O$, ≥ 99.9%) and ytterbium chloride hexahydrate ($YbCl_3 \cdot 6H_2O$, ≥ 99.9%) were purchased from *Treibacher Industrie AG*. Sodium oleate (82%) and erbium chloride hexahydrate ($ErCl_3 \cdot 6H_2O$, ≥ 99,9%) were acquired from *Sigma Aldrich*. Oleylamine (80 - 90%) was bought from *Acros Organics*. Sodium hydroxide and ammonium fluoride (98%) were acquired from *Merck*. A multielement standard of the six elements Er, Gd, Nd, Tm, Y, and Yb, each 1,000 mg mL^{-1} (dissolved in 1.5 M HNO_3) was received from *Bernd Kraft GmbH*. Nitric acid (HNO_3, 65%) was obtained from *VWR Chemicals*. Sulfuric acid (H_2SO_4, ≥ 95% (w/w)), cyclohexane (analytical reagent grade), dimethylformamide (DMF, ≥ 99.5%) and methanol (MeOH, ≥ 99.9%) were purchased from *Fisher Scientific*. All other organic solvents were of analytical grade. All chemicals were used without further purification. For aqueous solutions, double distilled water was used in each case.

3.5.2 Characterization

Transmission electron microscopy images (TEM) were recorded with a 120 kV CM12 microscope (*Philips*). Particle dispersions (1 mg mL^{-1}) were dropped on carbon coated copper grids, several micrographs were recorded per sample and to reveal a particle-size distribution at least 1,000 particles were analyzed using the software ImageJ. Lanthanide concentrations were determined using optical emission spectroscopy with inductively coupled plasma excitation (ICP-OES) with an SPECTROBLUE FMX36 instrument (*SPECTRO*). Details for the calibration and concentration determination can be found in the SI. X-ray powder diffraction patterns (XRD) were collected using a STOE STADI P diffractometer equipped with a Dectris Mython 1K detector. Monochromatic Cu K$_{\alpha 1}$ radiation (λ = 1.54056 Å) was used and the resolution of the patterns was 0.005° (2θ). For luminescence recording, a custom-built spectroscopic set-up was used, including a *Qmini* UV/VIS spectrometer with the corresponding software *Waves* (*Broadcom*) and in 90° configuration a 980 nm, 200 mW (cw) laser module (*Picotronic*). The luminescence curves were normalized to the particle concentration or the Er^{3+}-concentration. Signal smoothing was

performed for samples with very low luminescence signals, using percentile filtering or Savitzky-Golay filtering.[67] Green-to-Red ratios were calculated by dividing the integral of the green emission [510 nm – 570 nm] by the integral of the red emission [625 nm – 705 nm]. Luminescence decay curves were recorded with a custom-built setup, which is equipped with a 980 nm 200 mW (cw) laser module (*Picotronic*) and an optical chopper (*Thorlabs*). To collect green and red upconversion signals, two filters with transmission at [446 - 629 nm] and [572 - 763 nm] are inserted. A photomultiplier (*PreSens*) was used for signal amplification, while the oscilloscope Voltcraft PLUS DSO 8204 (*Conrad*) was incorporated for signal analysis. Absorption spectra of the particle dispersions in cyclohexane were recorded with a Cary 50 Scan UV-Visible Spectrophotometer (*Agilent*).

3.5.3 Synthesis of Upconversion Nanoparticles

The synthesis of alloyed UCNPs was performed according to a protocol published by the group of Bruce Cohen[40] with modifications. For a 10 mmol batch size of β-NaYbF$_4$(20%Er) nanoparticles, the lanthanide trichloride hexahydrates YbCl$_3$·6H$_2$O (8 mmol) and ErCl$_3$·6H$_2$O (2 mmol) were dissolved in methanol. Other particle compositions were prepared analogously using desired molar ratios of lanthanide ions. The solution was transferred into a three-necked round-bottom flask, oleic acid (82.5 mL) and octadecene (100 mL) were added and heated to 110 °C under nitrogen atmosphere. Solvent and crystal water were evaporated by applying vacuum for 1 h. After cooling to room temperature, sodium oleate (31.25 mmol), NH$_4$F (50 mmol), oleylamine (95 mmol), and octadecene (43.75 mL) were added. To reach different nanoparticle sizes, the amount of oleylamine and sodium oleate was varied (see Table 3.1). Vacuum was applied for another 20 minutes followed by degassing the solution three times. Subsequently, the mixture was heated to 315 °C under reflux with a heating rate of 16 °C min^{-1} before rapidly cooling to room temperature after 45 min. For smaller batch sizes, the time at 315 °C was shortened (for 1 mmol: 15 min). The nanoparticles were precipitated in a centrifuge tube by addition of excess of ethanol, collected *via* centrifugation (3,000 g, 5 min) and purified by redispersing in cyclohexane and precipitating with ethanol three times. Afterwards, the particles are dispersed in cyclohexane, aggregates were removed *via* centrifugation (3,000 g, 5 min) and the particle dispersion was stored at 8 °C.

Table 3.1. Variation of amounts of sodium oleate and oleylamine for different particle sizes and compositions. Values refer to a batch size of 1 mmol rare earth ions.

composition	resulting diameter / nm	n(Na-oleate) / mmol	n(oleylamine) / mmol
β-NaYbF$_4$(20%Er)	8.5	3.13	9.50
β-NaYbF$_4$(20%Er)	14.0	3.13	/
β-NaYbF$_4$(20%Er)	20.3	2.13	/
β-NaYF$_4$(20%Yb,2%Er)	7.6	3.13	9.50
β-NaYbF$_4$(18%Y,2%Er)	8.8	3.13	16.50
β-NaYF$_4$(20%Yb,20%Er)	7.6	3.13	8.25

3.5.4 Synthesis of Core-Shell Nanoparticles

A shell precursor consisting of cubic NaYF$_4$ was prepared first. For a 10 mmol batch size, YCl$_3$·6H$_2$O (10 mmol) was dissolved in methanol. The solution was transferred into a three-necked round-bottom flask and oleic acid (80 mL) and octadecene (150 mL) were added. The mixture was heated to 160 °C under nitrogen flow before vacuum was applied for 30 min. After cooling to room temperature, NH$_4$F (4.0 mmol) and NaOH (2.5 mmol), which was dissolved in methanol, were added and the mixture was heated to 120 °C for 30 min followed by a heating step to reflux (about 240 °C) for 30 min. After cooling to room temperature, the cubic particles were purified as described for hexagonal particles.

For the growth of a 2.4 nm shell, a three-necked round-bottom flask containing hexagonal particles (0.5 mmol) dispersed in cyclohexane, oleic acid (2.5 mL), and octadecene (2.5 mL) was heated to 100 °C under nitrogen atmosphere. A second flask containing cubic precursor material (1.2 mmol), oleic acid (6 mL), and octadecene (6 mL) was also heated to the same temperature. After applying vacuum to both flasks for 30 min, the flask containing the core particles was heated to reflux (about 325 °C). During heating, 0.5 mL of shell precursor was injected to the core particles *via* a syringe. At 325 °C, after every 4 minutes, small portions of shell precursor were injected to the core particles to obtain uniform shell formation. After the last injection, the dispersion was kept at 325 °C for another 4 min and subsequently cooled to room temperature. Purification of the core-shell particles was performed as described for the core particles. For synthesis of other shell thicknesses,

the core to shell-precursor material was varied and the corresponding amounts of oleic acid and octadecene adjusted, according to following calculations:

First, the average volume of the core particle and the shell were calculated, where d_{core} was determined by TEM and $d_{core\text{-}shell}$ is the desired diameter of the final particle. Although the particle growth of a hexagonal crystal lattice leads to hexagonal prisms, such shapes were not observed by TEM for the nanoparticles (hexagonal prisms are usually clearly to identify for particles > 25 nm diameter). Instead, a quasi-spherical shape is revealed in the TEM images, which is why spherical geometry was assumed for the calculations.

$$V_{core} = \frac{4}{3} \cdot \pi \cdot \left(\frac{d_{core}}{2} \right)^3$$

$$V_{shell} = \frac{4}{3} \cdot \pi \cdot \left[\left(\frac{d_{core\text{-}shell}}{2} \right)^3 - \left(\frac{d_{core}}{2} \right)^3 \right]$$

Including the density ρ of the materials, the molar ratio can be determined.

$$\frac{n_{core}}{n_{shell}} = \frac{\rho_{core} \cdot V_{core} \cdot M_{shell}}{\rho_{shell} \cdot V_{shell} \cdot M_{core}}$$

With a chosen amount of core particles (*e.g.,* 0.5 mmol), the required amount of shell precursor can be determined including the calculated molar ratio.

3.5.5 Calculation of the Particle Concentration

Concentrations of the rare earth ions were determined using inductively coupled plasma optical emission spectroscopy (ICP-OES). A multielement standard containing Y, Gd, Er, Tm, Yb, and Nd (all 1,000 mg mL^{-1} in 1.5 M HNO$_3$) was used to prepare calibration solutions (V=25 mL) with lanthanide concentrations of 0 ppb (blank), 100 ppb, 500 ppb, 2,000 ppb, 5,000 ppb, 10,000 ppb and 20,000 ppb using 1.5 M HNO$_3$ for dilution of the standard and including addition of concentrated H$_2$SO$_4$ (1.25 mL) to each solution. Sample preparation was performed as follows: 10 µL of UCNP-dispersions were dried in a glass vial, concentrated H$_2$SO$_4$ (0.5 mL) was added, and the sample was sonicated for several minutes to dissolve the nanoparticles. The solution was diluted to a total volume of 10 mL using 1.5 M HNO$_3$. After calibration of the instrument, each sample was measured three times and the mean concentration of each element was calculated. An average molar mass for NaREF$_4$ (RE=rare earth) can be calculated including the percentage proportion of each rare earth ion molar masses:

$$M_{NaREF_4}=M_{Na}+4\,M_F+\sum_i \frac{c_i}{c_{RE}}\cdot M_i$$

Where c_i is the concentration per rare earth element with corresponding molar weight M_i, c_{RE} the total concentration of rare earth ions and M_{Na} and M_F the molar weights of sodium and fluor, respectively.

The mass concentration β was then determined as

$$\beta_{NP}=M_{NaREF_4}\cdot c_{RE}$$

For normalization of the curves, the particle concentration C [particles·mL^{-1}] was required. It was calculated by dividing the mass concentration by the mass of a single nanoparticle m_{NP}, according to following formula, assuming a spherical particle shape.

$$C_{NP}=\frac{\beta}{m_{NP}}=\frac{\beta}{\rho_{core}\cdot\frac{4}{3}\cdot\left(\frac{d_{core}}{2}\right)^3\cdot\pi+\rho_{Shell}\cdot\pi\cdot\frac{4}{3}\cdot\left[\left(\frac{d_{CS}}{2}\right)^3-\left(\frac{d_{core}}{2}\right)^3\right]}$$

3.5.6 Calculation of Absorption Cross-Sections

The absorption cross-sections are calculated according following equations:

$$\sigma(\lambda)=\frac{1}{C\cdot l}\,\ln\left(\frac{p_\lambda^0}{p_\lambda}\right)$$

where C is the number of molecules (or nanoparticles) per volume, *l* is the optical pathlength of 1 cm, and p_λ^0 and p_λ are incident and transmitted spectral radiant power.[68]

With

$$A=\lg\left(\frac{p_\lambda^0}{p_\lambda}\right)=\frac{\ln\left(\frac{p_\lambda^0}{p_\lambda}\right)}{\ln 10}=\varepsilon(\lambda)\cdot c\cdot l$$

and

$$C=c\cdot N_A$$

where A corresponds to the absorbance, $\varepsilon(\lambda)$ is the extinction coefficient, *c* the molar concentration in [mol/L] and $N_A=6.022\cdot 10^{23}$ mol^{-1}, one finds the following relation:

$$\sigma(\lambda)=\frac{1}{N_A\cdot c\cdot l}\,\ln 10\cdot A=\frac{\ln 10\cdot\varepsilon(\lambda)}{N_A}$$

For calculation of the errors, gaussian error propagation was performed, including the error of the concentration, particle diameter, and uncertainty of absorbance measurement.

3.6 Supplementary Figures
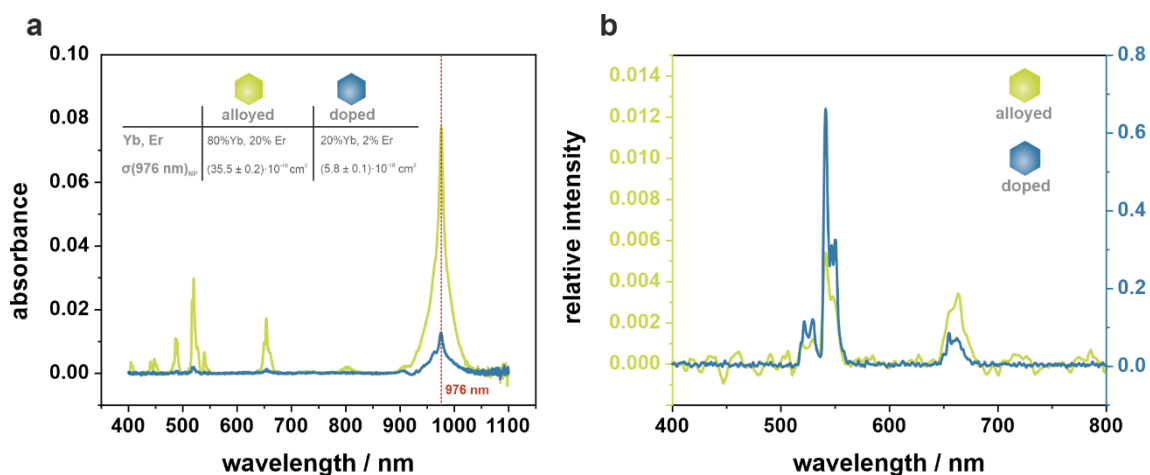
3.6.1 Absorption Spectra

Figure S3.1. (a) Absorption spectra of β-NaYbF$_4$(20%Er) (alloyed, diameter: 8.5 ± 1.2 nm) and β-NaYF$_4$(20%Yb,20%Er) (doped, diameter: 7.6 ± 1.2 nm). Spectra are background corrected and absorption corresponds to a particle concentration of 5·10^{15} particles·mL^{-1} in cyclohexane. Absorption cross-sections σ per nanoparticle are displayed in the table for the absorption maximum at 976 nm. (b) Corresponding luminescence spectra under 980 nm irradiation (140 W·cm^{-2}) with different y-scales for alloyed (left) and doped (right) particles.
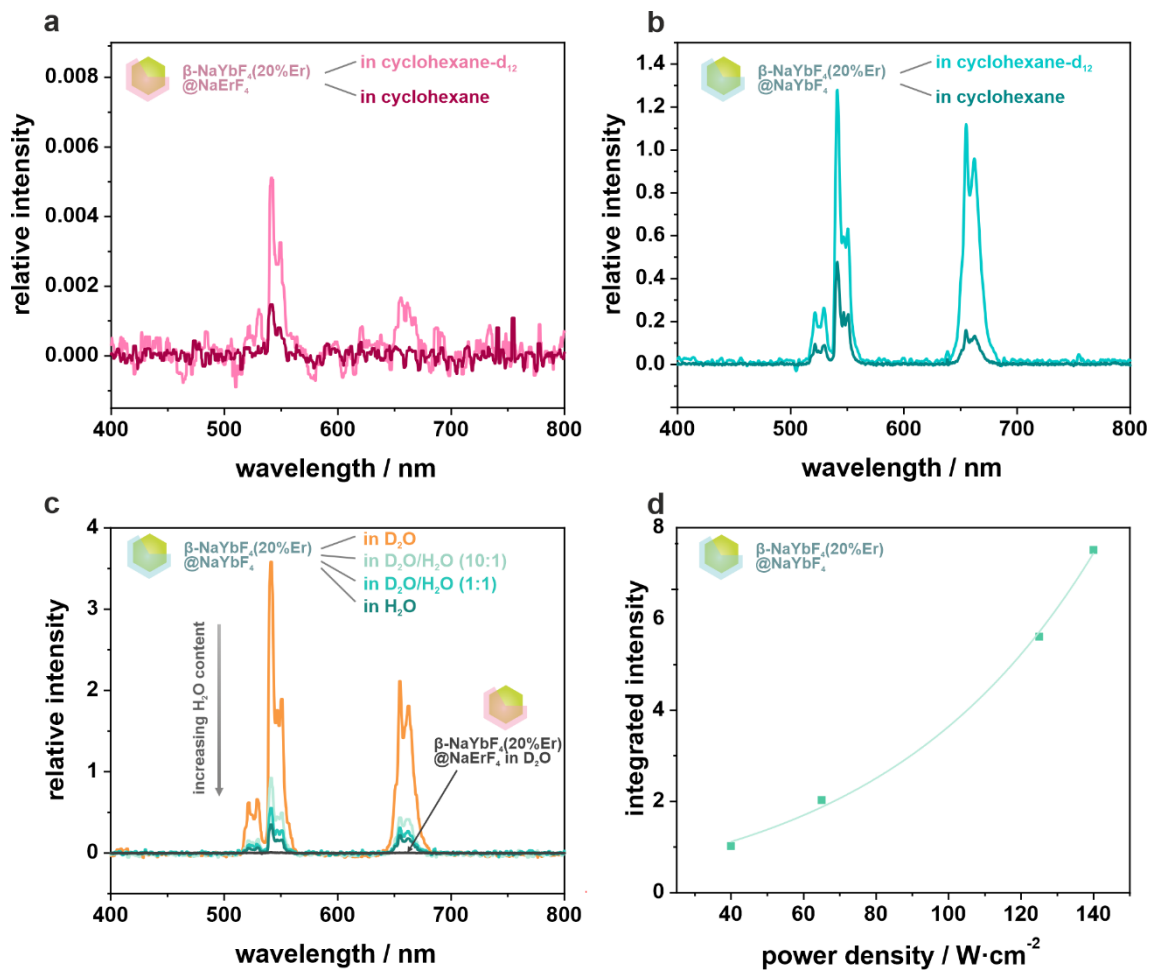
Figure S3.2. Luminescence spectra in cyclohexane and cyclohexane-d_{12} for (a) β-NaYbF$_4$(20%Er)@NaErF$_4$ and (b) β-NaYbF$_4$(20%Er)@NaYbF$_4$ core-shell nanoparticles. (c) Luminescence of β-NaYbF$_4$(20%Er)@NaYbF$_4$ in D$_2$O/H$_2$O mixtures and spectrum of β-NaYbF$_4$(20%Er)@NaErF$_4$ in D$_2$O. All spectra are recorded at 980 nm excitation with 140 W·cm^{-2} (cw) and normalized to particle concentration [particles·mL^{-1}]. (d) Integrated luminescence (400-750 nm) of β-NaYbF$_4$(20%Er)@NaYbF$_4$ particles in cyclohexane at 980 nm irradiation at different excitation power densities.

3.6.2 Particle Systems with Different Yb^{3+} : Er^{3+} Ratio
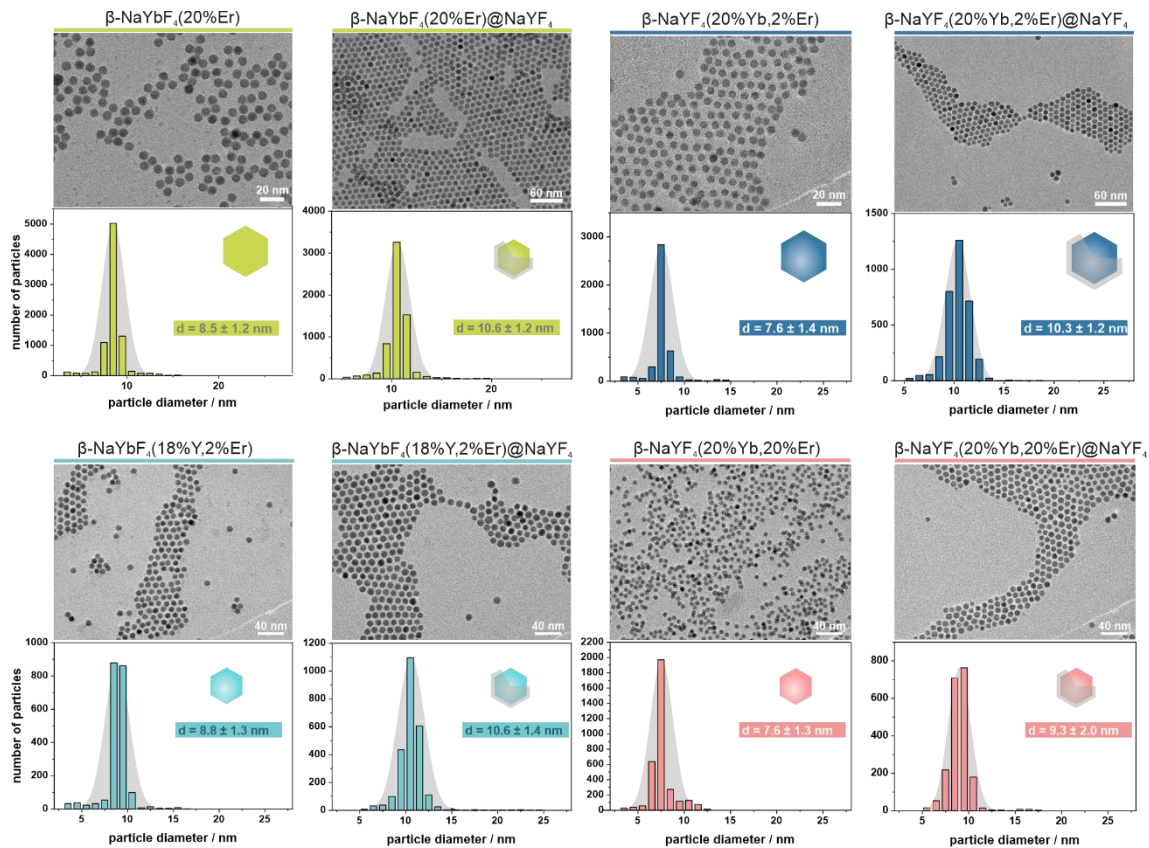
Figure S3.3. TEM micrographs and corresponding particle size histograms of β-NaYbF$_4$(20%Er), β-NaYF$_4$(20%Yb,2%Er), β-NaYbF$_4$(18%Y,2%Er) and β-NaYF$_4$(20%Yb,20%Er) core particles and corresponding core-shell particles (@NaYF$_4$).
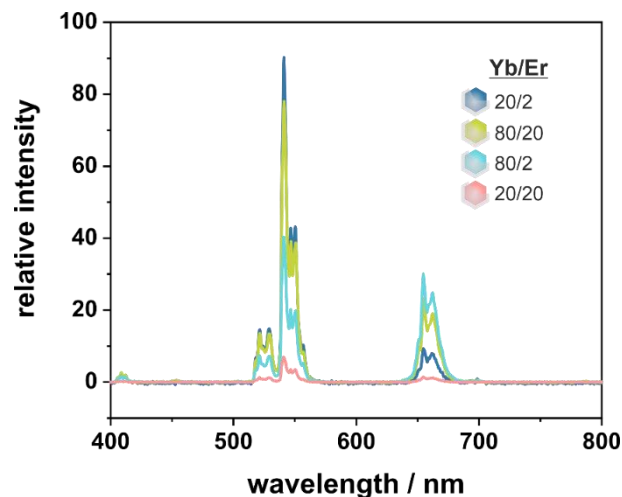

Figure S3.4. Upconversion luminescence of core-shell particles with varying Yb^{3+} and Er^{3+} content in the core. Green: β-NaYbF$_4$(20%Er)@NaYF$_4$, blue: β-NaYbF$_4$(2%Er,18%Y)@NaYF$_4$, red: β-NaYF$_4$(20%Yb,20%Er)-@NaYF$_4$, light blue: β-NaYF$_4$(80%Yb,2%Er)@NaYF$_4$. Measurements were performed in cyclohexane at 980 nm with an excitation power density of 140 W·cm^{-2}, the spectra were normalized to the particle concentration.

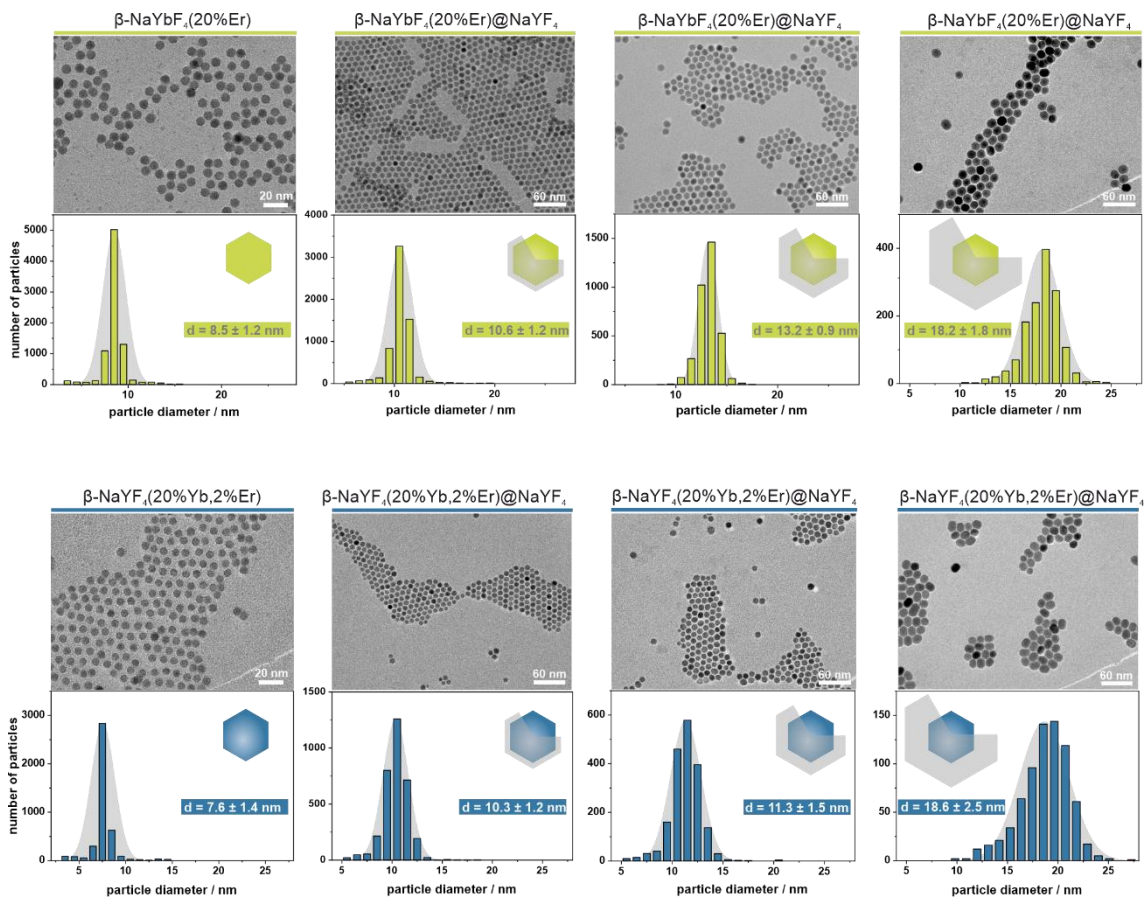## 3.6.3 Characterization of Particles with Varying Shell Thickness

Figure S3.5. TEM micrographs and corresponding size histograms of alloyed and doped nanoparticles with varying shell thicknesses.
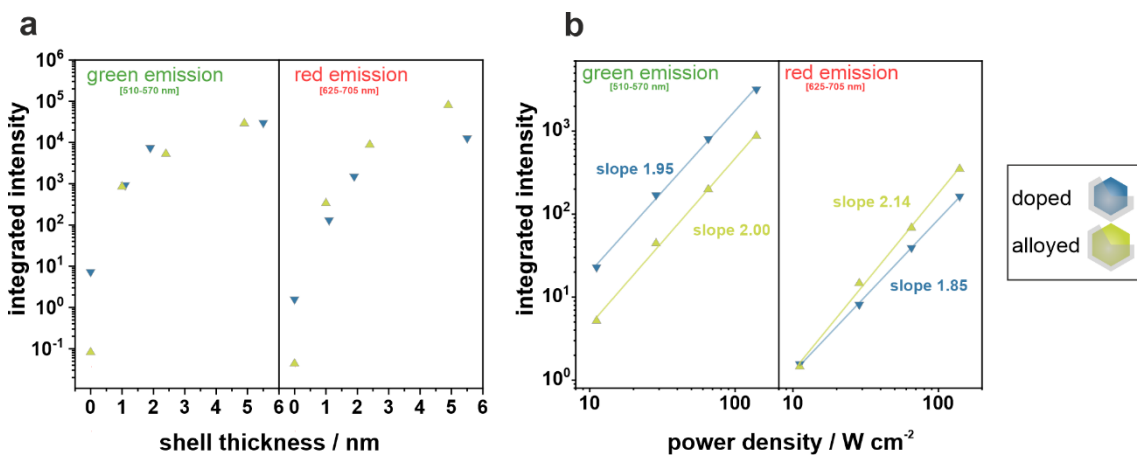

Figure S3.6. (a) Integrated intensity of green and red upconversion luminescence of alloyed (green) and doped (blue) core-shell structures for different shell thicknesses (power density: 140 W·cm^{-2}). (b) Integrated intensity of green and red upconversion emission of alloyed (8.5 nm) and classical (8.1 nm) cores with ~ 1 nm shell at varying excitation power densities. The slope is related to the number of participating photons. While no clear difference was observed for the green emission, a higher slope was found for the red emission in the alloyed system, which can be explained by the contribution of pathway 4. Measurements were performed in cyclohexane at 980 nm radiation, spectra were normalized to particle concentration.
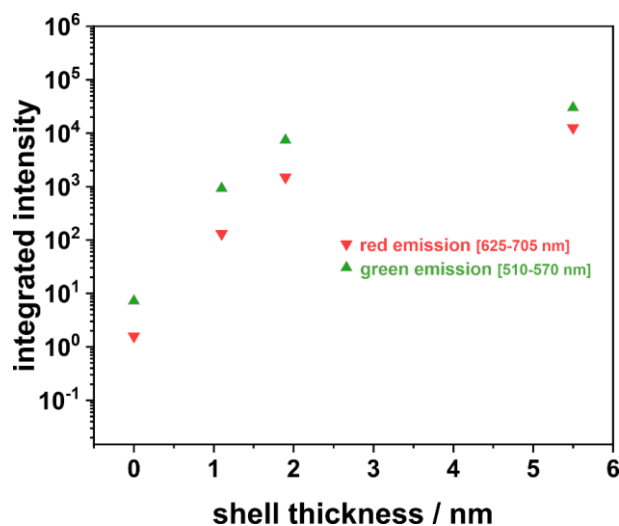
Figure S3.7. Integrated luminescence intensities of green and red emissions of β-NaYF$_4$(20%Yb,2%Er) core-shell structures as a function of the NaYF$_4$ shell thicknesses. Luminescence spectra were recorded in cyclohexane upon 980 nm excitation with 140 W·cm^{-2} (cw) and normalized to the particle concentration.
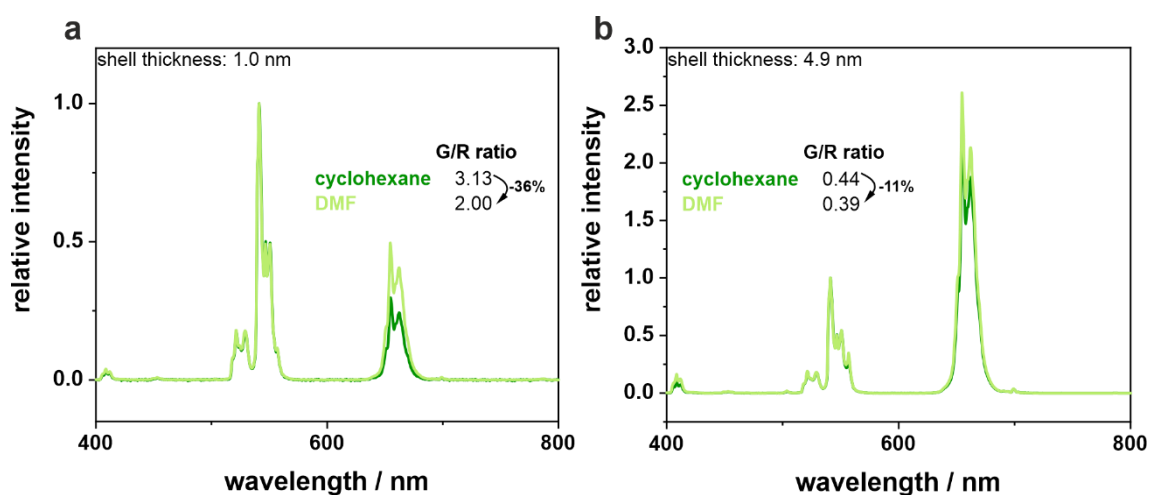

Figure S3.8. Luminescence spectra of β-NaYbF$_4$(20%Er) particles with (a) 1.0 nm NaYF$_4$ shell and (b) 4.9 nm NaYF$_4$ shell recorded in cyclohexane and DMF under 980 nm irradiation (140 W cm^{-2}).
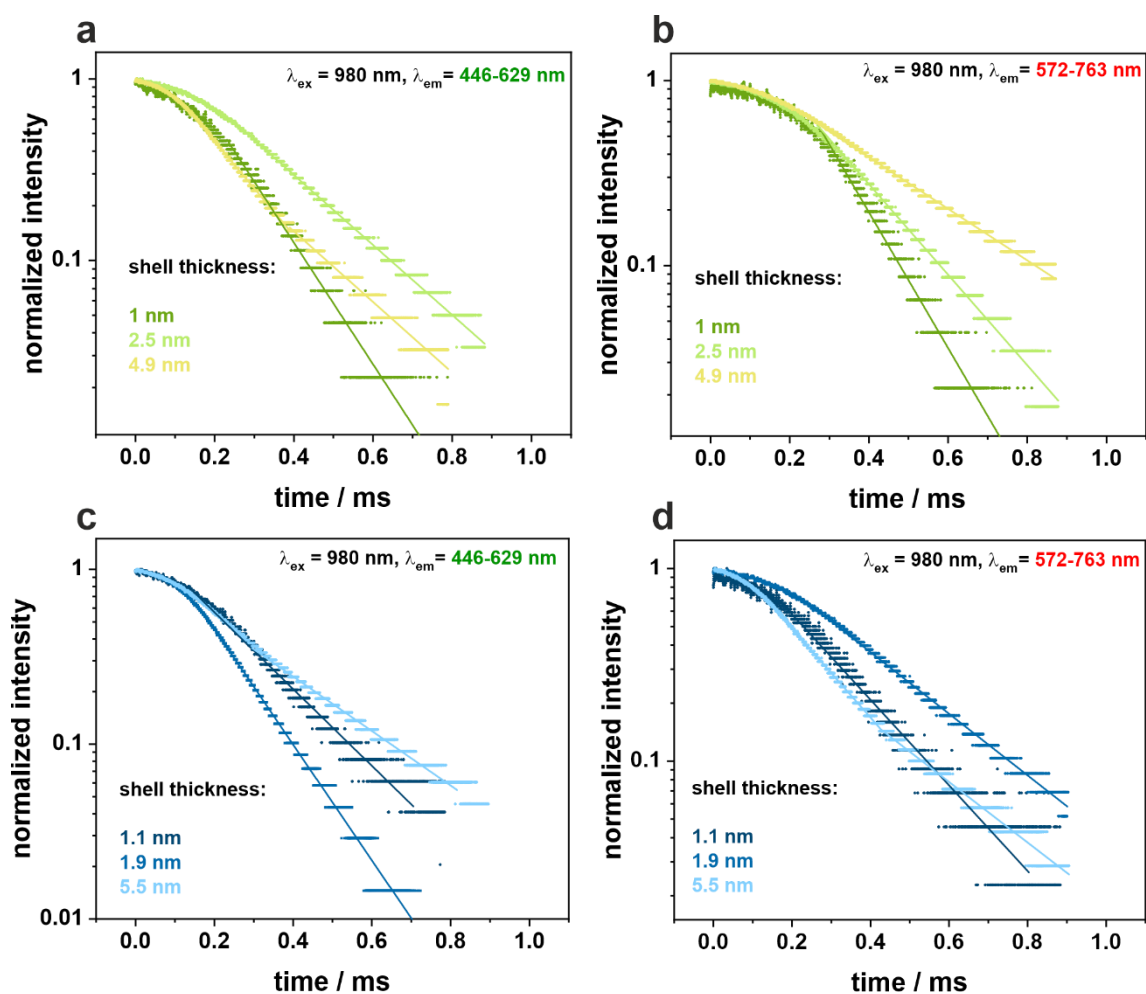
Figure S3.9. Luminescence decay curves of green and red upconversion emissions under 980 nm excitation in cyclohexane. Alloyed nanoparticles with 8.5 nm core size and varying $NaYF_4$ shell thicknesses (a,b) and doped nanoparticles with 7.6 nm core size with varying $NaYF_4$ shell thicknesses (c,d).

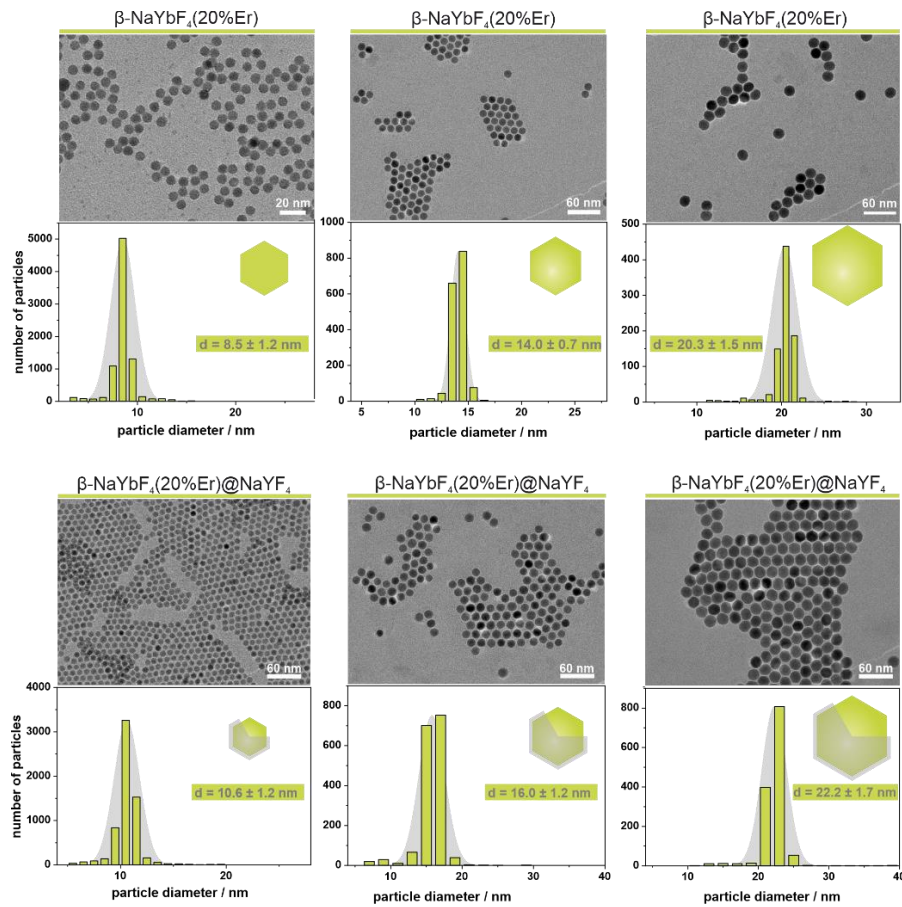## 3.6.4 Characterization of Nanoparticles with Varying Core-diameter

Figure S3.10. TEM micrographs and corresponding size histograms of alloyed core (top) and corresponding core-shell (bottom) particles with varying core diameters.
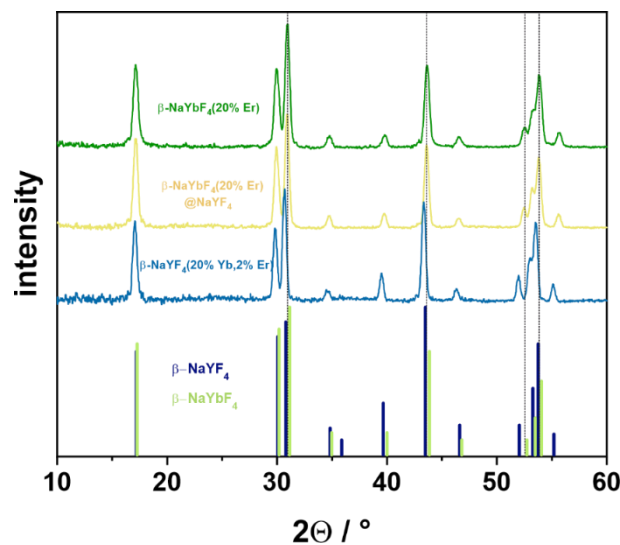
Figure S3.11. XRD pattern of β-NaYbF$_4$(20%Er) (diameter: 20.3 nm), β-NaYbF$_4$(20%Er)@NaYF$_4$ (diameter: 22.2 nm) and β-NaYF$_4$(20%Yb,2%Er) (diameter: 24.6 nm) nanoparticles. Corresponding reference pattern of β-NaYbF$_4$ (ICDD, PDF #00-027-1427) and β-NaYF$_4$ (ICDD, PDF #00-016-0334) are shown in the bottom. Dotted lines are inserted as guidelines for the eyes.
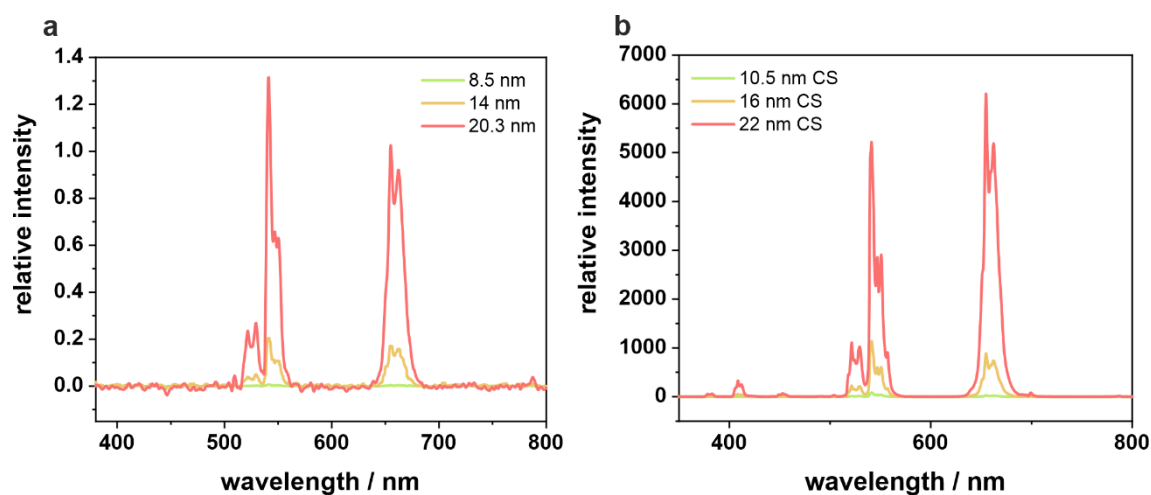
Figure S3.12. Upconversion luminescence spectra of alloyed (**a**) core and (**b**) corresponding core-shell particles with varying core diameters. Measurements were performed in cyclohexane at 980 nm with an excitation power density of 140 W·cm⁻². The spectra were normalized to the particle concentration.

Figure S3.13. Luminescence decay curves of green and red upconversion emissions under 980 nm excitation of alloyed nanoparticles with constant NaYF$_4$ shell thickness (~ 1 nm) and varying core diameters in cyclohexane (**a**,**b**).

3.7 References

[1] Niu, J.; Wang, X.; Lv, J.; Li, Y.; Tang, B. Luminescent Nanoprobes for In-vivo Bioimaging. *TrAC, Trends Anal. Chem.* **2014**, *58*, 112–119. DOI: 10.1016/j.trac.2014.02.013.
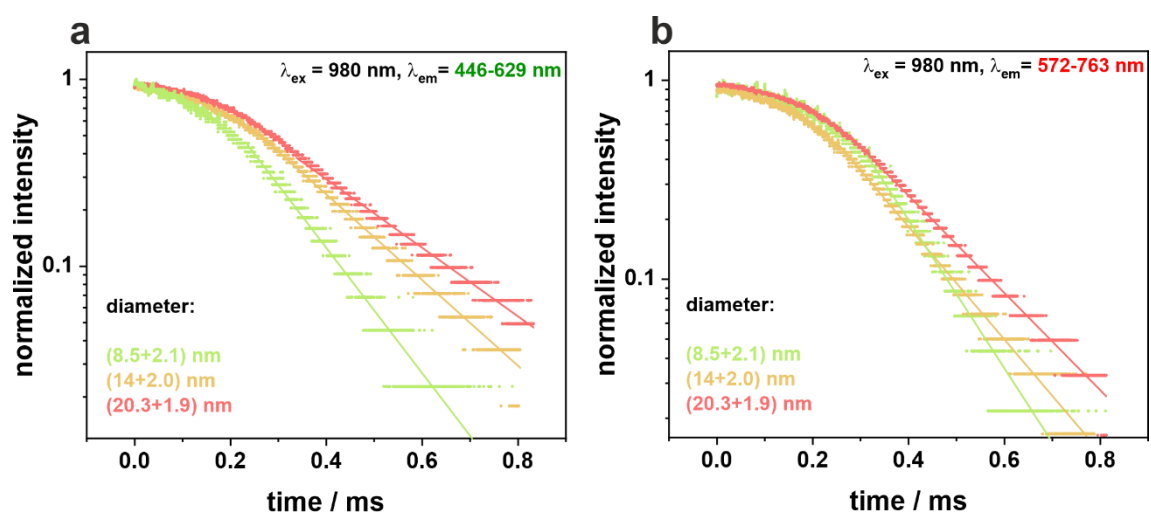
[2] Himmelstoß, S. F.; Hirsch, T. A Critical Comparison of Lanthanide Based Upconversion Nanoparticles to Fluorescent Proteins, Semiconductor Quantum Dots, and Carbon Dots for Use in Optical Sensing and Imaging. *Methods Appl. Fluoresc.* **2019**, *7* (2), 22002. DOI: 10.1088/2050-6120/ab0bfa.

[3] Steinegger, A.; Wolfbeis, O. S.; Borisov, S. M. Optical Sensing and Imaging of pH Values: Spectroscopies, Materials, and Applications. *Chem. Rev.* **2020**, *120* (22), 12357–12489. DOI: 10.1021/acs.chemrev.0c00451.

[4] Das, P.; Sedighi, A.; Krull, U. J. Cancer Biomarker Determination by Resonance Energy Transfer Using Functional Fluorescent Nanoprobes. *Anal. Chim. Acta* **2018**, *1041*, 1–24. DOI: 10.1016/j.aca.2018.07.060.

[5] Ibarra-Ruiz, A. M.; Rodríguez Burbano, D. C.; Capobianco, J. A. Photoluminescent Nanoplatforms in Biomedical Applications. *Adv. Phys.: X* **2016**, *1* (2), 194–225. DOI: 10.1080/23746149.2016.1165629.

[6] Wang, X.; Chang, H.; Xie, J.; Zhao, B.; Liu, B.; Xu, S.; Pei, W.; Ren, N.; Huang, L.; Huang, W. Recent Developments in Lanthanide-based Luminescent Probes. *Coord. Chem. Rev.* **2014**, *273-274*, 201–212. DOI: 10.1016/j.ccr.2014.02.001.

[7] Chen, G.; Qiu, H.; Prasad, P. N.; Chen, X. Upconversion Nanoparticles: Design, Nanochemistry, and Applications in Theranostics. *Chem. Rev.* **2014**, *114* (10), 5161–5214. DOI: 10.1021/cr400425h.

[8] Liu, Y.-Q.; Qin, L.-Y.; Li, H.-J.; Wang, Y.-X.; Zhang, R.; Shi, J.-M.; Wu, J.-H.; Dong, G.-X.; Zhou, P. Application of Lanthanide-doped Upconversion Nanoparticles for Cancer Treatment: A Review. *Nanomedicine* **2021**, *16* (24), 2207–2242. DOI: 10.2217/nnm-2021-0214.

[9] DaCosta, M. V.; Doughan, S.; Han, Y.; Krull, U. J. Lanthanide Upconversion Nanoparticles and Applications in Bioassays and Bioimaging: A Review. *Anal. Chim. Acta* **2014**, *832*, 1–33. DOI: 10.1016/j.aca.2014.04.030.

[10] Diao, S.; Hong, G.; Antaris, A. L.; Blackburn, J. L.; Cheng, K.; Cheng, Z.; Dai, H. Biological Imaging Without Autofluorescence in the Second Near-infrared Region. *Nano Res.* **2015**, *8* (9), 3027–3034. DOI: 10.1007/s12274-015-0808-9.

[11] Chen, G.; Shen, J.; Ohulchanskyy, T. Y.; Patel, N. J.; Kutikov, A.; Li, Z.; Song, J.; Pandey, R. K.; Agren, H.; Prasad, P. N.; Han, G. (α-NaYbF$_4$:Tm^{3+})/CaF$_2$ Core/shell Nanoparticles With Efficient Near-infrared to Near-infrared Upconversion for High-contrast Deep Tissue Bioimaging. *ACS Nano* **2012**, *6* (9), 8280–8287. DOI: 10.1021/nn302972r.

[12] Francouis E. Auzel. Materials and Devices Using Double-pumped Phosphors with Energy Transfer. *Proc. IEEE* **1973** (61), 758–786. DOI: 10.1109/PROC.1973.9155.

[13] Krämer, K. W.; Biner, D.; Frei, G.; Güdel, H. U.; Hehlen, M. P.; Lüthi, S. R. Hexagonal Sodium Yttrium Fluoride Based Green and Blue Emitting Upconversion Phosphors. *Chem. Mater.* **2004**, *16* (7), 1244–1251. DOI: 10.1021/cm031124o.

[14] Liang, G.; Wang, H.; Shi, H.; Wang, H.; Zhu, M.; Jing, A.; Li, J.; Li, G. Recent Progress in the Development of Upconversion Nanomaterials in Bioimaging and Disease Treatment. *J. Nanobiotechnol.* **2020**, *18* (1), 154. DOI: 10.1186/s12951-020-00713-3.

[15] Wiesholler, L. M.; Hirsch, T. Strategies for the Design of Bright Upconversion Nanoparticles for Bioanalytical Applications. *Opt. Mater.* **2018**, *80*, 253–264. DOI: 10.1016/j.optmat.2018.04.015.

[16] Paudel, H. P.; Zhong, L.; Bayat, K.; Baroughi, M. F.; Smith, S.; Lin, C.; Jiang, C.; Berry, M. T.; May, P. S. Enhancement of Near-infrared-to-visible Upconversion Luminescence Using Engineered Plasmonic Gold Surfaces. *J. Phys. Chem. C* **2011**, *115* (39), 19028–19036. DOI: 10.1021/jp206053f.

[17] Wiesholler, L. M.; Genslein, C.; Schroter, A.; Hirsch, T. Plasmonic Enhancement of NIR to UV Upconversion by a Nanoengineered Interface Consisting of $NaYF_4$:Yb,Tm Nanoparticles and a Gold Nanotriangle Array for Optical Detection of Vitamin B12 in Serum. *Anal. Chem.* **2018**, *90* (24), 14247–14254. DOI: 10.1021/acs.analchem.8b03279.

[18] Chen, G.; Damasco, J.; Qiu, H.; Shao, W.; Ohulchanskyy, T. Y.; Valiev, R. R.; Wu, X.; Han, G.; Wang, Y.; Yang, C.; Ågren, H.; Prasad, P. N. Energy-Cascaded Upconversion in an Organic Dye-Sensitized Core/Shell Fluoride Nanocrystal. *Nano Lett.* **2015**, *15* (11), 7400–7407. DOI: 10.1021/acs.nanolett.5b02830.

[19] Zhu, Y.; Ji, Y.; Chen, Q.; Wang, C.; Lu, X.; Mei, Y.; Xu, P.; Li, L.; Tan, T.; Wang, J. The Modification of Upconversion Emissions by Photonic Band Gap in β-$NaYF_4$: Yb^{3+}, Tm^{3+} Inverse Opal Structures. *J. Lumin.* **2018**, *194*, 420–423. DOI: 10.1016/j.jlumin.2017.10.069.

[20] Zhao, C.; Kong, X.; Liu, X.; Tu, L.; Wu, F.; Zhang, Y.; Liu, K.; Zeng, Q.; Zhang, H. Li^+ Ion Doping: An Approach for Improving the Crystallinity and Upconversion Emissions of $NaYF_4$:Yb^{3+}, Tm^{3+} Nanoparticles. *Nanoscale* **2013**, *5* (17), 8084–8089. DOI: 10.1039/c3nr01916k.

[21] Cheng, T.; Marin, R.; Skripka, A.; Vetrone, F. Small and Bright Lithium-based Upconverting Nanoparticles. *J. Am. Chem. Soc.* **2018**, *140* (40), 12890–12899. DOI: 10.1021/jacs.8b07086.

[22] Estebanez, N.; Cortés‐Villena, A.; Ferrera‐González, J.; González‐Béjar, M.; Galian, R. E.; González‐Carrero, S.; Pérez‐Prieto, J. Linear Coassembly of Upconversion and Perovskite Nanoparticles: Sensitized Upconversion Emission of Perovskites by Lanthanide‐Doped Nanoparticles. *Adv. Funct. Mater.* **2020**, *30* (46), 2003766. DOI: 10.1002/adfm.202003766.

[23] Han, S.; Deng, R.; Gu, Q.; Ni, L.; Huynh, U.; Zhang, J.; Yi, Z.; Zhao, B.; Tamura, H.; Pershin, A.; Xu, H.; Huang, Z.; Ahmad, S.; Abdi-Jalebi, M.; Sadhanala, A.; Tang, M. L.; Bakulin, A.; Beljonne, D.; Liu, X.; Rao, A. Lanthanide-doped Inorganic Nanoparticles Turn Molecular Triplet Excitons Bright. *Nature* **2020**, *587* (7835), 594–599. DOI: 10.1038/s41586-020-2932-2.

[24] Würth, C.; Fischer, S.; Grauel, B.; Alivisatos, A. P.; Resch-Genger, U. Quantum Yields, Surface Quenching, and Passivation Efficiency for Ultrasmall Core/Shell Upconverting Nanoparticles. *J. Am. Chem. Soc.* **2018**, *140* (14), 4922–4928. DOI: 10.1021/jacs.8b01458.

[25] Fischer, S.; Bronstein, N. D.; Swabeck, J. K.; Chan, E. M.; Alivisatos, A. P. Precise Tuning of Surface Quenching for Luminescence Enhancement in Core-Shell Lanthanide-Doped Nanocrystals. *Nano Lett.* **2016**, *16* (11), 7241–7247. DOI: 10.1021/acs.nanolett.6b03683.

[26] Haase, M.; Schäfer, H. Upconverting nanoparticles. *Angew. Chem., Int. Ed.* **2011**, *50* (26), 5808–5829. DOI: 10.1002/anie.201005159.

[27] Hyppänen, I.; Höysniemi, N.; Arppe, R.; Schäferling, M.; Soukka, T. Environmental Impact on the Excitation Path of the Red Upconversion Emission of Nanocrystalline $NaYF_4$:Yb^{3+},Er^{3+}. *J. Phys. Chem. C* **2017**, *121* (12), 6924–6929. DOI: 10.1021/acs.jpcc.7b01019.

[28] Kraft, M.; Würth, C.; Muhr, V.; Hirsch, T.; Resch-Genger, U. Particle-size-dependent Upconversion Luminescence of $NaYF_4$:Yb,Er Nanoparticles in Organic Solvents and Water at Different Excitation Power Densities. *Nano Res.* **2018**, *11* (12), 6360–6374. DOI: 10.1007/s12274-018-2159-9.

[29] Wen, S.; Zhou, J.; Zheng, K.; Bednarkiewicz, A.; Liu, X.; Jin, D. Advances in Highly Doped Upconversion Nanoparticles. *Nat. Commun.* **2018**, *9* (1), 2415. DOI: 10.1038/s41467-018-04813-5.

[30] Zhao, J.; Jin, D.; Schartner, E. P.; Lu, Y.; Liu, Y.; Zvyagin, A. V.; Zhang, L.; Dawes, J. M.; Xi, P.; Piper, J. A.; Goldys, E. M.; Monro, T. M. Single-nanocrystal Sensitivity Achieved by Enhanced Upconversion Luminescence. *Nat. Nanotechnol.* **2013**, *8* (10), 729–734. DOI: 10.1038/nnano.2013.171.

[31] Gargas, D. J.; Chan, E. M.; Ostrowski, A. D.; Aloni, S.; Altoe, M. V. P.; Barnard, E. S.; Sanii, B.; Urban, J. J.; Milliron, D. J.; Cohen, B. E.; Schuck, P. J. Engineering bright sub-10-nm Upconverting Nanocrystals for Single-molecule Imaging. *Nat. Nanotechnol.* **2014**, *9* (4), 300–305. DOI: 10.1038/nnano.2014.29.

[32] Chen, G.; Ågren, H.; Ohulchanskyy, T. Y.; Prasad, P. N. Light Upconverting Core-shell Nanostructures: Nanophotonic Control for Emerging Applications. *Chem. Soc. Rev.* **2015**, *44* (6), 1680–1713. DOI: 10.1039/c4cs00170b.

[33] Shen, B.; Cheng, S.; Gu, Y.; Ni, D.; Gao, Y.; Su, Q.; Feng, W.; Li, F. Revisiting the Optimized Doping Ratio in Core/Shell Nanostructured Upconversion Particles. *Nanoscale* **2017**, *9* (5), 1964–1971. DOI: 10.1039/c6nr07687d.

[34] Gao, W.; Sun, Z.; Han, Q.; Han, S.; Cheng, X.; Wang, Y.; Yan, X.; Dong, J. Enhancing Upconversion Emission of Er3+ in Single β-$NaYF_4$ Microrod Through Constructing Different Inert and Active Shells With Doping Yb^{3+} Ions. *J. Alloys Compd.* **2021**, *857*, 157578. DOI: 10.1016/j.jallcom.2020.157578.

[35] Johnson, N. J. J.; He, S.; Diao, S.; Chan, E. M.; Dai, H.; Almutairi, A. Direct Evidence for Coupled Surface and Concentration Quenching Dynamics in Lanthanide-Doped Nanocrystals. *J. Am. Chem. Soc.* **2017**, *139* (8), 3275–3282. DOI: 10.1021/jacs.7b00223.

[36] Wang, Z.; Meijerink, A. Concentration Quenching in Upconversion Nanocrystals. *J. Phys. Chem. C* **2018**, *122* (45), 26298–26306. DOI: 10.1021/acs.jpcc.8b09371.

[37] Liu, Q.; Zhang, Y.; Peng, C. S.; Yang, T.; Joubert, L.-M.; Chu, S. Single Upconversion Nanoparticle Imaging at Sub-10 W cm^{-2} Irradiance. *Nat. Photonics* **2018**, *12* (9), 548–553. DOI: 10.1038/s41566-018-0217-1.

[38] Chen, B.; Kong, W.; Wang, N.; Zhu, G.; Wang, F. Oleylamine-Mediated Synthesis of Small $NaYbF_4$ Nanoparticles with Tunable Size. *Chem. Mater.* **2019**, *31* (13), 4779–4786. DOI: 10.1021/acs.chemmater.9b01050.

[39] Meng, Z.; Zhang, S.; Wu, S. Power Density Dependent Upconversion Properties of NaYbF4: Er^{3+}@NaYbF4: Tm^{3+}@$NaYF_4$ Nanoparticles and Their Application in White-light Emission LED. *J. Lumin.* **2020**, *227*, 117566. DOI: 10.1016/j.jlumin.2020.117566.

[40] Tian, B.; Fernandez-Bravo, A.; Najafiaghdam, H.; Torquato, N. A.; Altoe, M. V. P.; Teitelboim, A.; Tajon, C. A.; Tian, Y.; Borys, N. J.; Barnard, E. S.; Anwar, M.; Chan, E. M.; Schuck, P. J.; Cohen, B. E. Low Irradiance Multiphoton Imaging with Alloyed Lanthanide Nanocrystals. *Nat. Commun.* **2018**, *9* (1), 3082. DOI: 10.1038/s41467-018-05577-8.

[41] Förster, T. Zwischenmolekulare Energiewanderung und Fluoreszenz. Annalen der Physik, 437(1-2), 55-75. *Ann. Phys.* **1948**, *437* (1-2), 55–75. DOI: 10.1002/ANDP.19484370105.

[42] Wang, F.; Deng, R.; Wang, J.; Wang, Q.; Han, Y.; Zhu, H.; Chen, X.; Liu, X. Tuning Upconversion Through Energy Migration in Core-shell Nanoparticles. *Nat. Mater.* **2011**, *10* (12), 968–973. DOI: 10.1038/nmat3149.

[43] Chen, X.; Jin, L.; Kong, W.; Sun, T.; Zhang, W.; Liu, X.; Fan, J.; Yu, S. F.; Wang, F. Confining Energy Migration in Upconversion Nanoparticles Towards Deep Ultraviolet Lasing. *Nat. Commun.* **2016**, *7*, 10304. DOI: 10.1038/ncomms10304.

[44] Mei, Q.; Bansal, A.; Jayakumar, M. K. G.; Zhang, Z.; Zhang, J.; Huang, H.; Yu, D.; Ramachandra, C. J. A.; Hausenloy, D. J.; Soong, T. W.; Zhang, Y. Manipulating Energy Migration within Single Lanthanide Activator for Switchable Upconversion Emissions Towards Bidirectional Photoactivation. *Nat. Commun.* **2019**, *10* (1), 4416. DOI: 10.1038/s41467-019-12374-4.

[45] Xu, L.; Liu, Y.; Zhou, Z.; Sun, X.; Ud Din, I.; Khan, F.; Li, Y.; Li, H.; Ren, J.; Carvajal, J. J.; Zhang, J.; Liu, L. A New Role of Yb^{3+}-An Energy Reservoir for Lanthanide Upconversion Luminescence. *Nanoscale* **2021**, *13* (22), 9978–9988. DOI: 10.1039/d0nr08205h.

[46] Zhou, B.; Huang, J.; Yan, L.; Liu, X.; Song, N.; Tao, L.; Zhang, Q. Probing Energy Migration Through Precise Control of Interfacial Energy Transfer in Nanostructure. *Adv. Mater.* **2019**, *31* (6), e1806308. DOI: 10.1002/adma.201806308.

[47] Wiesholler, L. M.; Frenzel, F.; Grauel, B.; Würth, C.; Resch-Genger, U.; Hirsch, T. Yb,Nd,Er-doped Upconversion Nanoparticles: 980 nm versus 808 nm Excitation. *Nanoscale* **2019**, *11* (28), 13440–13449. DOI: 10.1039/c9nr03127h.

[48] Wang, J.; Deng, R.; MacDonald, M. A.; Chen, B.; Yuan, J.; Wang, F.; Chi, D.; Hor, T. S. A.; Zhang, P.; Liu, G.; Han, Y.; Liu, X. Enhancing Multiphoton Upconversion Through Energy Clustering at Sublattice Level. *Nat. Mater.* **2014**, *13* (2), 157–162. DOI: 10.1038/nmat3804.

[49] Zhou, J.; Li, C.; Li, D.; Liu, X.; Mu, Z.; Gao, W.; Qiu, J.; Deng, R. Single-molecule Photoreaction Quantitation Through Intraparticle-surface Energy Transfer (i-SET) Spectroscopy. *Nat. Commun.* **2020**, *11* (1), 4297. DOI: 10.1038/s41467-020-18223-z.

[50] Chen, Q.; Xie, X.; Huang, B.; Liang, L.; Han, S.; Yi, Z.; Wang, Y.; Li, Y.; Fan, D.; Huang, L.; Liu, X. Confining Excitation Energy in Er^{3+}-Sensitized Upconversion Nanocrystals through Tm^{3+}-Mediated Transient Energy Trapping. *Angew. Chem., Int. Ed.* **2017**, *56* (26), 7605–7609. DOI: 10.1002/anie.201703012.

[51] Sun, T.; Li, Y.; Ho, W. L.; Zhu, Q.; Chen, X.; Jin, L.; Zhu, H.; Huang, B.; Lin, J.; Little, B. E.; Chu, S. T.; Wang, F. Integrating Temporal and Spatial Control of Electronic Transitions for Bright Multiphoton Upconversion. *Nat. Commun.* **2019**, *10* (1), 1811. DOI: 10.1038/s41467-019-09850-2.

[52] Shang, Y.; Hao, S.; Lv, W.; Chen, T.; Tian, L.; Lei, Z.; Yang, C. Confining Excitation Energy of Er^{3+}-Sensitized Upconversion Nanoparticles Through Introducing Various Energy Trapping Centers. *J. Mater. Chem. C* **2018**, *6* (15), 3869–3875. DOI: 10.1039/C7TC05742C.

[53] Wilhelm, S.; Kaiser, M.; Würth, C.; Heiland, J.; Carrillo-Carrion, C.; Muhr, V.; Wolfbeis, O. S.; Parak, W. J.; Resch-Genger, U.; Hirsch, T. Water Dispersible Upconverting Nanoparticles: Effects of Surface Modification on their Luminescence and Colloidal Stability. *Nanoscale* **2015**, *7* (4), 1403–1410. DOI: 10.1039/c4nr05954a.

[54] Yan, J.; Li, B.; Yang, P.; Lin, J.; Dai, Y. Progress in Light‐Responsive Lanthanide Nanoparticles Toward Deep Tumor Theranostics. *Adv. Funct. Mater.* **2021**, *31* (42), 2104325. DOI: 10.1002/adfm.202104325.

[55] Ding, F.; Zhan, Y.; Lu, X.; Sun, Y. Recent Advances in Near-infrared II Fluorophores for Multifunctional Biomedical Imaging. *Chem. Sci.* **2018**, *9* (19), 4370–4380. DOI: 10.1039/c8sc01153b.

[56] Wang, X.; Valiev, R. R.; Ohulchanskyy, T. Y.; Ågren, H.; Yang, C.; Chen, G. Dye-sensitized Lanthanide-doped Upconversion Nanoparticles. *Chem. Soc. Rev.* **2017**, *46* (14), 4150–4167. DOI: 10.1039/C7CS00053G.

[57] Carnall, W. T.; Crosswhite, H.; Crosswhite, H. M. *Energy Level Structure and Transition Probabilities in the Spectra of the Trivalent Lanthanides in LaF₃*, Argonne National Laboratory, Argonne, IL, 1978.

[58] Strohhöfer, C.; Polman, A. Absorption and Emission Spectroscopy in Er^{3+}–Yb^{3+} doped Aluminum Oxide Waveguides. *Opt. Mater.* **2003**, *21* (4), 705–712. DOI: 10.1016/S0925-3467(02)00056-3.

[59] Rabouw, F. T.; Prins, P. T.; Villanueva-Delgado, P.; Castelijns, M.; Geitenbeek, R. G.; Meijerink, A. Quenching Pathways in $NaYF_4$:Er^{3+},Yb^{3+} Upconversion Nanocrystals. *ACS Nano* **2018**, *12* (5), 4812–4823. DOI: 10.1021/acsnano.8b01545.

[60] Würth, C.; Kaiser, M.; Wilhelm, S.; Grauel, B.; Hirsch, T.; Resch-Genger, U. Excitation Power Dependent Population Pathways and Absolute Quantum Yields of Upconversion Nanoparticles in Different Solvents. *Nanoscale* **2017**, *9* (12), 4283–4294. DOI: 10.1039/c7nr00092h.

[61] Berry, M. T.; May, P. S. Disputed Mechanism for NIR-to-Red Upconversion Luminescence in $NaYF_4$:Yb^{3+},Er^{3+}. *J. Phys. Chem. A* **2015**, *119* (38), 9805–9811. DOI: 10.1021/acs.jpca.5b08324.

[62] Lee, C.; Park, H.; Kim, W.; Park, S. Origin of Strong Red Emission in Er^{3+}-based Upconversion Materials: Role of Intermediate States and Cross Relaxation. *Phys. Chem. Chem. Phys.* **2019**, *21* (43), 24026–24033. DOI: 10.1039/c9cp04692e.

[63] Hossan, M. Y.; Hor, A.; Luu, Q.; Smith, S. J.; May, P. S.; Berry, M. T. Explaining the Nanoscale Effect in the Upconversion Dynamics of β-$NaYF_4$:Yb^{3+},Er^{3+} Core and Core–Shell Nanocrystals. *J. Phys. Chem. C* **2017**, *121* (30), 16592–16606. DOI: 10.1021/acs.jpcc.7b04567.

[64] Zuo, J.; Sun, D.; Tu, L.; Wu, Y.; Cao, Y.; Xue, B.; Zhang, Y.; Chang, Y.; Liu, X.; Kong, X.; Buma, W. J.; Meijer, E. J.; Zhang, H. Precisely Tailoring Upconversion Dynamics via Energy Migration in Core-Shell Nanostructures. *Angew. Chem., Int. Ed.* **2018**, *57* (12), 3054–3058. DOI: 10.1002/anie.201711606.

[65] Jacques, S. L. Optical Properties of Biological Tissues: A Review. *Phys. Med. Biol.* **2013**, *58* (11), R37-61. DOI: 10.1088/0031-9155/58/11/R37.

[66] Ormond, A. B.; Freeman, H. S. Dye Sensitizers for Photodynamic Therapy. *Materials* **2013**, *6* (3), 817–840. DOI: 10.3390/ma6030817.

[67] Press, W. H.; Teukolsky, S. A. Savitzky-Golay Smoothing Filters. *Comput. Phys.* **1990**, *4* (6), 669. DOI: 10.1063/1.4822961.

[68] Braslavsky, S. E. Glossary of Terms Used in Photochemistry, 3rd edition (IUPAC Recommendations 2006). *Pure Appl. Chem.* **2007**, *79* (3), 293–465. DOI: 10.1351/pac200779030293.

4 Bilayer-Coating Strategy for Hydrophobic Nanoparticles Providing Colloidal Stability, Functionality, and Surface Protection in Biological Media

4.1 Abstract

The surface chemistry of nanoparticles is a key step on the pathway from particle design towards applications in biologically relevant environments. Here, a bilayer-based strategy for the surface modification of hydrophobic nanoparticles is introduced that leads to excellent colloidal stability in aqueous environments and good protection against disintegration, while permitting surface functionalization *via* simple carbodiimide chemistry. We have demonstrated the excellent potential of this strategy using upconversion nanoparticles (UCNPs), initially coated with oleate and therefore dispersible only in organic solvents. The hydrophobic oleate capping is maintained and a bilayer is formed upon addition of excess oleate. The bilayer approach renders protection towards luminescence loss by water quenching, while the incorporation of additional molecules containing amino functions yields colloidal stability and facilitates the introduction of functionality. The biological relevance of the approach was confirmed with the use of two model dyes, a photosensitizer and a nitric oxide (NO) probe that, when attached to the surface of the UCNPs, retained their functionality to produce singlet oxygen and detect intracellular NO, respectively. We present a simple and fast strategy to protect and functionalize inorganic nanoparticles in biological media, which is important for controlled surface engineering of nanosized materials for theranostic applications.

4.2 Introduction

Nanomaterials are attractive for tracking biomacromolecules not only because of their exceptional physicochemical properties but also since they are similar in size. Their high surface-to-volume ratio is beneficial for functionalization with receptors, sensors, or drugs.[1–3] At the same time, this feature bears the greatest challenge of nanomaterials, as it comes along with a high tendency of agglomeration.[4] Thus, functionalization strategies are desirable that protect particles from agglomeration in biological environments and still allow the particle surface to be modified with different molecules in a targeted manner.[5]

Upconversion nanoparticles (UCNPs) convert low-energy near-infrared (NIR) light into higher-energy visible or UV light. They typically consist of $NaYF_4$ host lattices doped with trivalent lanthanide ions. In most cases, a system of two lanthanide ions is used, a sensitizer ion with strong NIR-absorption (*e.g.*, Yb^{3+}, Nd^{3+}) and an activator ion that has a variety of energy levels, which are populated by the sequential absorption of more than one photon (*e.g.*, Er^{3+}, Tm^{3+}, Ho^{3+}). The transfer of the energy of two or more photons from the sensitizer ions to an activator ion enables the upconversion process.[6–9] High temperatures are required to form hexagonal, monodisperse UCNPs, therefore synthesis protocols utilizing temperature-stable rare-earth-oleates in high boiling organic solvents have been established. Consequently, these oleate-stabilized particles are hydrophobic and therefore dispersible only in organic solvents.[10,11] The same applies to many other nanosized probes, regardless of whether they are luminescent (*e.g.*, quantum dots) or magnetic (*e.g.*, superparamagnetic iron oxide particles). To date, many strategies have been proposed to elegantly facilitate transfer into an aqueous environment.[12,13] UCNPs that are aimed for biomedical applications should exhibit colloidal stability and have the potential to be functionalized with receptors or reporter molecules, or with therapeutic agents.[5] The simplest particle modification strategy is based on ligand exchange, in which the oleate is first removed in the presence of nitrosyl tetrafluoroborate or acid, while the desired ligand is added during a second modification step.[14,15] This method has gained great popularity because of its capability to use a wide variety of ligands, ranging from small molecules to large polymers.[16,17] Despite the great charm of its simplicity, this method comes with a downside: it is almost impossible to adequately protect the surface of the particle through the ligand exchange, *i.e.*, to cover it so completely that no further unwanted binding of other molecules present in the solution is possible later. Molecules with functional groups such as $-SO_4$, $-COOH$, $-NH_2$, or $-H_2PO_3$ occupy free binding sites or

even displace ligands, which can also lead to particle aggregation in addition to a changed functionality.[17,18] Water molecules can diffuse to the weakly protected particle surface, which greatly impairs the upconversion effect due to quenching or disintegration effects.[12,17,19–21] These drawbacks have been overcome with ligand modifications in which the oleate ligand remains on the particle surface and an amphiphilic coating, such as amphiphilic polymers, is added to aid water dispersibility while providing a hydrophobic barrier to protect the particle surface from quenching and dissolution.[22,23] The preparation of such protected systems is usually time-consuming, as many parameters have to be carefully adjusted to prevent the polymer from unwanted cross-linking, potentially leading to particle aggregation.[24–26] Alternatively, phospholipids can be used as amphiphiles to obtain biocompatible, bright, and colloidally stable UCNPs; however, this method is also laborious, expensive, and results often in low yield.[27,28]

As an alternative, we present a fast and simple surface modification strategy that disperses nanoparticles in aqueous media, ensures bright upconversion luminescence and colloidal stability, and allows easy further functionalization (Figure 4.1). The procedure starts with oleate-coated UCNPs of any size between 10 and 50 nm dispersed in an organic solvent. The particles are then added to an aqueous suspension of sodium oleate and dodecylamine where, under mild conditions (1 h, 60 °C), the amphiphilic molecules interact with the hydrophobic alkyl chains on the particle surface forming a bilayer. The addition of dodecylamine in the bilayer formation allows for later functionalization.
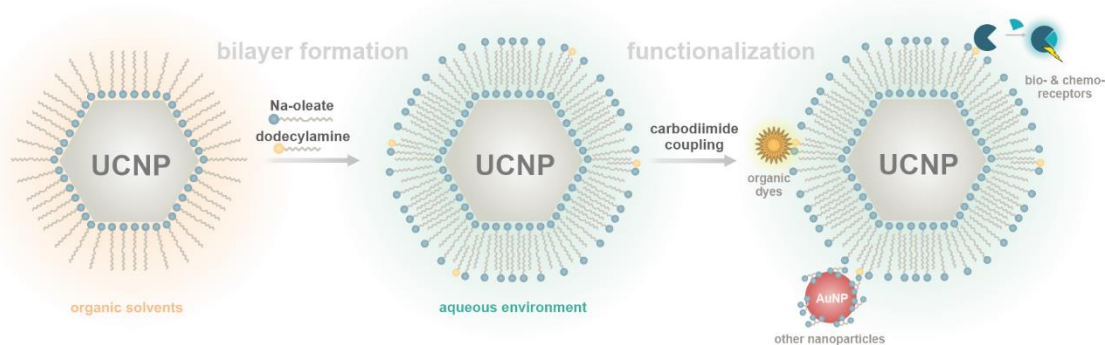

Figure 4.1. Particle modification strategy: transfer of oleate-capped UCNPs from a nonpolar environment into an aqueous environment by bilayer formation with the possibility of further functionalization.

4.3 Results and Discussion

Oleate-coated UCNPs (UCNPs@oleate) of the type $NaYbF_4(20\%Er)@NaYF_4$ with a diameter of (23.3 ± 1.7) nm (Figures 4.2a and S4.1), were synthesized according to a previously published protocol.[29] The UCNPs@oleate, initially dispersed in cyclohexane $(31.2$ mg mL^{-1}) were added to an aqueous mixture of sodium oleate $(50$ mg mL^{-1}) and dodecylamine $(15$ mg mL^{-1} in DMSO). The transfer of the UCNPs@oleate from the organic phase to the aqueous phase took place within seconds as observed monitoring the upconversion luminescence upon excitation with a NIR handheld-laser. The initial slightly turbid solution became clear after evaporation of the cyclohexane, indicating that the particles were surrounded by the amphiphilic molecules and therefore were stable in the aqueous phase. In contrast, if UCNPs@oleate were added to water without the presence of amphiphilic molecules, the particles agglomerated and precipitated immediately. Following purification, the formation of a uniform bilayer is confirmed by transmission electron microscopy (TEM) images recorded on negatively stained grids (Figure 4.2b). A hydrodynamic diameter of (36.4 ± 0.6) nm (polydispersity index (PDI) = 0.147 ± 0.006) verifies that micelles with multiple individual particles were not formed (Figure 4.2c). High upconversion luminescence losses are usually observed when changing the solvent from organic to aqueous media.[19] Here, 65% of the upconversion luminescence of the UCNPs@oleate in cyclohexane was preserved after transfer to water (Figure 4.2d). In contrast, unprotected UCNPs (UCNPs@BF$_4^-$) in water retained only 22% of their original upconversion luminescence. This demonstrates the exceptional ability of the bilayer strategy to efficiently shield the particle surface from the solvent. To prove that this bilayer modification is also suitable for long-term storage, the particles were freeze-dried and characterized following redispersion in water. Dynamic light scattering (DLS) results confirmed that the UCNPs remained monodisperse (Figure S4.2). The UCNPs@bilayer exhibited a negative zeta potential of (-57 ± 4) mV and showed good colloidal stability in cell media and in the presence of high ionic strength (Figure S4.3). Under physiological conditions, significant agglomeration was only observed in the presence of high Ca^{2+} concentrations $(1.8$ mM). This is most likely due to the divalent character of the ion and the consequently stronger influence on the colloidal stability. In comparison to the also divalent Mg^{2+}, Ca^{2+} shows a weaker formation of hydrate shells and with this a higher reactivity towards counterions such as the oleate on the surface of the nanoparticles. [30,31]
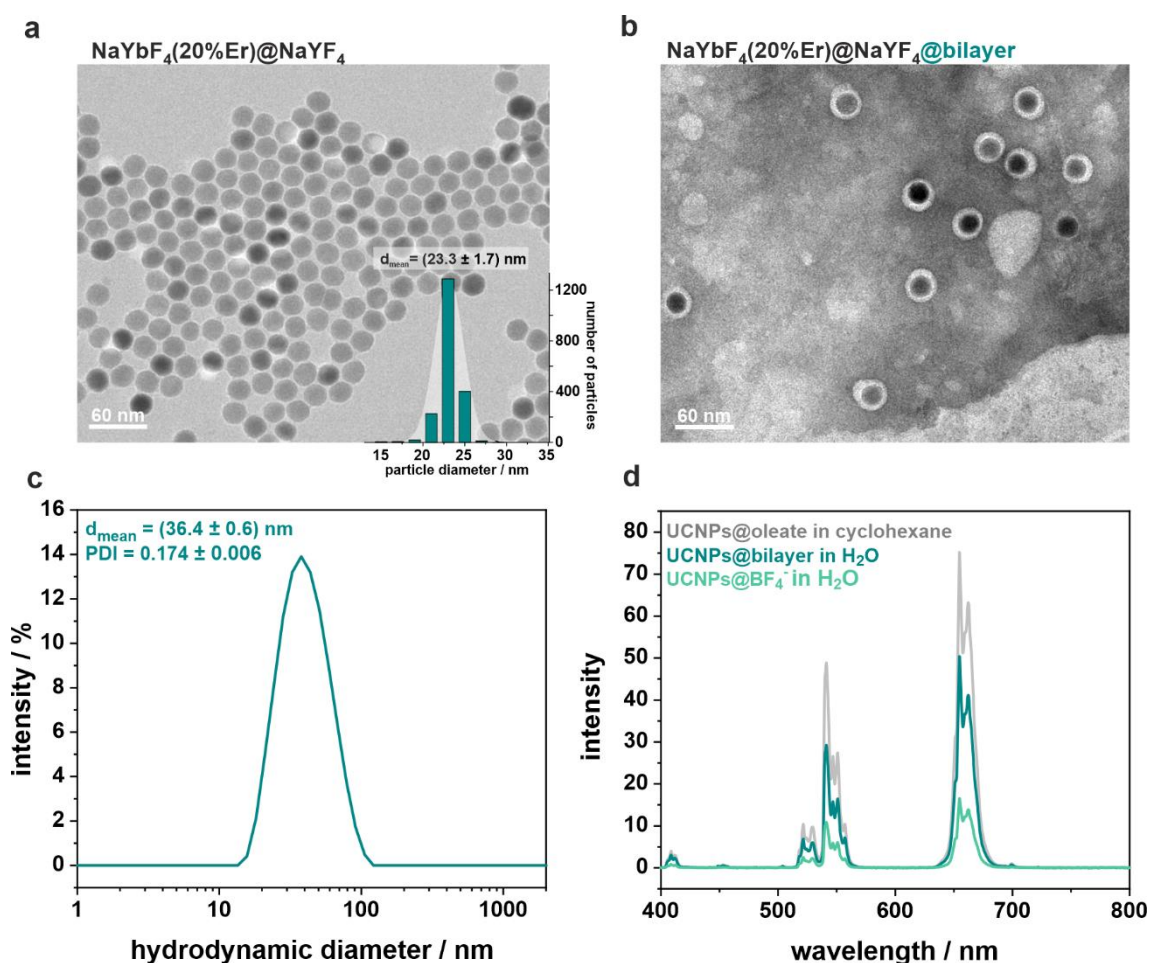
Figure 4.2. (a) TEM micrograph and corresponding particle-size-distribution of NaYbF$_4$(20%Er)@NaYF$_4$ (UCNPs@oleate). (b) TEM micrograph of the same UCNPs after bilayer formation (UCNPs@bilayer). The TEM grid was negatively stained with phosphotungstic acid. (c) DLS of UCNPs@bilayer in H$_2$O. (d) Upconversion luminescence of UCNPs@oleate in cyclohexane, UCNPs@bilayer in H$_2$O and UCNPs@BF$_4^-$ in H$_2$O, where the oleate was removed *via* ligand exchange.[12] All surface modifications shown were performed using the same batch of NaYbF$_4$(20%Er)@NaYF$_4$, which were characterized in (a). Spectra (λ_{exc} = 980 nm at 140 W cm^{-2}) were normalized to the mass concentration determined by ICP-OES (for more details, see SI).

The incorporation of organic molecules is often required to introduce additional functionality to the particles and, consequently, improve their applicability. This should be achieved without losing colloidal stability. Since both carboxyl groups and amino groups are available on the UCNPs@bilayer, carbodiimide-coupling chemistry can be easily applied (Figure 4.3). The coupling of a carboxyl group to the UCNPs was demonstrated using the photosensitizer Rose Bengal (RB) as model molecule. An RB-NHS-ester derivative was prepared and reacted with the UCNPs@bilayer (Figure 4.3, top). The particles were purified *via* centrifugation to remove unbound RB-NHS ester molecules.
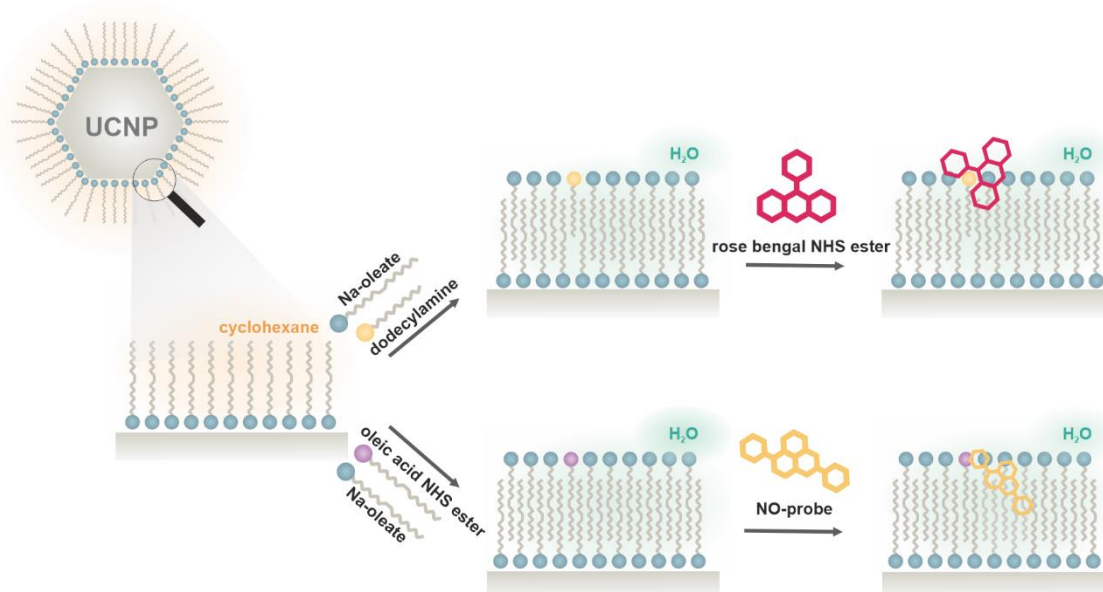
Figure 4.3. Carbodiimide-chemistry-based strategies for functionalization of UCNPs@bilayer with organic dyes containing a carboxy function (top) or an amino function (bottom).

Especially for FRET-based nanosystems, it is desirable to control the dye-loading of the UCNPs surface. The challenge is to find a compromise between sufficient signal intensities and self-quenching at too high concentrations. A plethora of surface modification strategies reported in the literature to date allow only little control of this property.[32–34] In the case of bilayer modification, two strategies can be followed to adjust the amount of dye: (1) varying the ratio of UCNP : dye in the coupling protocol, or (2) controlling the ratio of sodium oleate : dodecylamine during bilayer formation. When attaching RB to the UCNPs, the possibility of controlling the amount of dye on the particle by varying the ratio of UCNPs to RB in the coupling step was confirmed by absorbance measurements (Figure 4.4). The colloidal stability of the particles was not affected by the attachment of the organic dye as only a slight increase in the hydrodynamic diameter was observed for the particles with the highest number of attached dye molecules (Figure S4.4a). When comparing the systems containing different amounts of RB, no clear difference in the luminescence measurements was observed under 980 nm excitation. In addition, the emission corresponding to RB at about 600 nm indicates radiative or non-radiative energy transfer from UCNP to RB either *via* FRET or reabsorption (Figure S4.4b).

Different UCNPs@bilayer systems with varying percentages of dodecylamine (5%, 10%, 15%, 20%) and the respective added constant amount of activated RB were synthesized to examine whether RB was covalently attached to the amine groups in the bilayer and not only intercalated between the amphiphilic molecules. The increase in the absorbance of RB with higher amounts of dodecylamine suggests that

a binding of the dye to the amine groups is taking place (Figure S4.5a). These results also support that the degree of functionalization can be easily adjusted *via* the amine content in the bilayer. However, an optimal colloidal stability was found for UCNPs@bilayer with 10 mol % dodecylamine (Figure S4.5b).
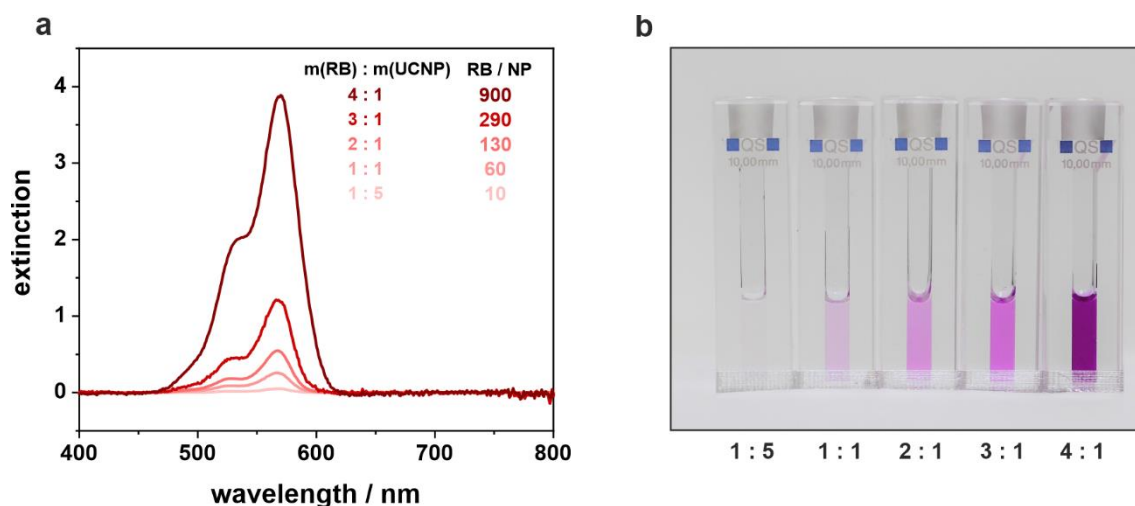

Figure 4.4. (a) Extinction spectra and calculated number of RB molecules per nanoparticle of UCNPs@bilayer-RB with different ratios of m(RB) : m(UCNPs). The spectra are normalized to the mass concentration of UCNPs (1.0 mg mL^{-1}) as for some of the samples (4 : 1 and 3 : 1) dilution was required. (b) UCNPs@bilayer-RB dispersions with different ratios of m(RB) : m(UCNPs).

The number of organic dyes and molecules with potential pharmacological properties that contain terminal amine groups is extensive, so expanding the application of the UCNPs@bilayer to support this type of molecule is paramount. As a proof-of-concept study, the bilayer was formed using activated oleate (oleate-NHS-ester) along with non-activated oleate and an amine derivative of the nitric oxide (NO)-sensitive dye DANPY-NO,[35] referred to herein as the *NO-probe* (Scheme 2, bottom). This two-photon excitable molecular probe has shown excellent performance for the detection of NO in a broad range of cells, including human macrophages and endothelial cells.[35,36] The functionalization of UCNPs@bilayer with the NO-probe, motivated by the potential that a NIR-excitable ratiometric nanoprobe could have for biological applications, was achieved by a coupling reaction to previously carbodiimide-activated oleate molecules (1 mol % of total oleate), which were present during the bilayer formation. The resulting UCNPs@bilayer-NO-probe were characterized by a monodisperse size distribution with a hydrodynamic diameter of (36 ± 2) nm (Figure S4.6a). A control experiment, in which a NO-probe was added to the reaction mixture without pre-activation of the oleate, resulted in unstable particles without labelling confirming the covalent interaction between the NO-probe and the oleate (Figure S4.7). The UCNPs@bilayer-NO-probe exhibited the characteristic absorption maximum (Figure S4.6b), and fluorescence excitation

(Figure S4.6c) and emission (Figure S4.6d) of the NO-probe, confirming the successful functionalization.

Since the oleate-based bilayer of the UCNP surface offers good protection against hydrophilic molecules and thus ions have a low affinity to diffuse through the hydrophobic barrier, biomolecules are unlikely to replace the oleate on the nanoparticle surface and induce nanoparticle aggregation. Additionally, electrostatic repulsions further stabilize the particles as indicated by the high zeta potentials of the systems ((-44.5 ± 0.5) mV for UCNPs@bilayer-RB (see Figure S4.8 for full nanoparticle characterization) and (-42.6 ± 0.6) mV for UCNPs@bilayer-NO-probe). To check the colloidal stability under biological conditions, these particle systems were dispersed in cell medium (DMEM +10% FCS) showing no agglomeration after 72 h (Figure S4.9) and demonstrating the applicability of such modified UCNPs under biological conditions.

The ability of UCNPs@bilayer-RB to generate singlet oxygen *via* indirect NIR excitation of the UCNPs was confirmed by the decrease in fluorescence emission intensity of the singlet oxygen probe 9,10-anthracenedipropionic acid (ADPA) upon 980 nm irradiation (Figure 4.5a). No singlet oxygen production was observed for the free RB when excited with NIR light, further indicating the energy transfer from the nanoparticles to the RB. The ability of the NO-probe to detect NO once bound to the surface of the UCNPs@bilayer particles was demonstrated using diethylamine NONOate as a NO donor. As expected, the fluorescence emission intensity of the probe increased in the presence of NO (Figure 4.5b). To further confirm the NO-sensing ability of the UCNPs@bilayer-NO-probe, their potential to monitor intracellular levels of NO was investigated. As shown by confocal laser scanning microscopy images and corresponding intracellular spectra (Figure S4.10a and b, respectively), the nanoprobe was successfully internalized by RAW264.7γ NO⁻ cells. The high cell survival rates at the concentrations tested, indicate the great biocompatibility of the UCNPs@bilayer-NO-probe (Figure S4.10c).

To evaluate the ability of the nanoprobe, which accumulated in the lysosomes of the tested cells (Figure S4.10d), to detect NO, two pathways of NO production in RAW264.7γ NO⁻ cells were examined: endogenous and exogenous. NO was endogenously produced by RAW264.7γ NO⁻ macrophages following stimulation with lipopolysaccharide (LPS) and interferon-gamma (IFN-γ) and exogenous NO was released by treating the cells with the NO-donor *S*-nitroso-*N*-acetylpenicillamine (SNAP). In both cases, strong intensity changes of the NO-probe fluorescence emission were observed in the presence of NO (Figure 4.5c and d, and Figure S4.11),

suggesting that NO detection is indeed possible by the UCNPs@bilayer-NO-probe. Additionally, the selective detection of NO by the particles was proven using a NO synthase inhibitor (N(ω)-nitro-L-arginine methyl ester, L-NAME), which blocked the endogenous production of NO resulting in the decrease of the fluorescence emission intensity. This is the first indication that the bilayer coating is still intact, even after being taken up by biological cells.
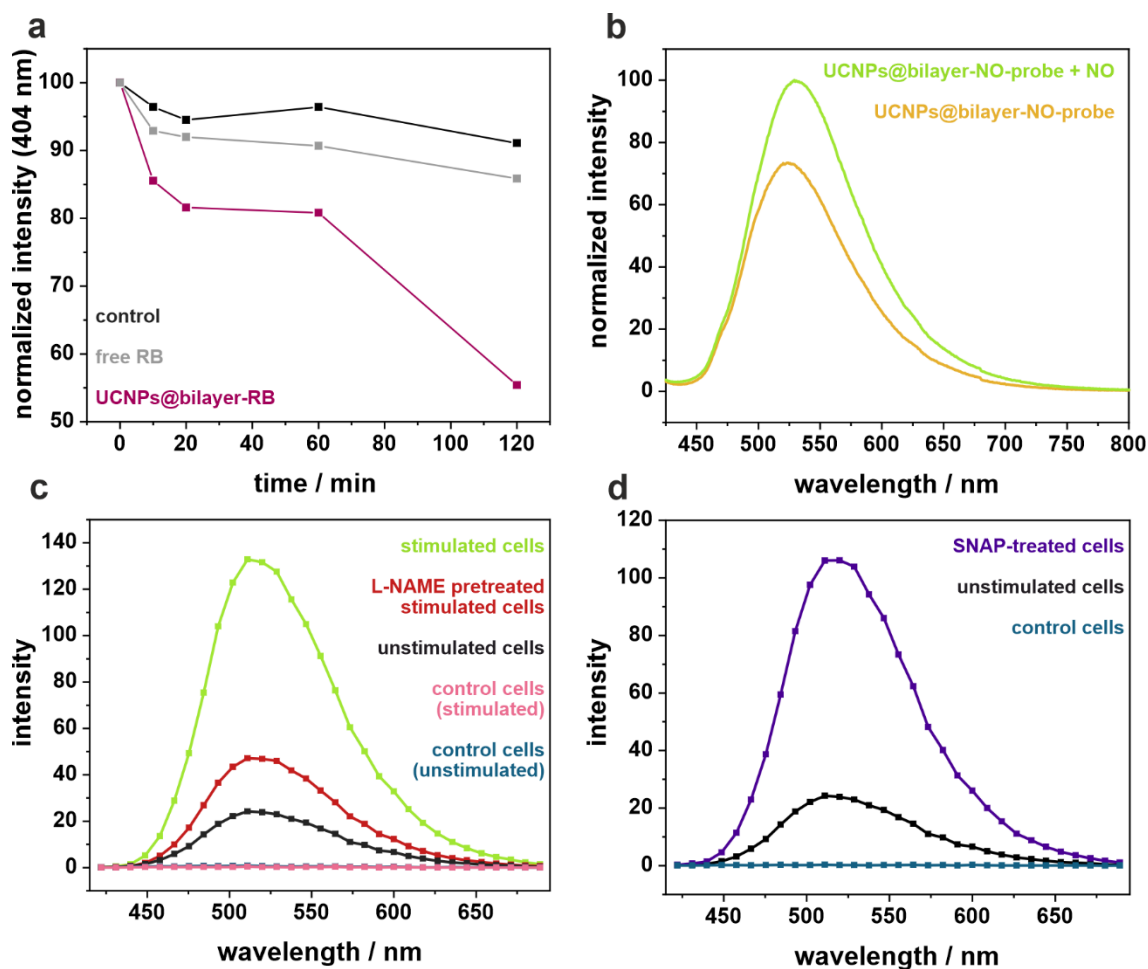
Figure 4.5. (a) Singlet oxygen generation at different time periods of 980 nm irradiation detected by monitoring the fluorescence bleaching of ADPA excited at 390 nm. Normalized fluorescence decays of ADPA in the presence of UCNPs@bilayer-RB (pink), free RB (gray), and the corresponding control of only ADPA (black) in H_2O. (b) Normalized fluorescence emission spectra of UCNPs@bilayer-NO-probe (100 µg mL^{-1}) before (yellow) and following (green) addition of NONOate (1.5 mM); λ_{exc} = 405 nm. (c and d) Intracellularly recorded fluorescence emission spectra (λ_{exc} = 405 nm) of RAW264.7γ NO$^-$ cells incubated with UCNPs@bilayer-NO-probe (25 µg mL^{-1}, 3 h) and treated under the following conditions: (c) unstimulated(black), stimulated with LPS (0.7 µg mL^{-1}) and IFN-γ (17 µg mL^{-1}) (green) and pre-treated L-NAME and stimulated with LPS (0.7 µg mL^{-1}) and IFN-γ (17 µg mL^{-1}) (red); and (d) unstimulated (black), treated with SNAP (275 µM, 1 h, purple). Control unstimulated cells (blue in (c) and (d)) and control stimulated cells (pink in (c)) were also recorded.

The precise arrangement of the bilayer on the nanoparticle surface remains unclear since the incorporated amines appear to have an impact on the colloidal stability of the particles. This phenomenon was studied with different sized UCNPs and with different types of amines, which confirms that the stability is influenced by the presence and type of amine (Figure S4.12, Table S4.1). For example, for 23 nm particles, small hydrodynamic diameters and low PDIs were only observed for bilayer modifications including 10 mol % dodecylamine (Figure S4.12b). If no amine or other amines (octylamine, oleylamine) were incorporated into the bilayer, the particle size distributions indicated aggregate formation. The same effect was observed for smaller UCNPs (13 nm, Figure S4.12a), while the influence of the amine tends to become negligible for larger particles (Figure S4.12c). Comparing small and large UCNPs, it is known that small particles usually have a quasi-spherical shape and therefore large curvature, while the hexagonal prismatic shape usually evolves for larger particles.[37,38] This shape changing effect is also evident by TEM studies (Figure S4.13). With regard to bilayer formation, a large curvature is disadvantageous because gaps can be expected between the oleate molecules.[39] It is conceivable that the offered amine molecules fill the gaps and thus increase the stability of the UCNPs@bilayer. This is a phenomenon already known from catanionic surfactant mixtures consisting of fatty acids and amines, which form extremely stable colloidal structures due to the decrease in the average ion head size and hence increasing packing parameters.[40,41] For geometric and electrostatic reasons, these colloidal structures are strongly dependent on the chain length of the surfactant and the molar ratio anion : cation, which could explain the widely different results for the distinctive kind of amines.[40] The stabilizing function of dodecylamine appears to be more important for small, highly curved particles. For larger UCNPs, the crystal edges are probably the most critical spots, as this is where a gap between the oleate molecules is to be expected. To verify this hypothesis, citrate-coated gold nanoparticles (AuNPs@citrate, 16 nm) were attached to 60 nm × 48 nm UCNPs@bilayer *via* carbodiimide chemistry (Figure 4.6a). A clear tendency of the AuNPs to arrange predominantly on the edges than on the facets was observed in the TEM images. A control experiment with UCNPs@bilayer without amine showed no significant binding of AuNPs to the UCNPs, demonstrating the selective binding to the amine groups (Figure 4.6b). These results confirmed that the amines act as a gap filler stabilizing the bilayer. Incorporation of 10 mol % dodecylamine is a reasonable choice for all particle sizes between 10 and 50 nm and is therefore recommended for bilayer modifications and functionalization. However, the ratio oleate : dodecylamine may need to be adjusted for very small (<10 nm) or very large (>50 nm) particles to

address changes in the ratio of the total surface area to the total length of edges in the nanoparticle crystal. Furthermore, other amine-containing molecules, such as the NO-probe, can also be used to achieve stabilization *via* catanionic electrostatic interaction.
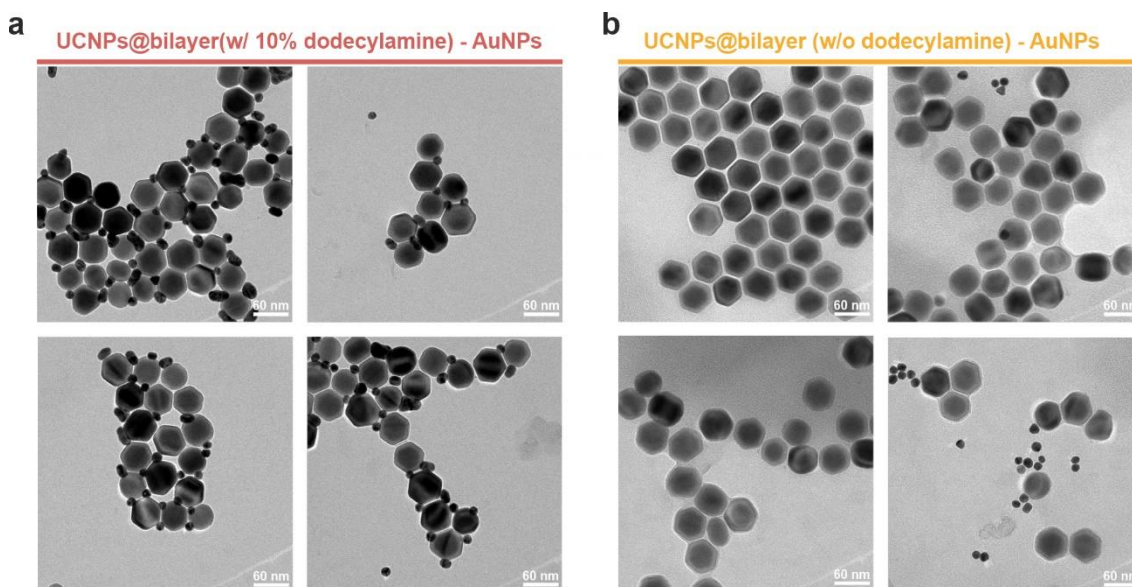
Figure 4.6. TEM images of UCNPs@bilayer (60 nm x 48 nm) coupled to AuNPs@citrate (16 nm). (a) UCNPs@bilayer with 10 mol % dodecylamine incorporated in the bilayer. (b) Negative control of UCNPs@bilayer without dodecylamine in the bilayer and AuNPs which were treated under the same coupling protocol.

4.4 Conclusion

The bilayer-strategy for simple surface modification and functionalization of hydrophobic nanoparticles yields hydrophilic and colloidally stable UCNPs. It was proven that dodecylamine has a positive, stabilizing function for the bilayer, which can be attributed to the positive effect of catanionics on the stability of colloids but also due to a gap-filling function. It was demonstrated that the attachment of organic dyes to UCNPs@bilayer is possible in a very simple manner by carbodiimide coupling chemistry. Two proof-of-concept studies are shown: one where singlet oxygen was generated under 980 nm irradiation after attachment of RB to the UCNPs, and another, where a NO-sensitive probe was coupled to the particle surface to monitor exogenous and endogenous intracellular levels of NO. These results demonstrate that bilayer-coatings retain the functionality and allow their application for *in vitro* studies.

4.5 Materials and Methods

4.5.1 Chemicals

Yttrium chloride hexahydrate ($YCl_3·6H_2O$, ≥ 99.9%) and ytterbium chloride hexahydrate ($YbCl_3·6H_2O$, ≥ 99.9%) were acquired from *Treibacher Industrie AG*. Sodium oleate (82%), erbium chloride hexahydrate ($ErCl_3·6H_2O$, ≥ 99,9%), 2-morpholin-4-ylethanesulfonic acid hydrate (MES hydrate, 99.5%), N-hydroxysuccinimide (NHS), nitrosyl tetrafluoroborate ($NOBF_4$, 95%), 1-ethyl-3-(3-dimethylaminopropyl)carbodiimide (EDC), Rose Bengal (RB, 95%), phosphotungstic acid hydrate (PTA), dodecylamine (98%), magnesium chloride (98%), gold(III)chloride trihydrate (≥ 99.9%), Dulbecco's Phosphate Buffered Saline (PBS, with and without $MgCl_2$ and $CaCl_2$), *S*-nitroso-*N*-acetylpenicillamine (SNAP), lipopolysaccharide (LPS), interferon-gamma (IFN-γ), N(ω)-nitro-L-arginine methyl ester (L-NAME) and diethylamine NONOate were from *Sigma Aldrich*. Oleic acid and 1-octadecene (technical grade, ≥90%) were purchased from *Alfa Aesar*. Ammonium fluoride (98%), sodium hydroxide and trisodium citrate dihydrate were from *Merck*. A multielement standard for ICP-OES measurements of the six elements Er, Gd, Nd, Tm, Y, and Yb, each 1,000 mg mL^{-1} (dissolved in 1.5 M HNO_3) was obtained from *Bernd Kraft GmbH*. Nitric acid (65%) was from *VWR Chemicals*. Tris-(hydroxymethyl)-aminomethan (TRIS) was from *Roche Diagnostics*. Calcium chloride (≥ 94%) was purchased from *Carl Roth*. Sulfuric acid (≥ 95%), cyclohexane (analytical reagent grade), chloroform (99,98%), dimethylformamide (DMF, ≥ 99.5%), dimethylsulfoxide (DMSO, ≥ 99.9%), methanol (MeOH, ≥ 99.9%) NaCl, KCl, 4-(2-hydroxyethyl)-1-piperazineethanesulfonic acid (HEPES), NaH_2PO_4, $NaHCO_3$, MeOH, L-glutamine (200 mM), phenol red-free Dulbecco's Modified Eagle Medium (DMEM) containing 4.5 g·L^{-1} D-glucose and fetal bovine serum (FBS) were received from *Fisher Scientific*. Anthracene-9,10-dipropionic acid disodium salt (ADPA) was from *Molecular Probes*. CellTiter Blue reagent was purchased from *Promega*. Deuterated dimethylsulfoxide (DMSO-d_6) and oleylamine (80-90%) were purchased from *Acros Organics*. Octylamine (>99%) was from *Fluka*. Penicillin-streptomycin (P-S) (100 U·mL^{-1} and 100 μL, respectively) and LysoTracker Red DND-99 (1 mM in DMSO) were purchased from *Invitrogen*. The RAW264.7γ NO$^-$ macrophages were purchased from *ATCC*. All chemicals were used without further purification. Double distilled water was used for aqueous solutions.

4.5.2 Preparation of Nanoparticles

4.5.2.1 Synthesis of Upconversion Nanoparticles

Upconversion nanoparticles of the type $NaYbF_4$(20%Er) were synthesized according to a previously published protocol.[29] For a 10 mmol batch size, $YbCl_3 \cdot 6H_2O$ (3,099.92 mg, 8 mmol) and $ErCl_3 \cdot 6H_2O$ (763.42 mg, 2 mmol) were dissolved in methanol (25 mL) and transferred into a three-necked round bottom flask. Oleic acid (82.6 mL) and 1-octadecene (100 mL) were added. The solution was heated to 110 °C under a nitrogen atmosphere, where vacuum was applied for 1 h. The flask was cooled to room temperature and ammonium fluoride (1,852 mg, 50 mmol), sodium oleate (6,469 mg, 21.25 mmol) and 1-octadecene (50 mL) were added. After applying vacuum for further 20 min, the mixture was degassed three times and heated to 315 °C under reflux (heating rate 16 °C min^{-1}). After 40 min, the flask was cooled to room temperature.

For purification, the nanoparticles were precipitated by adding an excess of ethanol and subsequently collected in a centrifuge (3,000 g, 5 min). After three redispersion/precipitation cycles using cyclohexane for redispersion and ethanol for precipitation, the particles were dispersed in cyclohexane (60 mL). Aggregates were removed *via* centrifugation (1,000 g, 5 min).

4.5.2.2 Synthesis of Core-Shell Nanoparticles

To enable core-shell synthesis, a shell precursor consisting of cubic $NaYF_4$ was prepared first. For a 10 mmol batch size, $YCl_3 \cdot 6H_2O$ (3,033.6 mg) was dissolved in methanol (25 mL). The solution was heated together with oleic acid (80 mL) and 1-octadecene (150 mL) to 160 °C in a three-necked round bottom flask under nitrogen atmosphere. After vacuum was applied for 30 min, the flask was cooled to room temperature and ammonium fluoride (1,482 mg, 4.0 mmol) and sodium hydroxide (1,000 mg, 2.5 mmol) were added. The mixture was heated to 120 °C for 30 min followed by heating to 240 °C under reflux for 30 min. The flask was cooled to room temperature and the cubic particles were purified as described for the core particles.

For the preparation of $NaYbF_4$(20%Er)@$NaYF_4$ core-shell nanoparticles, 2 mmol of the core particles (542 mg in 15 mL cyclohexane) were mixed with oleic acid (10 mL) and 1-octadecene (10 mL) in a three-necked round bottom flask. The flask was heated to 100 °C under a nitrogen atmosphere and vacuum was applied for 30 min.

Simultaneously, the same procedure was conducted for 2 mmol of the cubic shell precursor. The flask containing core particles was heated to 325 °C under reflux (heating rate 16 °C min^{-1}). During heating (at approx. 200 °C), a small amount of shell precursor (1 mL) was injected *via* a syringe. After reaching the final temperature of 325 °C, small injections of shell precursor were added to the core particles every 10 min. After the last injection, the heating proceeded for another 10 min before cooling to room temperature. Purification of the particles was performed as described for the core particles. The purified particles were stored in cyclohexane (25 mL).

4.5.2.3 Synthesis of UCNPs Functionalized with Oleate Bilayer

To modify 5 mg of the NaYbF$_4$(20%Er)@NaYF$_4$ particles, dodecylamine (6.1 mg, 0.033 mmol) was dissolved in DMSO (400 µL). H$_2$O (1 mL) was added, followed by addition of a saturated Na-oleate solution (1 mL, 100 mg mL^{-1}). The mixture was stirred at about 60 °C until a clear solution was obtained. UCNPs dissolved in cyclohexane (161 µL, 31 mg mL^{-1}) were added slowly, causing the mixture to become turbid again. After further stirring for 1 h at 60 °C, the particle dispersion turned clear, indicating a successful sheathing of the particles.

The particles were purified with three washing cycles *via* centrifugation (21,000 g, 1 h) followed by redispersion in H$_2$O. In a final step, aggregates were removed by centrifugation (3,000 g, 5 min). Particles were stored with a concentration of 2 mg mL^{-1} in H$_2$O.

For UCNPs@bilayer containing no dodecylamine, the same synthetic protocol was performed but adding pure DMSO instead of dodecylamine dissolved in DMSO. For the experiment using oleylamine and octylamine, 0.033 mmol of these compounds were pre-dissolved in DMSO (400 µL) as performed for dodecylamine.

4.5.2.4 Synthesis of Rose Bengal-functionalized UCNPs

UCNPs (5 mg) with oleate-bilayer (10% dodecylamine) were prepared as described above and purified by one centrifugation step (21,000 g, 1 h) followed by redispersion in H$_2$O (1.5 mL).

To enable the coupling reaction of Rose Bengal (RB) to the amine groups in the bilayer, RB was activated as follows. RB (5 mg, 4.9 µmol), EDC (7.6 mg, 49 mmol) and NHS (11.3 mg, 98 mmol) were stirred in MES-buffer (0.5 mL, 50 mM, pH 5.5) for 1 h.

The activated RB, which has low solubility in H_2O, was collected *via* centrifugation (10,000 g, 5 min) and redispersed in H_2O (0.5 mL).

UCNPs@bilayer (1.5 mL) were stirred together with activated RB (0.5 mL) overnight (RT). The particles were purified by centrifugation (21,000 g, 1 h) until the supernatant was colorless. The particles were redispersed in H_2O (2 mL). Aggregates were removed by centrifugation (3,000 g, 5 min). Particles were stored with a concentration of about 2 mg mL^{-1}.

4.5.2.5 Synthesis of UCNPs@BF$_4$

For comparison, UCNPs stabilized by BF_4^- ions were prepared. The UCNPs (30 mg in 1 mL cyclohexane) were mixed with DMF (1 mL) and heated to about 30 °C. NOBF$_4$ (80 mg) was added, and the particles were stirred for 30 min. Afterwards, they were precipitated with an excess of chloroform and collected *via* centrifugation (1,000 g, 5 min). After an additional washing step, the particles in DMF were precipitated by centrifugation (21,000 g, 30 min) and redispersed in H_2O.

4.5.2.6 Synthesis of NO-probe Derivative Ligand

The NO-probe derivative compound was synthesized following a previously reported protocol.[36] ^{1}H NMR (400 MHz, DMSO-d_6) δ = 8.50 – 8.43 (m, 2H; a-H and c-H), 8.38 (d, J = 8.2 Hz, 1H; d/e-H), 7.82 (dd, J = 8.5, 7.3 Hz, 1H; b-H), 7.33 (d, J = 8.2 Hz, 1H; d/e-H), 6.56 (d, J = 8.1 Hz, 1H; g-H), 6.38 (d, J = 2.3 Hz, 1H; h-H), 6.27 (dd, J = 8.1, 2.3 Hz, 1H; f-H), 4.62 – 4.47 (m, 4H; i-H and n-H), 3.19 – 3.13 (m, 4H; j,j'/k,k'-H), 3.04 – 2.99 (m, 4H; j,j'/k,k'-H). m-H could not be seen in the ^{1}H NMR spectrum. ^{13}C NMR (101 MHz, DMSO-d_6) δ = 164.01 (C), 163.51 (C), 156.03 (C), 135.14 (C), 134.83 (C), 132.17 (CH), 130.61 (CH), 129.49 (CH), 128.71 (C), 126.48 (CH), 125.97 (CH), 125.47 (C), 125.31 (C), 123.23 (C), 117.25 (CH), 116.11 (CH), 114.69 (CH), 113.94 (C), 53.65 (CH_2), 45.41 (CH_2). HRMS (ESI+) calc. for $C_{22}H_{21}N_5O_2$ $[M+H]^+$: 388.1695; found: 388.1663.
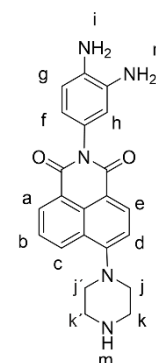
4.5.2.7 Synthesis of NO-probe-functionalized UCNPs

Oleic acid NHS ester was formed by stirring sodium oleate (10 mg, 0.033 mmol) with EDC (50 mg, 0.33 mmol) and NHS (75 mg, 0.66 mmol) in H_2O (0.75 mL) for 1 h at RT. The water was evaporated, and the reaction product dissolved in DMSO (1 mL).

Activated oleate (100 μL), DMSO (300 μL), H_2O (1 mL) and Na-oleate solution (1 mL, 100 mg mL^{-1}) were stirred at 60 °C until a clear solution was obtained. UCNPs (161 μL,

31 mg mL^{-1}) were added slowly. After 20 min reaction time, NO-probe (1.3 mg, 0.0033 mmol, dissolved in 100 µL DMSO) was added to the reaction mixture. The solution was stirred over-night at room temperature. The particles were purified by centrifugation (21,000 g, 1 h) until the supernatant was colorless and afterwards redispersed in H$_2$O (2 mL). Aggregates were removed by centrifugation (3,000 g, 5 min). Particles were stored with a concentration of about 2 mg mL^{-1}.

4.5.2.8 Synthesis of Citrate-coated Gold Nanoparticles (AuNPs@citrate)

A citrate solution (1 mL, 30 mg mL^{-1}) was added to H$_2$O (98.9 mL). The solution was heated to 95 °C and subsequently, an aqueous gold(III) chloride trihydrate solution (100 µL, 98.5 mg mL^{-1}) was added. After 7 minutes of stirring at this temperature, the now strongly red-colored dispersion was cooled to room temperature in an ice bath.

4.5.2.9 Coupling of AuNPs@citrate to UCNPs@bilayer

To remove excess citrate, 3 mL of the AuNPs@citrate dispersion were centrifuged (15,000 g, 20 min) and the resulting pellet was redispersed in H$_2$O (1.5 mL). UCNPs@bilayer were synthesized as described above with 60x48 nm sized UCNPs and purified by one centrifugation step, as for the coupling of Rose Bengal. EDC and NHS (each 1 mg) were dissolved in H$_2$O (10 mL). One milliliter of this solution was added to the AuNPs and the dispersion was stirred at RT (1.5 h) before the UCNPs@bilayer (400 µL, 2.5 mg mL^{-1}) were added. After overnight reaction, the particles were purified by three centrifugation steps (10,000 g, 20 min) followed by redispersion in H$_2$O (1 ml). This procedure was once performed for UCNPs@bilayer containing dodecylamine, and once for UCNPs@bilayer without amine as control.

4.5.2.10 Evaluation of the Singlet Oxygen Production by UCNPs@bilayer-RB

The generation of singlet oxygen was monitored with anthracene-9,10-dipropionic acid (ADPA), a molecular probe for singlet oxygen. The UCNPs@bilayer-RB were mixed with ADPA, which was dissolved in methanol, resulting in final concentrations of 0.3 mg mL^{-1} for the UCNPs and 1 µM for the ADPA. The solution was placed in a stoppered quartz cuvette and the sample was irradiated with a 980 nm NIR laser (200 mW, Picotronic) for 120 min. The fluorescence emission intensity of ADPA was monitored over time between 400 nm – 550 nm (λ_{exc} = 390 nm). A control sample was prepared in H$_2$O with ADPA (1 µM) and it was irradiated at 980 nm for the same time and the fluorescence emission spectra were recorded at 390 nm excitation. A second control, containing free RB (0.0712 µM in H$_2$O) was spiked with ADPA (1 µM),

and measured in the same way. The chosen concentration of RB corresponds to the estimated concentration of RB for UCNPs@bilayer-RB (0.3 mg mL^{-1}). For all measurements, the fluorescence emission intensity at 404 nm was normalized to the time 0 min and was plotted against time.

4.5.2.11 Nitric Oxide Detection using UCNPs@bilayer-NO-probe

For the detection of NO in a cuvette, the fluorescence emission spectrum (λ_{exc} = 405 nm) of UCNPs@bilayer-NO-probe was measured before and 24 h after the addition of diethylamine NONOate. For this, an aqueous solution of UCNPs@bilayer-NO-probe (100 µg mL^{-1}) was treated with NONOate (1.5 mM in NaOH 0.01 M) or with the same amount of NaOH 0.01 M for the control. Diethylamine NONOate sodium salt is a commercially available NO donor that decomposes spontaneously in solution at physiological pH and temperature to generate NO. NONOate stock solution (15 mM) was prepared by dissolving the diethylamine NONOate sodium salt (50 mg) in NaOH 0.01 M (21.49 mL). The solution was kept in the freezer and defrosted 30 min before use.

The fluorescence emission spectra obtained in this experiment were normalised for better comparison. For this, the fluorescence emission spectrum of the UCNPs@bilayer-NO-probe recorded after addition of NONOate was normalized (rescaled) to 100 at the maximum wavelength; and, using the same ratio, the fluorescence emission data for the sample of UCNPs@bilayer-NO-probe in the absence of NO was normalised accordingly.

4.5.3 Biological Experiments

Imaging medium: Imaging Medium (IM) was prepared by mixing NaCl (120 mM), KCl (5 mM), $CaCl_2 \cdot 2H_2O$ (2 mM), $MgCl_2 \cdot 6H_2O$ (1 mM), NaH_2PO_4 (1 mM), $NaHCO_3$ (1 mM), 4-(2-hydroxyethyl)piperazine-4-ethanesulfonic acid (HEPES, 25 mM), D-glucose (11 mM) and bovine serum albumin (BSA, 1 mg mL^{-1}) in H_2O and the pH was adjusted to 7.4 using an aqueous solution of NaOH (1 mM).

Defrost and culture RAW264.7γ NO$^-$ macrophages: The macrophage cell line RAW264.7γ NO$^-$ was cultured in a humidified atmosphere of 5% CO_2 at 37 °C in phenol red-free Dulbecco's Modified Eagle's Medium (DMEM) containing 4.5 mg mL^{-1} D-glucose and supplemented with 1% L-glutamine (200 mM), 1% penicillin-streptomycin (P-S) (100 U mL^{-1} and 100 µg mL^{-1}, respectively) and 10% fetal bovine serum (FBS).

A frozen cryotube containing RAW264.7γ NO$^-$ was defrosted in a water bath at 37 °C. The cell suspension (1 mL) was transferred to a centrifuge tube containing 9 mL of supplemented DMEM media and the cells were centrifuged at 1,000 g for 5 min. The freezing medium was discarded, and the cells were resuspended in fresh supplemented DMEM (12 mL). The content was placed into a 75 cm^2 Nunc Easy Flask and the cells were incubated in an Heracell 150i CO_2 incubator at 37 °C in a 5% CO_2 atmosphere. Subcultures were obtained by dislodging the cells from the flask surface using a cell scraper (18 mm blade), centrifuging them at 800 rpm for 5 min and resuspending the cells in supplemented DMEM medium. Dilutions 1:12 were made every 3 days.

Colocalization studies: LysoTracker Red DND-99 was used as a fluorescent marker of acidic organelles to study the location of UCNPs@bilayer-NO-probe in those organelles. Cells cultured on 18 mm coverslips in 6-well plates incubated with UCNPs@bilayer-NO-probe (25 µg mL^{-1}, 3 h) at 37 °C in a 5% CO_2 atmosphere were further incubated with LysoTracker Red DND-99 (5 µM, 5 min) at 37 °C. Following incubation, the cells were imaged using confocal laser scanning microscopy (CLSM). UCNPs@bilayer-NO-probe were excited using a 405 nm diode laser and the fluorescence emission was recorded between 500 and 580 nm. LysoTracker Red DND-99 was excited using a 561 nm diode laser and the fluorescence emission was recorded between 580 and 625 nm. CLSM images of cells were analyzed in triplicates, each image containing an average of three cells. The Pearson's correlation coefficient

(with coefficient 1 meaning perfect colocalization) and the scatterplot were obtained using ImageJ. The Pearson's correlation coefficient calculated for UCNPs@bilayer-NO-probe and LysoTracker Red DND-99 was 0.76 ± 0.07.

NO detection in RAW264.7γ NO⁻ cells by UCNPs@bilayer-NO-probe: For cellular experiments using UCNPs@bilayer-NO-probe, RAW264.7γ NO⁻ cells were cultured on 18 mm coverslips in 6-well plates. Cells grown to confluence in 75 cm^2 Nunc Easy Flask were harvested from the surface using a cell scraper, centrifuged at 800 rpm for 5 min and resuspended in DMEM medium (9 mL). From the cell suspension, 0.5 mL were added to wells containing 2 mL of DMEM medium. The cells were incubated at 37 °C in a 5% CO_2 atmosphere overnight. After this time, the cells were attached to the coverslips and the medium was replaced with fresh cell culture medium. RAW264.7γ NO⁻ cells were incubated with UCNPs@bilayer-NO-probe (25 µg mL^{-1}) and stimulated following the addition of LPS (0.7 µg mL^{-1}) and IFN-γ (17 µg mL^{-1}). Unstimulated cells were only incubated with UCNPs@bilayer-NO-probe (25 µg mL^{-1}). L-NAME treatment was performed by treating RAW264.7γ NO⁻ cells with L-NAME (2 mM, 1 h) prior to stimulation with LPS (0.7 µg mL^{-1}) and IFN-γ (17 µg mL^{-1}) and incubation with UCNPs@bilayer-NO-probe (25 µg mL^{-1}). Control cells that were not incubated with UCNPs@bilayer-NO-probe were also prepared to contain the same LPS and IFN-γ concentrations used for stimulated cells. Control cells treated with L-NAME (2 mM, 1 h) before stimulation with LPS (0.7 µg mL^{-1}) and IFN-γ (17 µg mL^{-1}) were also prepared. The cells were incubated at 37 °C in a 5% CO_2 atmosphere for 3 h. Following incubation, the cells were imaged using the CLSM (λ_{exc} = 405 nm, $\Delta\lambda_{em}$ = 422 nm – 689 nm).

For the exogenous detection of NO by UCNPs@bilayer-NO-probe, RAW264.7γ NO⁻ cells were cultured overnight on 18 mm coverslips (in 6-well plates) at 37 °C in a 5% CO_2 atmosphere. After this time, cells were incubated with UCNPs@bilayer-NO-probe (25 µg mL^{-1}) for 3 h and were treated with SNAP (275 µM) for 1 h. Following incubation, the cells were imaged using CLSM (λ_{exc} = 405 nm, $\Delta\lambda_{em}$ = 422 nm – 689 nm).

Imaging live cells using a confocal laser scanning microscope: To image live cells in CLSM, the coverslips containing the cells were securely tightened into a Ludin chamber (*Life Imaging Services*) for 18 mm coverslips. The cells were washed three times with IM and 1 mL of IM was added to conduct the imaging on live cells. The Ludin chamber was mounted on a heated stage of the microscope (37 °C). A Carl Zeiss Objective 63x with oil immersion (1.4 NA) was used for imaging. In the CLSM,

Differential interference contrast (DIC) images were collected simultaneously with fluorescence images using the same laser. For spectral analysis on the CLSM, the samples were excited at 405 nm and the fluorescence emission spectra were recorded between 430 nm and 690 nm.

CellTiter-Blue cell viability assays: CellTiter-Blue cell viability assay was conducted to evaluate the cytotoxicity of UCNPs@bilayer-NO-probe in RAW264.7γ NO$^-$ macrophages. The cells at a concentration of 20×10^4 cells mL^{-1} (100 μL per well) were seeded overnight on 96-well black-bottom microplates before treating the cells at 37 °C in a 5% CO_2 atmosphere. Next, the cells were incubated overnight with UCNPs@bilayer-NO-probe at concentrations ranging from 0 to 37.5 μg mL^{-1}. Cells without UCNPs@bilayer-NO-probe were used as control. At this point, after removing the medium and washing once with PBS (100 μL), CellTiter-Blue reagent (20 μL per well) was added, and the cells were incubated for 4 h at 37 °C in a 5% CO_2 atmosphere. The fluorescence emission of the CellTiter-Blue reagent was then measured at 594 nm following excitation at 561 nm using a CLARIOstar (*BMG Labtech*) microplate reader. Background fluorescence was corrected by subtracting fluorescence emission from DMEM phenol red-free medium. Cell viability was calculated as a percentage of non-treated. All the samples were analyzed in triplicates. Statistical significance between means was determined using a two-tailed Student's t-test and P values < 0.05 were considered significant.

4.5.4 Instrumental Techniques

Transmission electron microscopy (TEM): Size and shape of the synthesized nanoparticles were determined by TEM using a 120 kV CM12 microscope (*Philips*). For this purpose, the particle dispersions (1 mg mL^{-1}) were dropped onto 400 mesh carbon-coated copper grids (400 mesh, *PLANO*), several micrographs were recorded and at least 1,000 particles were analyzed using the software *ImageJ*. For negative staining of the TEM grids, the grids were first hydrophilized using oxygen plasma (15 sscm O$_2$, 30 s) by PlasmaFlecto 10 (*Plasma Technology*). The particle dispersion (1 mg mL^{-1} in H$_2$O) was dropped onto the grid and blotted out with filter paper twice before a PTA solution (1% w/v) was dropped onto the grid. The excess solution was again removed by filter paper after 90 s.

Dynamic light scattering (DLS): Particle dispersions were measured using a Zetasizer Nano ZS (*Malvern Panalytical*). All samples are measured in an aqueous environment (H$_2$O or cell medium) three times at 20 °C.

Optical emission spectroscopy with inductively coupled plasma excitation (ICP-OES): Concentration of particle dispersions was determined using ICP-OES with the SPECTROBLUE FMX36 instrument (*SPECTRO*). Calibration was performed using a multielement standard containing Y, Gd, Er, Tm, Yb, and Nd ions. The emission bands at 371 nm (Y), 329 nm (Yb), and 337 nm (Er) were chosen for detection. Concentrations were determined by averaging over three measurements.

Luminescence spectra: Spectra were recorded using a custom-built set-up including a Qmini UV/VIS spectrophotometer (*Broadcom*) and a 980 nm laser module (200 mW, cw) in 90° orientation (*Picotronic*). Unless other specified, the spectra were normalized to a mass concentration of 1 mg mL^{-1} (weight of the ligands not included), which corresponds to a particle concentration of about $2.7 \cdot 10^{13}$ particles·mL^{-1} for core-shell particles with a size of 23.3 nm.

Extinction spectra: Spectra were recorded using a Cary 50 Scan UV-Visible Spectrophotometer (*Agilent*) or a Hitachi U-3000 spectrophotometer at room temperature. Quartz cuvettes with a 1 cm path length were used. For calculation of the number of RB molecules per nanoparticle a molar absorption coefficient of RB $\varepsilon_{549nm} = 95,000$ L mol^{-1} cm^{-1} was used and the spectra were corrected from

scattering.[42] The values were derived by dividing the number of dye molecules per mL by the number of nanoparticles per mL.

Fluorescence excitation and emission spectra: Spectra were obtained using an Edinburgh Instrument FS5 fluorescence spectrometer. Quartz cuvettes with a 1 cm path length were used.

Confocal laser scanning microscopy (CLSM): Cellular images were obtained using a Zeiss CLSM 980 with Airyscan 2 (pinhole adjusted to obtain an optical section of 1.5 µm). Details on the objectives used and the experimental conditions applied are given in the relevant experimental sections. Differential interference contrast (DIC) images were collected, together with fluorescence images exciting the samples at the corresponding laser in each case. Fluorescence emission spectra were obtained using the lambda scan mode. Images and spectra were analyzed using the *ImageJ* software.

Microplate reader: The fluorescence emission intensities of the CellTiter Blue were recorded using a CLARIOstar® (*BMG Labtech*) microplate reader.

4.6 Supplementary Figures
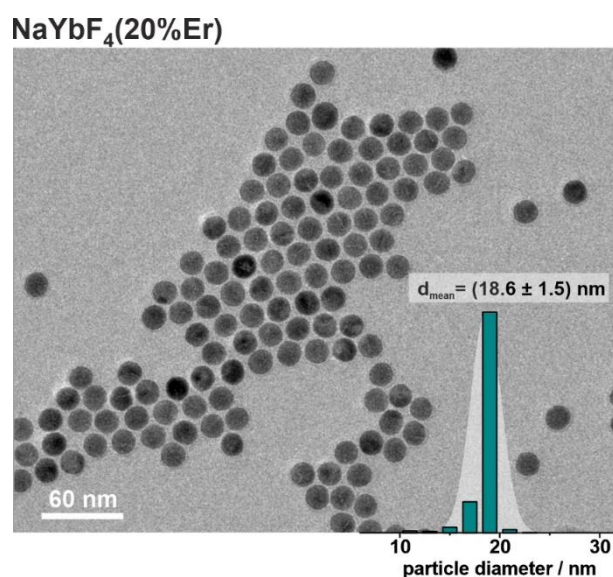

Figure S4.1. TEM micrograph and corresponding histogram of NaYbF$_4$(20%Er) nanoparticles dispersed in cyclohexane. The mean diameter of the nanoparticles is (18.6 ± 1.5) nm and was calculated by averaging over 1,000 nanoparticles.
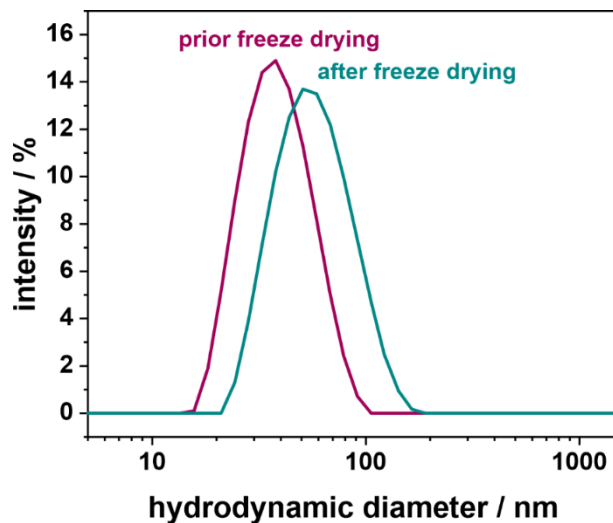
Figure S4.2. DLS measurement of UCNPs@bilayer before and after lyophilization and redispersion in H_2O. The hydrodynamic diameter changed from (36.4 ± 0.6) nm to (51.9 ± 1.8) nm and the PDI from 0.15 ± 0.06 to 0.16 ± 0.02.
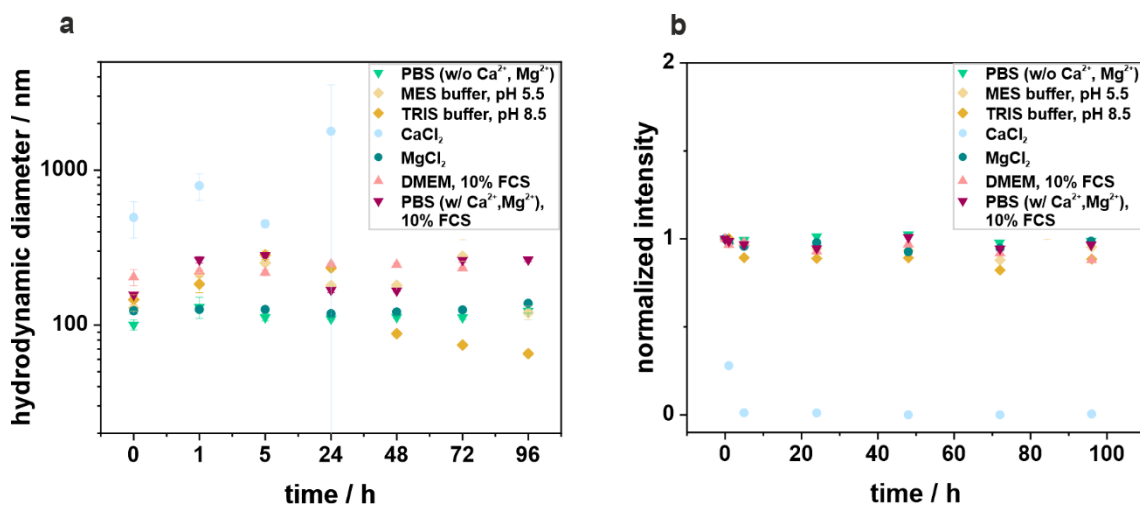
Figure S4.3. (a) Hydrodynamic diameter and (b) normalized integrated luminescence intensity of UCNPs@bilayer with a concentration of 0.2 mg mL^{-1}. The particles were dispersed in the indicated media and DLS and luminescence of the dispersions were recorded at the specified time points. MES and TRIS buffers were in concentrations of 5 mM, $CaCl_2$ of 1.8 mM, $MgCl_2$ of 1 mM in H_2O, according to relevant physiological conditions.[43] Both DMEM and PBS (with Ca^{2+} and Mg^{2+}) contained 10% fetal calf serum (FCS); while PBS (without Ca^{2+} and Mg^{2+}) was used without the addition of FCS. DLS measurements for the sample in $CaCl_2$ were stopped after 24 h since the particles sedimented due to aggregation. PDIs of the samples were between 0.07 and 0.4, exceptions are $CaCl_2$ (PDI > 0.6 nm after 1 h), MES at pH 5.5 (PDI > 0.6 after 24 h) and TRIS at pH 8.5 (PDI > 0.5 after 48 h). For luminescence measurements, the excitation wavelength was 980 nm with an excitation power density of 140 W cm^{-2}. The luminescence spectra were integrated in the range of 400 nm - 800 nm and normalized to the initial emission at 0 h.
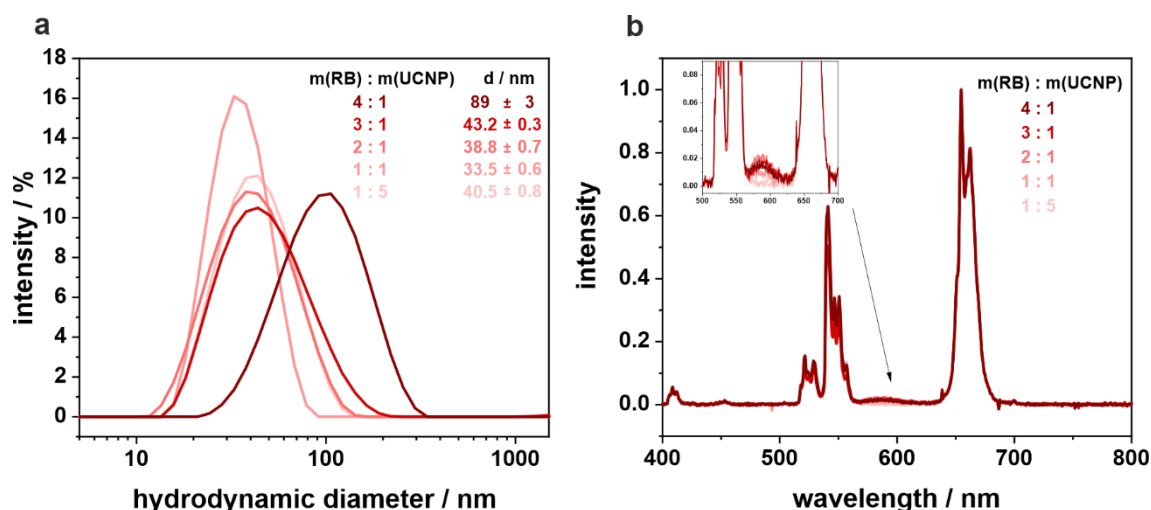
Figure S4.4. (a) DLS measurements of UCNPs@bilayer-RB with different ratios of m(RB) : m(UCNPs). (b) Luminescence spectra of the UCNPs@bilayer-RB under 980 nm excitation in H_2O (140 W cm^{-2}). At 600 nm a weak RB emission is visible in the enlarged section. Spectra were measured at the same concentration of UCNPs (0.2 mg mL^{-1}) and normalized to the red emission. All nanoparticles are dispersed in H_2O.
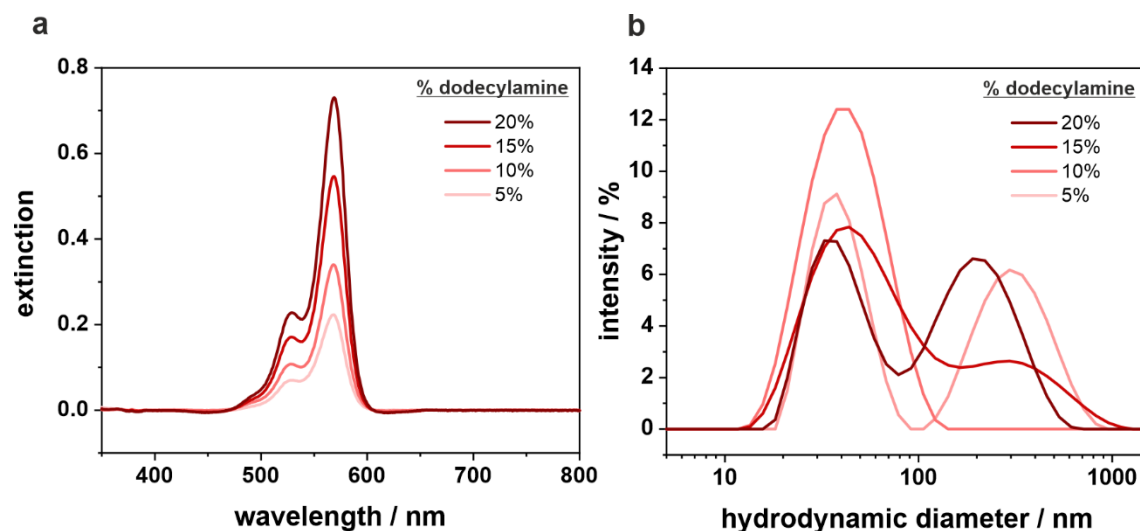
Figure S4.5. (a) Extinction spectra of UCNPs@bilayer-RB in H_2O synthesized with different percentages of dodecylamine during the bilayer formation and constant RB concentration. The particle dispersions were of the same concentrations (1.0 mg mL^{-1}). (b) Corresponding DLS measurements of the nanoparticles.

Figure S4.6. (a) DLS measurement of UCNPs@bilayer-NO-probe in H_2O (d_{hydro} = (36 ± 2) nm, PDI = 0.231 ± 0.004). (b,c,d) Spectral characterization of UCNPs@bilayer-NO-probe (yellow) and unfunctionalized UCNPs@bilayer (1.0 mg mL^{-1}) in H_2O (cyan): (b) extinction spectra, (c) fluorescence excitation spectra (λ_{em} = 520 nm) and (d) fluorescence emission spectra (λ_{exc} = 405 nm). The particles characterized here were used for stability experiments (Figure S4.9) as well as NO detection and cell internalization in Figure 4.5, S4.10 and S4.11
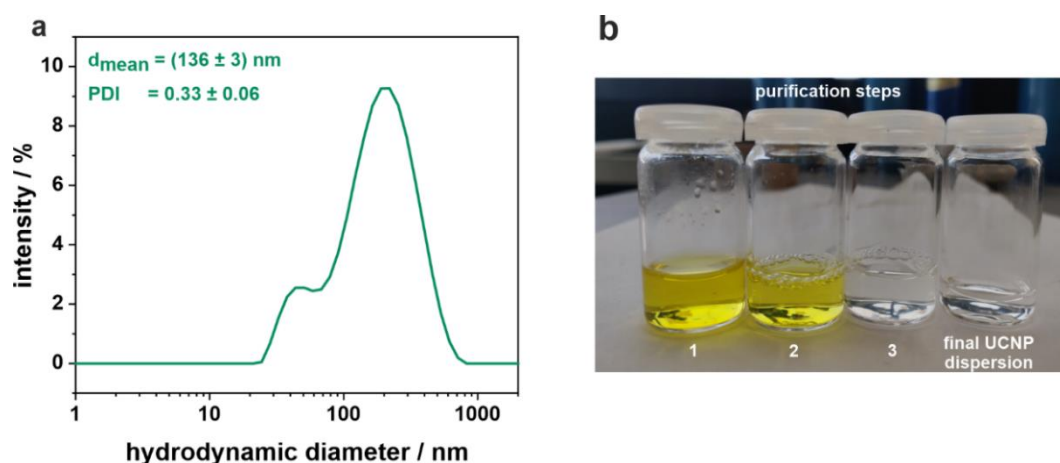
Figure S4.7. Control experiment for the NO-probe functionalization of UCNPs@bilayer without pre-activation of the oleate to see if the amine-derivative NO-probe binds to the oleate or freely intercalates in the bilayer. (a) DLS of the final UCNP dispersion and (b) photographic image of the purification steps. The solutions shown are the supernatants of the centrifugation steps (1-3) and the final purified UCNP dispersion. Since the yellow-colored amine-derivative NO-probe is washed away, no intercalation in the bilayer had happened.
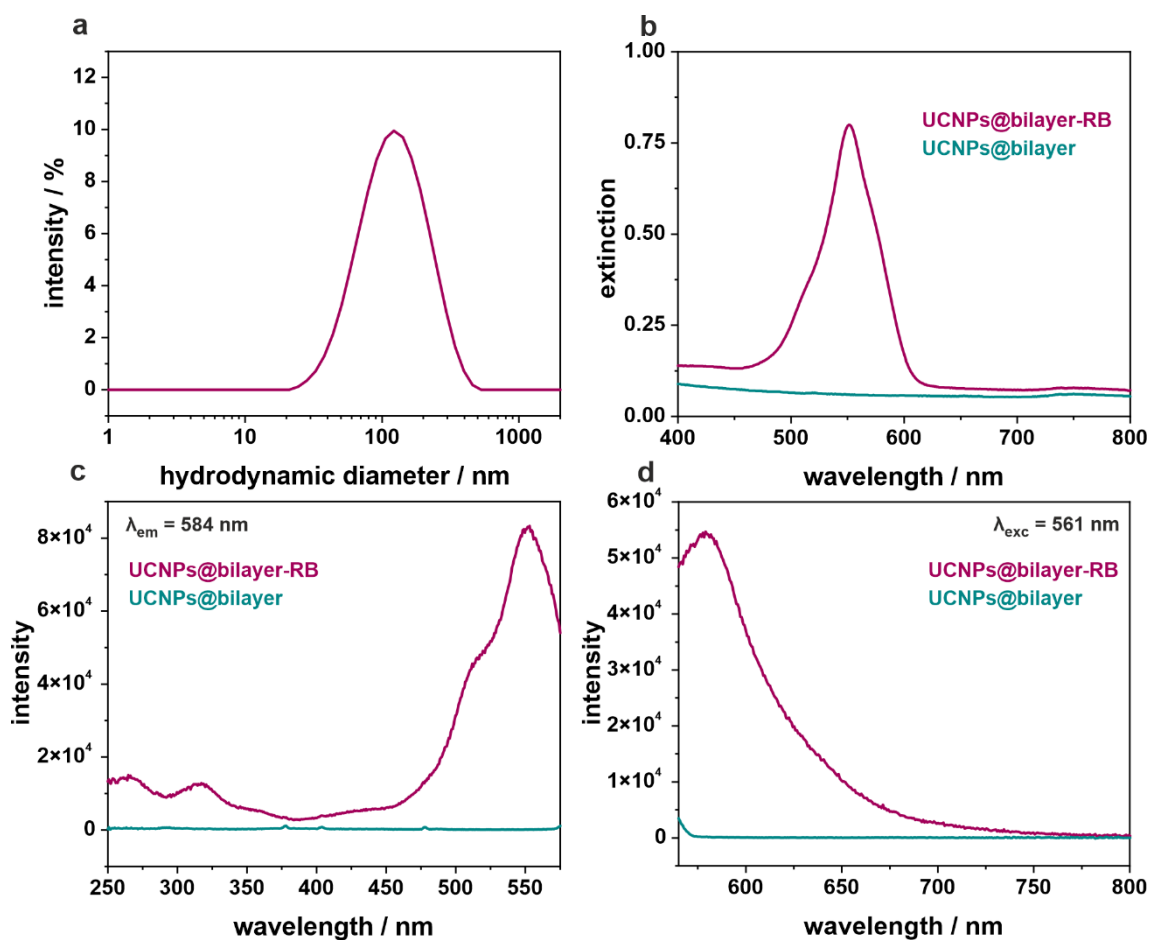
Figure S4.8. (a) DLS measurement of UCNPs@bilayer-RB in H_2O (d_{hydro} = (110 ± 3) nm, PDI = 0.256 ± 0.003). (b,c,d) Spectral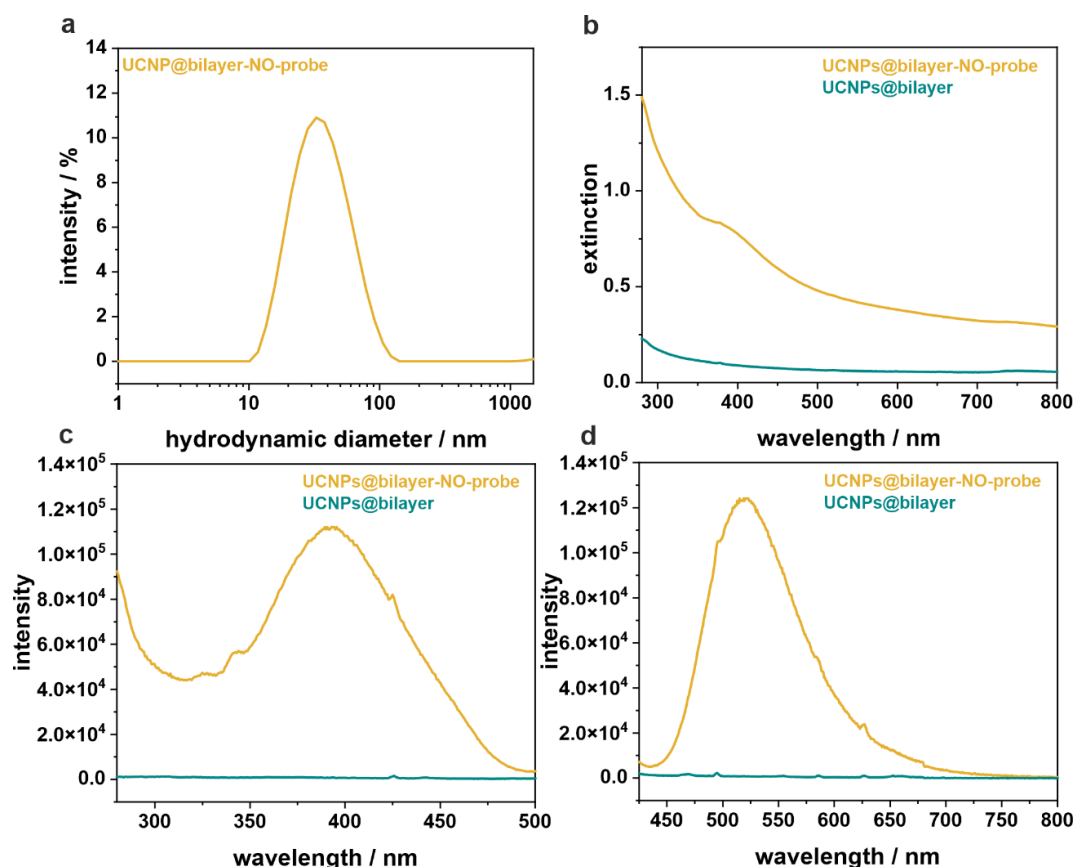 characterization of UCNPs@bilayer-RB (78 µg mL^{-1}, magenta) and unfunctionalized UCNPs@bilayer (1.0 mg mL^{-1}, cyan) in H_2O: (b) extinction spectrum, (c) fluorescence excitation spectrum (λ_{em} = 584 nm) and (d) fluorescence emission spectrum (λ_{exc} = 561 nm). The particles characterized here were used for stability experiments (Figure S4.9) and singlet oxygen determination (Figure 4.5).
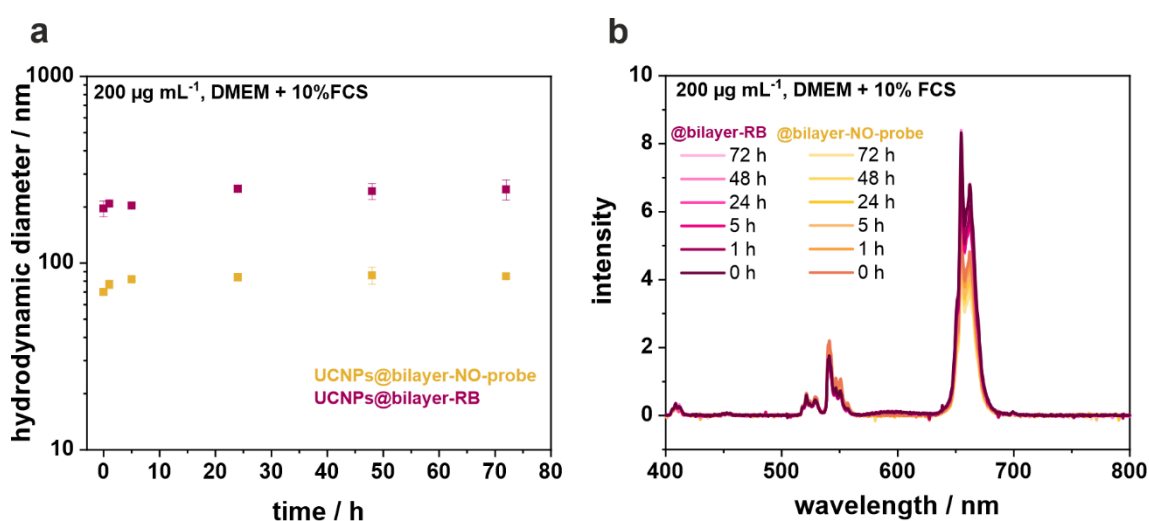
Figure S4.9. (a) Hydrodynamic diameter, derived out of three DLS measurements, recorded over time for UCNPs@bilayer-RB and UCNPs@bilayer-NO-probe in DMEM + 10% FCS cell medium. Error bars indicate the standard deviations derived out of three measurements. (b) Luminescence spectra of the same particles for different times in DMEM + 10% FCS. Spectra are recorded at 980 nm excitation (140 W cm^{-2}).
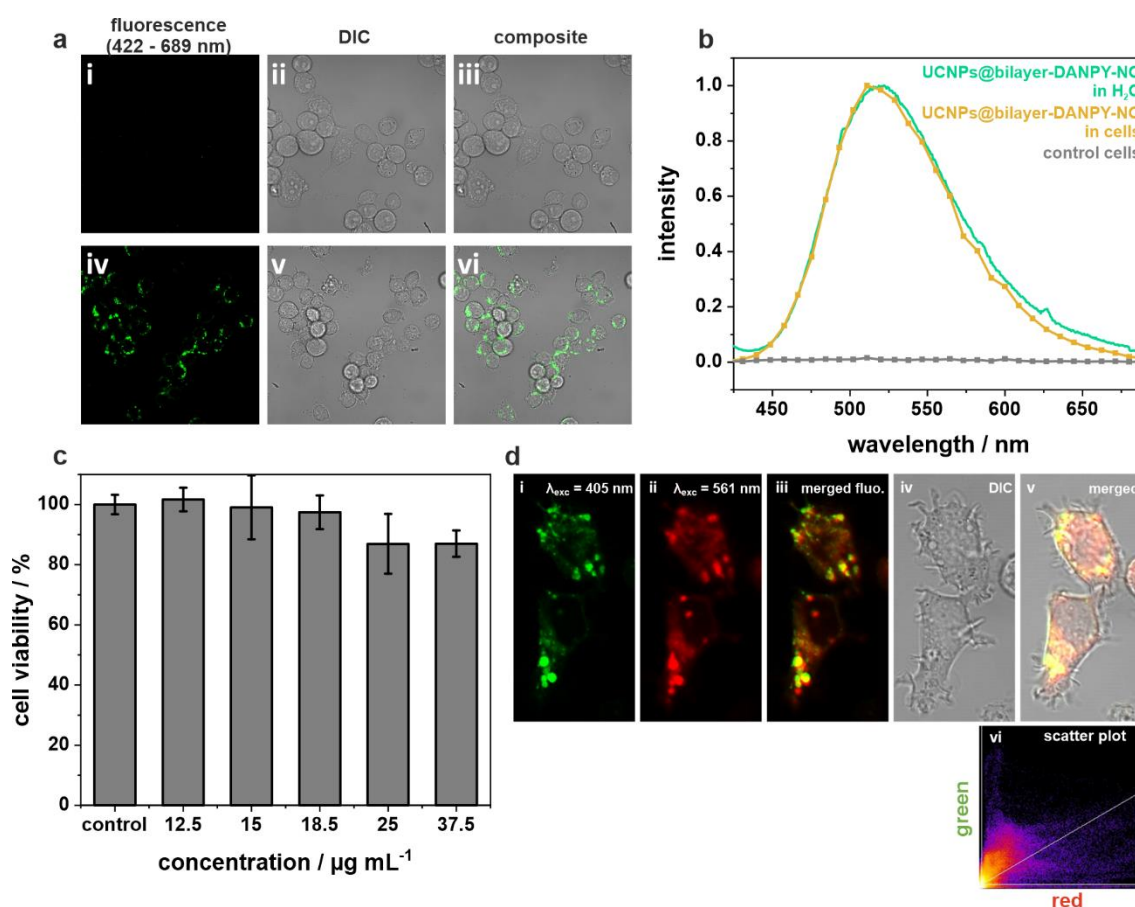
Figure S4.10. (a) CLSM images of RAW264.7γ NO⁻ cells untreated (i – iii) and incubated with UCNPs@bilayer-NO-probe (25 µg mL⁻¹, 3 h) (iv – vi); λ_{exc} = 405 nm, $\Delta\lambda_{em}$ = 422 nm – 689 nm. (b) Normalized fluorescence emission spectrum of: UCNPs@bilayer-NO-probe in H_2O recorded in the fluorimeter (green) and UCNPs@bilayer-NO-probe internalized by RAW264.7γ NO⁻ cells recorded in the CLSM (yellow), and fluorescence emission spectrum of untreated cells (grey). (c) Cell viability studies of UCNPs@bilayer-NO-probe in RAW264.7γ NO⁻ cells. CellTiter Blue viability assay was used to determine the cytotoxicity of UCNPs@bilayer-NO-probe. n = 3, error bars indicate the standard deviation of the three measurements. (d) CLSM images of RAW264.7γ NO⁻ cells incubated with UCNPs@bilayer-NO-probe (25 µg mL⁻¹, 3 h) and LysoTracker™ Red DND-99 (5 µM, 5 min) (i – v) and scatterplot showing the correlation between the green and red emission intensities (vi). Images collected upon excitation at (i) λ_{exc} = 405 nm, $\Delta\lambda_{em}$ = 500 nm – 580 nm and (ii) λ_{exc} = 561 nm, $\Delta\lambda_{em}$ = 580 – 625 nm; (iii) merged fluorescence green and red channel; (iv) DIC channel; and (v) composite image of green, red and DIC channels.
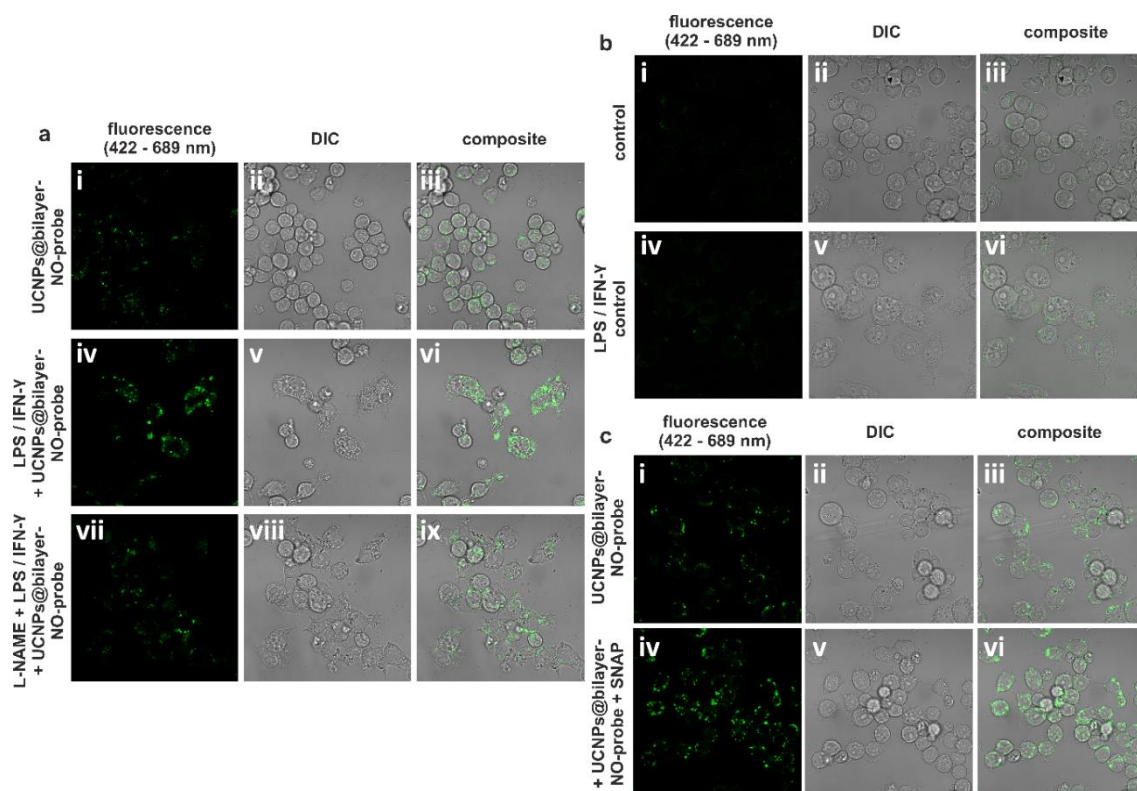
Figure S4.11. (a) CLSM images of RAW264.7γ NO⁻ cells incubated with UCNPs@bilayer-NO-probe (25 µg mL⁻¹, 3 h) unstimulated (i – iii), stimulated (iv – vi) and pre-incubated with L-NAME and stimulated (vii – ix). Stimulation was performed using LPS (0.7 µg mL⁻¹) and IFN-γ (17 µg mL⁻¹) for 3 h and the pre-treatment with L-NAME (2 mM) was done for 30 min prior to the stimulation. λ_{exc} = 405 nm and $\Delta\lambda_{em}$ = 422 nm – 689 nm. (b) CLSM images of unstimulated (i – iii) and stimulated (iv – vi) control RAW264.7γ NO⁻ macrophages. Stimulation and recording of the CLSM images were identical to the conditions in (a). (c) CLSM images of RAW264.7γ NO⁻ cells incubated with UCNPs@bilayer-NO-probe (25 µg mL⁻¹, 3 h) (i – iii) and treated with SNAP (275 µM, 1 h) (iv – vi). λ_{exc} = 405 nm and $\Delta\lambda_{em}$ = 422 nm – 689 nm.
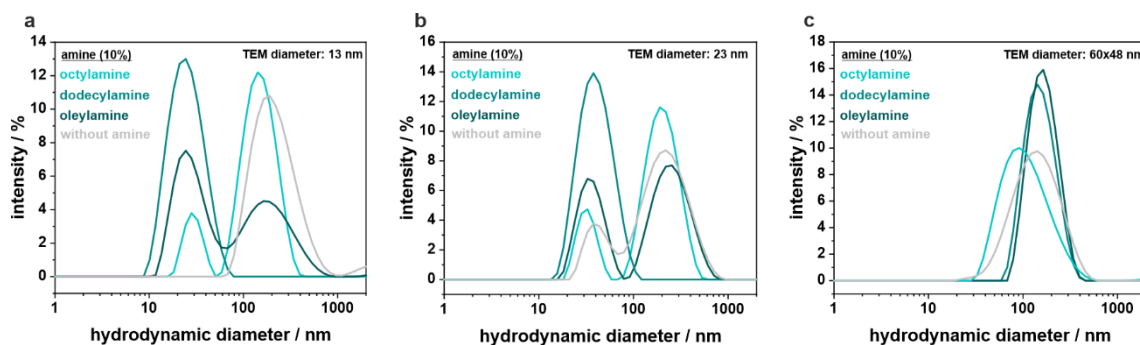
Figure S4.12. DLS measurements of UCNPs@bilayer with variation of the amine (all 10 mol %) used during bilayer preparation (octylamine, dodecylamine, oleylamine and without amine). The hydrodynamic diameter histograms are shown for (a) 13 nm, (b) 23 nm and (c) 60x48 nm core-shell UCNPs (NaYbF$_4$(20%Er)@NaYF$_4$).

Table S4.1. Hydrodynamic diameters and PDIs of UCNPs@bilayer with variation of the amine used during bilayer preparation (octylamine, dodecylamine, oleylamine and without amine). The values are averaged over three measurements.

	13 nm		23 nm		60x48 nm	
	d_{hydro} / nm	PDI	d_{hydro} / nm	PDI	d_{hydro} / nm	PDI
without amine	196 ± 3	0.235 ± 0.004	122.4 ± 0.5	0.448 ± 0.012	134 ± 4	0.29 ± 0.02
octylamine (10%)	99.6 ± 1.5	0.363 ± 0.04	106.6 ± 1.4	0.486 ± 0.009	91 ± 5	0.25 ± 0.02
dodecylamine (10%)	22.3 ± 1.5	0.20 ± 0.01	36.4 ± 0.6	0.147 ± 0.006	155 ± 7	0.182 ± 0.02
oleylamine (10%)	49 ± 2	0.54 ± 0.08	78.9 ± 3.9	0.61 ± 0.075	165 ± 7	0.181 ± 0.03
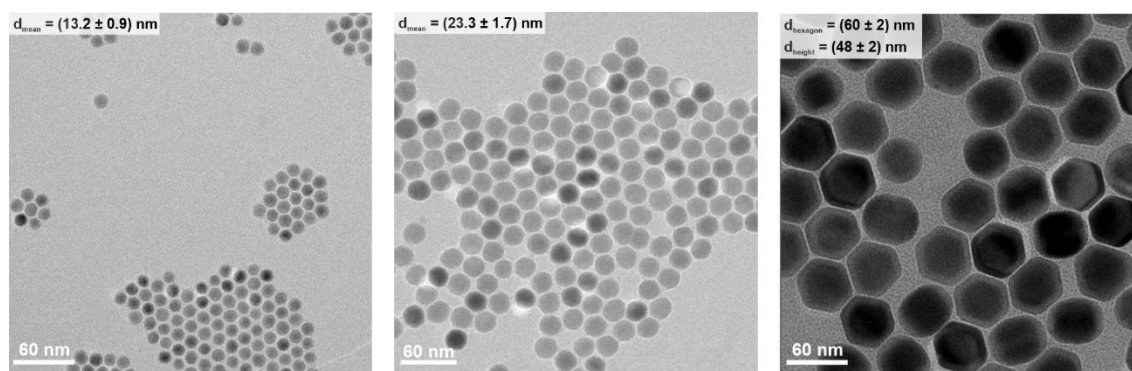
Figure S4.13. TEM micrographs of NaYbF$_4$(20%Er)@NaYF$_4$ with different diameters.

88

4.7 References

[1] Lee, Y.-E. K.; Smith, R.; Kopelman, R. Nanoparticle PEBBLE Sensors in Live Cells and in Vivo. *Annu. Rev. Anal. Chem.* **2009**, *2* (1), 57–76. DOI: 10.1146/annurev.anchem.1.031207.112823.

[2] Lehner, R.; Wang, X.; Marsch, S.; Hunziker, P. Intelligent Nanomaterials for Medicine: Carrier Platforms and Targeting Strategies in the Context of Clinical Application. *Nanomedicine* **2013**, *9* (6), 742–757. DOI: 10.1016/j.nano.2013.01.012.

[3] Liu, P.; Qin, R.; Fu, G.; Zheng, N. Surface Coordination Chemistry of Metal Nanomaterials. *J. Am. Chem. Soc.* **2017**, *139* (6), 2122–2131. DOI: 10.1021/jacs.6b10978.

[4] Pfeiffer, C.; Rehbock, C.; Hühn, D.; Carrillo-Carrion, C.; Aberasturi, D. J. de; Merk, V.; Barcikowski, S.; Parak, W. J. Interaction of Colloidal Nanoparticles with their Local Environment: The (ionic) Nanoenvironment Around Nanoparticles is Different from Bulk and Determines the Physico-chemical Properties of the Nanoparticles. *J. R. Soc., Interface* **2014**, *11* (96), 20130931. DOI: 10.1098/rsif.2013.0931.

[5] Li, Y.; Chen, C.; Liu, F.; Liu, J. Engineered Lanthanide-doped Upconversion Nanoparticles for Biosensing and Bioimaging Application. *Microchim. Acta* **2022**, *189* (3), 109. DOI: 10.1007/s00604-022-05180-1.

[6] Haase, M.; Schäfer, H. Upconverting Nanoparticles. *Angew. Chem., Int. Ed.* **2011**, *50* (26), 5808–5829. DOI: 10.1002/anie.201005159.

[7] Xie, X.; Gao, N.; Deng, R.; Sun, Q.; Xu, Q.-H.; Liu, X. Mechanistic Investigation of Photon Upconversion in Nd^{3+}-sensitized Core-Shell Nanoparticles. *J. Am. Chem. Soc.* **2013**, *135* (34), 12608–12611. DOI: 10.1021/ja4075002.

[8] Chen, G.; Qiu, H.; Prasad, P. N.; Chen, X. Upconversion Nanoparticles: Design, Nanochemistry, and Applications in Theranostics. *Chem. Rev.* **2014**, *114* (10), 5161–5214. DOI: 10.1021/cr400425h.

[9] Zhang, Z.; Shikha, S.; Liu, J.; Zhang, J.; Mei, Q.; Zhang, Y. Upconversion Nanoprobes: Recent Advances in Sensing Applications. *Anal. Chem.* **2019**, *91* (1), 548–568. DOI: 10.1021/acs.analchem.8b04049.

[10] Mai, H.-X.; Zhang, Y.-W.; Si, R.; Yan, Z.-G.; Sun, L.; You, L.-P.; Yan, C.-H. High-quality Sodium Rare-Earth Fluoride Nanocrystals: Controlled Synthesis and Optical Properties. *J. Am. Chem. Soc.* **2006**, *128* (19), 6426–6436. DOI: 10.1021/ja060212h.

[11] Muhr, V.; Würth, C.; Kraft, M.; Buchner, M.; Baeumner, A. J.; Resch-Genger, U.; Hirsch, T. Particle-Size-Dependent Förster Resonance Energy Transfer from Upconversion Nanoparticles to Organic Dyes. *Anal. Chem.* **2017**, *89* (9), 4868–4874. DOI: 10.1021/acs.analchem.6b04662.

[12] Wilhelm, S.; Kaiser, M.; Würth, C.; Heiland, J.; Carrillo-Carrion, C.; Muhr, V.; Wolfbeis, O. S.; Parak, W. J.; Resch-Genger, U.; Hirsch, T. Water Dispersible Upconverting Nanoparticles: Effects of Surface Modification on their Luminescence and Colloidal Stability. *Nanoscale* **2015**, *7* (4), 1403–1410. DOI: 10.1039/c4nr05954a.

[13] Guerrini, L.; Alvarez-Puebla, R. A.; Pazos-Perez, N. Surface Modifications of Nanoparticles for Stability in Biological Fluids. *Materials* **2018**, *11* (7), 1154. DOI: 10.3390/ma11071154.

[14] Rosen, E. L.; Buonsanti, R.; Llordes, A.; Sawvel, A. M.; Milliron, D. J.; Helms, B. A. Exceptionally Mild Reactive Stripping of Native Ligands from Nanocrystal Surfaces by Using Meerwein's salt. *Angew. Chem., Int. Ed.* **2012**, *51* (3), 684–689. DOI: 10.1002/anie.201105996.

[15] Dong, A.; Ye, X.; Chen, J.; Kang, Y.; Gordon, T.; Kikkawa, J. M.; Murray, C. B. A Generalized Ligand-Exchange Strategy Enabling Sequential Surface Functionalization of Colloidal Nanocrystals. *J. Am. Chem. Soc.* **2011**, *133* (4), 998–1006. DOI: 10.1021/ja108948z.

[16] Kong, W.; Sun, T.; Chen, B.; Chen, X.; Ai, F.; Zhu, X.; Li, M.; Zhang, W.; Zhu, G.; Wang, F. A General Strategy for Ligand Exchange on Upconversion Nanoparticles. *Inorg. Chem.* **2017**, *56* (2), 872–877. DOI: 10.1021/acs.inorgchem.6b02479.

[17] Himmelstoß, S. F.; Hirsch, T. Long-Term Colloidal and Chemical Stability in Aqueous Media of NaYF$_4$ -Type Upconversion Nanoparticles Modified by Ligand-Exchange. *Part. Part. Syst. Charact.* **2019**, *57*, 1900235. DOI: 10.1002/ppsc.201900235.

[18] Tong, L.; Lu, E.; Pichaandi, J.; Cao, P.; Nitz, M.; Winnik, M. A. Quantification of Surface Ligands on NaYF$_4$ Nanoparticles by Three Independent Analytical Techniques. *Chem. Mater.* **2015**, *27* (13), 4899–4910. DOI: 10.1021/acs.chemmater.5b02190.

[19] Arppe, R.; Hyppänen, I.; Perälä, N.; Peltomaa, R.; Kaiser, M.; Würth, C.; Christ, S.; Resch-Genger, U.; Schäferling, M.; Soukka, T. Quenching of the Upconversion Luminescence of NaYF$_4$:Yb^{3+},Er^{3+} and NaYF$_4$:Yb^{3+},Tm^{3+} Nanophosphors by Water: The Role of the Sensitizer Yb^{3+} in Non-radiative Relaxation. *Nanoscale* **2015**, *7* (27), 11746–11757. DOI: 10.1039/c5nr02100f.

[20] Dukhno, O.; Przybilla, F.; Muhr, V.; Buchner, M.; Hirsch, T.; Mély, Y. Time-dependent Luminescence Loss for Individual Upconversion Nanoparticles Upon Dilution in Aqueous Solution. *Nanoscale* **2018**, *10* (34), 15904–15910. DOI: 10.1039/C8NR03892A.

[21] Lahtinen, S.; Lyytikäinen, A.; Päkkilä, H.; Hömppi, E.; Perälä, N.; Lastusaari, M.; Soukka, T. Disintegration of Hexagonal NaYF$_4$:Yb^{3+},Er^{3+} Upconverting Nanoparticles in Aqueous Media: The Role of Fluoride in Solubility Equilibrium. *J. Phys. Chem. C* **2017**, *121* (1), 656–665. DOI: 10.1021/acs.jpcc.6b09301.

[22] Pellegrino, T.; Manna, L.; Kudera, S.; Liedl, T.; Koktysh, D.; Rogach, A. L.; Keller, S.; Rädler, J.; Natile, G.; Parak, W. J. Hydrophobic Nanocrystals Coated with an Amphiphilic Polymer Shell: A General Route to Water Soluble Nanocrystals. *Nano Lett.* **2004**, *4* (4), 703–707. DOI: 10.1021/nl035172j.

[23] Černič, T.; Koren, M.; Majaron, B.; Ponikvar-Svet, M.; Lisjak, D. Optimisation of Amphiphilic-Polymer Coatings for Improved Chemical Stability of NaYF$_4$-based Upconverting Nanoparticles. *Acta Chim. Slov.* **2022**, *69* (2), 448–457. DOI: 10.17344/acsi.2021.7336.

[24] Lin, C.-A. J.; Sperling, R. A.; Li, J. K.; Yang, T.-Y.; Li, P.-Y.; Zanella, M.; Chang, W. H.; Parak, W. J. Design of an Amphiphilic Polymer for Nanoparticle Coating and Functionalization. *Small* **2008**, *4* (3), 334–341. DOI: 10.1002/smll.200700654.

[25] Yang, S.; Li, N.; Liu, Z.; Sha, W.; Chen, D.; Xu, Q.; Lu, J. Amphiphilic copolymer coated Upconversion Nanoparticles for Near-infrared Light-triggered Dual Anticancer Treatment. *Nanoscale* **2014**, *6* (24), 14903–14910. DOI: 10.1039/c4nr05305b.

[26] Liras, M.; González-Béjar, M.; Peinado, E.; Francés-Soriano, L.; Pérez-Prieto, J.; Quijada-Garrido, I.; García, O. Thin Amphiphilic Polymer-Capped Upconversion Nanoparticles: Enhanced Emission and Thermoresponsive Properties. *Chem. Mater.* **2014**, *26* (13), 4014–4022. DOI: 10.1021/cm501663n.

[27] Rojas-Gutierrez, P. A.; DeWolf, C.; Capobianco, J. A. Formation of a Supported Lipid Bilayer on Faceted $LiYF_4$:Tm^{3+}/Yb^{3+} Upconversion Nanoparticles. *Part. Part. Syst. Charact.* **2016**, *33* (12), 865–870. DOI: 10.1002/ppsc.201600218.

[28] Meijer, M. S.; Talens, V. S.; Hilbers, M. F.; Kieltyka, R. E.; Brouwer, A. M.; Natile, M. M.; Bonnet, S. NIR-Light-Driven Generation of Reactive Oxygen Species Using Ru(II)-Decorated Lipid-Encapsulated Upconverting Nanoparticles. *Langmuir* **2019**, *35* (37), 12079–12090. DOI: 10.1021/acs.langmuir.9b01318.

[29] Schroter, A.; Märkl, S.; Weitzel, N.; Hirsch, T. Upconversion Nanocrystals with High Lanthanide Content: Luminescence Loss by Energy Migration versus Luminescence Enhancement by Increased NIR Absorption. *Adv. Funct. Mater.* **2022**, *32* (26), 2113065. DOI: 10.1002/adfm.202113065.

[30] Rodriguez-Cruz, S. E.; Jockusch, R. A.; Williams, E. R. Hydration Energies and Structures of Alkaline Earth Metal Ions, $M^{2+}(H_2O)_n$, n = 5-7, M = Mg, Ca, Sr, and Ba. *J. Am. Chem. Soc.* **1999**, *121* (38), 8898–8906. DOI: 10.1021/ja9911871.

[31] Molinari, R.; Avci, A. H.; Argurio, P.; Curcio, E.; Meca, S.; Plà-Castellana, M.; Cortina, J. L. Selective Precipitation of Calcium Ion from Seawater Desalination Reverse Osmosis Brine. *J. Cleaner Prod.* **2021**, *328*, 129645. DOI: 10.1016/j.jclepro.2021.129645.

[32] Garbujo, S.; Galbiati, E.; Salvioni, L.; Mazzucchelli, M.; Frascotti, G.; Sun, X.; Megahed, S.; Feliu, N.; Prosperi, D.; Parak, W. J.; Colombo, M. Functionalization of Colloidal Nanoparticles with a Discrete Number of Ligands Based on a "HALO-bioclick" Reaction. *Chemical Communications* **2020**, *56* (77), 11398–11401. DOI: 10.1039/d0cc04355a.

[33] Montenegro, J.-M.; Grazu, V.; Sukhanova, A.; Agarwal, S.; La Fuente, J. M. de; Nabiev, I.; Greiner, A.; Parak, W. J. Controlled Antibody/(bio-) Conjugation of Inorganic Nanoparticles for Targeted Delivery. *Adv. Drug Delivery Rev.* **2013**, *65* (5), 677–688. DOI: 10.1016/j.addr.2012.12.003.

[34] Sapsford, K. E.; Algar, W. R.; Berti, L.; Gemmill, K. B.; Casey, B. J.; Oh, E.; Stewart, M. H.; Medintz, I. L. Functionalizing Nanoparticles with Biological Molecules: Developing Chemistries that Facilitate Nanotechnology. *Chem. Rev.* **2013**, *113* (3), 1904–2074. DOI: 10.1021/cr300143v.

[35] Arnau del Valle, C.; Williams, L.; Thomas, P.; Johnson, R.; Raveenthiraraj, S.; Warren, D.; Sobolewski, A.; Muñoz, M. P.; Galindo, F.; Marín, M. J. A Highly Photostable and Versatile Two-photon Fluorescent Probe for the Detection of a Wide Range of Intracellular Nitric Oxide Concentrations in Macrophages and Endothelial Cells. *J. Photochem. Photobiol., B* **2022**, *234*, 112512. DOI: 10.1016/j.jphotobiol.2022.112512.

[36] Arnau del Valle, C.; Thomas, P.; Galindo, F.; Muñoz, M. P.; Marín, M. J. Gold Nanoparticle-based Two-photon Fluorescent Nanoprobe for Monitoring Intracellular Nitric Oxide Levels. *J. Mater. Chem. B* **2023**, *11* (15), 3387–3396. DOI: 10.1039/d3tb00103b.

[37] Mai, H.-X.; Zhang, Y.-W.; Sun, L.; Yan, C.-H. Size- and Phase-Controlled Synthesis of Monodisperse $NaYF_4$:Yb,Er Nanocrystals from a Unique Delayed Nucleation Pathway Monitored with Upconversion Spectroscopy. *J. Phys. Chem. C* **2007**, *111* (37), 13730–13739. DOI: 10.1021/jp073919e.

[38] Ye, X.; Collins, J. E.; Kang, Y.; Chen, J.; Chen, D. T. N.; Yodh, A. G.; Murray, C. B. Morphologically Controlled Synthesis of Colloidal Upconversion Nanophosphors and Their Shape-directed Self-Assembly. *Proc. Natl. Acad. Sci. U. S. A.* **2010**, *107* (52), 22430–22435. DOI: 10.1073/pnas.1008958107.

[39] Agudo-Canalejo, J.; Lipowsky, R. Critical Particle Sizes for the Engulfment of Nanoparticles by Membranes and Vesicles with Bilayer Asymmetry. *ACS Nano* **2015**, *9* (4), 3704–3720. DOI: 10.1021/acsnano.5b01285.

[40] Fameau, A.-L.; Zemb, T. Self-assembly of Fatty Acids in the Presence of Amines and Cationic Components. *Adv. Colloid Interface Sci.* **2014**, *207*, 43–64. DOI: 10.1016/j.cis.2013.11.017.

[41] Engberts, J. B.; Kevelam, J. Formation and Stability of Micelles and Vesicles. *Curr. Opin. Colloid Interface Sci.* **1996**, *1* (6), 779–789. DOI: 10.1016/S1359-0294(96)80082-3.

[42] Ludvíková, L.; Friš, P.; Heger, D.; Šebej, P.; Wirz, J.; Klán, P. Photochemistry of Rose Bengal in Water and Acetonitrile: A Comprehensive Kinetic Analysis. *Phys. Chem. Chem. Phys.* **2016**, *18* (24), 16266–16273. DOI: 10.1039/c6cp01710j.

[43] Märkl, S.; Schroter, A.; Hirsch, T. Small and Bright Water-Protected Upconversion Nanoparticles with Long-Time Stability in Complex, Aqueous Media by Phospholipid Membrane Coating. *Nano Lett.* **2020**, *20* (12), 8620–8625. DOI: 10.1021/acs.nanolett.0c03327.

5 Control of Luminescence and Interfacial Properties as Perspective for Upconversion Nanoparticles

5.1 Abstract

Near-infrared (NIR) light is highly suitable for studying biological systems due to its minimal scattering and lack of background fluorescence excitation, resulting in high signal-to-noise ratios. By combining NIR light with lanthanide-based upconversion nanoparticles (UCNPs), upconversion is used to generate UV or visible light within tissue. This remarkable property has gained significant research interest over the past two decades. Synthesis methods have been developed to produce particles of various sizes, shapes, and complex core-shell architectures and new strategies are explored to optimize particle properties for specific bioapplications. The diverse photophysics of lanthanide ions offers extensive possibilities to tailor spectral characteristics by incorporating different ions and manipulating their arrangement within the nanocrystal. However, several challenges remain before UCNPs can be widely applied. Understanding the behavior of particle surfaces when exposed to complex biological environments is crucial. In applications where deep tissue penetration is required, such as photodynamic therapy and optogenetics, UCNPs show great potential as nanolamps. These nanoparticles can combine diagnostics and therapeutics in a minimally invasive, efficient manner, making them ideal upconversion probes. This article provides an overview of recent UCNP design trends, highlights past research achievements, and outlines potential future directions to bring upconversion research to the next level.

Author contributions:

This chapter has been published as perspectives article. Concept and structure of the article were planned by AS and TH. AS did the literature survey and wrote the

manuscript. The manuscript was revised by AS together with TH and TH is the corresponding author.

5.2 Introduction

Many biomedical and bioanalytical questions can be attractively answered using optical methods, as demonstrated by the popularity of fluorescence microscopy or the frequent application of fluorescent assays.[1,2] Along with this also improved luminescent nanoprobes are required and here the latest developments in the field of upconverting nanoparticles (UCNPs) display their great potential. Upconversion nanoparticles based on a crystalline host lattice (in most cases $NaYF_4$) and doped with different combinations of lanthanide ions differ from other nanoscale luminescent probes mainly in that they are NIR-excitable and thus have advantages as a high tissue penetration, low autofluorescence, and high signal-to-noise ratios. The photostability and their property of not blinking also distinguish them for possible applications. The NIR light is converted into visible and UV light by sequential multiphoton absorption of the many long-lived electronic states of lanthanide ions. Compared to two-photon excitation of dyes, this process increases the probability of reaching higher excited states and therefore allows lower excitation intensities.[3]

Despite this simple explanation of the upconversion principle in lanthanide-doped nanoparticles, the detailed mechanism is complex in nature, mainly due to the limitations imposed by Laporte's rule on the occupation of the energy levels and myriad competing nonradiative transitions within the ions.[4] Consequently, compared to other luminescent probes, their brightness is limited. Luckily, the knowledge in nanoparticle synthesis has grown significantly, allowing much more complex particle architectures, and thus leading to smart and creative particle designs that can compensate for the former weak luminescence. By implementing several different lanthanide ions in a host crystal, intentional crosstalk between these ions is induced, leading to processes such as energy migration, cross-relaxation, energy trapping, or excitation and emission wavelength shifts. The clever choice of doping and its spatial arrangement in the nanocrystal thus enables a precise adjustment of the luminescence regarding spectral properties, intensity, and lifetime.[5]

Before UCNPs can be used in biological environments, they must be equipped with a surface coating that keeps the particles colloidally and chemically stable even in the presence of proteins, high salt concentrations, and at different pH values.[6] Exciting progress has also been made in this area, especially concerning an efficient functionalization that has receptor or actuator properties for sensing, light-controlled local generation of reactive species, or controlled drug-release.[7] However, more research is needed, not only to fully control and understand the processes on the

particle surfaces, but also to protect the nanoparticle itself so that its luminescent properties can be used in chemically complex environments and remain stable over time.

In the following, the most important milestones of the last few years of upconversion research are shown, but also existing research gaps are pointed out and supplemented with ideas on how the research could be continued. The focus is on applications of UCNPs where the lanthanide emissions themselves are detected, such as in biosensing or bioimaging, and in applications where the UCNPs are used more as transducers, triggering other mechanisms such as drug release, photodynamic therapy, or optogenetics.

5.3 Strategies in Particle Design

Naturally, the relatively low efficiency of photon upconversion in lanthanide-doped nanoparticles due to the multi-photon processes still provides sufficient motivation for scientists to improve them. Depending on the application, significant successes have been achieved through energy harvesting, using antenna dyes and through coupling with plasmonic structures or photonic crystals.[8–11] However, for bioapplications that require, among other things, long stability and low toxicity, strategies that address particle composition and architecture are often more promising. An improved understanding of the synthesis of small, monodisperse nanoparticles has led to remarkable advances in this field. Probably the greatest implications in novel particle architectures are due to a) the development of nanoparticles with a core-shell structure and b) the realization that the concentrations of sensitizer and activator ions can be higher than it has been assumed for many years.[5,12–23] A combination of both approaches opens a wide field of previously unexplored particle systems, with possibilities to adapt the spectral properties of these particles even better to the requirements for medical-diagnostic applications, either by improving the general efficiency of upconversion or by specifically increasing the probabilities of individual transitions in the complex energy term scheme of UCNPs. The beginning of these new trends is marked, among others, by the development of UCNPs that omit sensitizer ions at all. Tm-doped UCNPs, which are excited by photon avalanche (PA) and therefore benefit from a high concentration of Tm^{3+} within the $NaYF_4$ crystal caused a stir. A high excitation power (in most cases $>10\,kW\,cm^{-2}$) favors the excited-state absorption (ESA) of Tm^{3+}, followed by cross-relaxations (CR) caused by the high Tm^{3+} concentrations in the crystal. The combination of ESA and CR sets the bulk of Tm ions in intermediate excited states, which then leads to extremely high populations of the higher excited

states since ESA now occurs without the further possibility of CR (Figure 5.1a). This upconversion process follows a strongly non-linear behavior, as the emission intensities increase immensely once a certain excitation power threshold is reached. As a result, these particles surpass all other UCNPs reported to date in terms of brightness. Therefore they are of great interest for application in high-resolution microscopy, as the high-power dependence confines the excitation beam to the maximum of the Gaussian laser distribution, enabling to beat the Abbe diffraction limit.[24–26]

However, apart from high-resolution microscopy, the applicability of such particles in biological systems is limited due to the high excitation power densities, even when trying to choose the excitation wavelength in the optically silent regions within the biological window (800 nm, 1,064 nm, or 1,450 nm). When it is desired to work with the lowest possible power densities, core–shell architectures are increasingly showing their advantages, especially in multishell systems, where spatial separation of different types of lanthanide ions is achieved. Recently, Liu *et al.* show that the separation of sensitizers from activators can lead to an increased luminescence intensity compared to particles in which sensitizers and activators are combined.[27] This study compares three different structures based on $NaLuF_4$ host lattices: Yb,Er@inert, Yb@Er@inert and Er@Yb@inert (Figure 5.1b). While the Yb-intermediate shell approach showed about a four-fold UCL enhancement compared to the Yb,Er-core particles, the Er-intermediate-shell particles were less bright than the mixed particles. This clearly shows that not only the separation is important, but also the exact sequence of the lanthanide layers. The separation of Yb^{3+} from Er^{3+} minimizes Er→Yb reverse energy transfer processes, which are known to reduce luminescence intensities. The superiority of Er@Yb@inert particles compared to Yb@Er@inert is mainly attributed to shorter energy migration paths from the outer Yb ions to the Er^{3+} in the core and to the fact that the Er-ions are stronger affected by quenching processes because they are closer to the particle surface.[27] Similar results were obtained by Yao *et al.*, showing that growth of the sensitizer shell around a core particle doped only with activators allows controlled energy migration from the shell to the core and thus upconversion efficiency gets improved.[28]
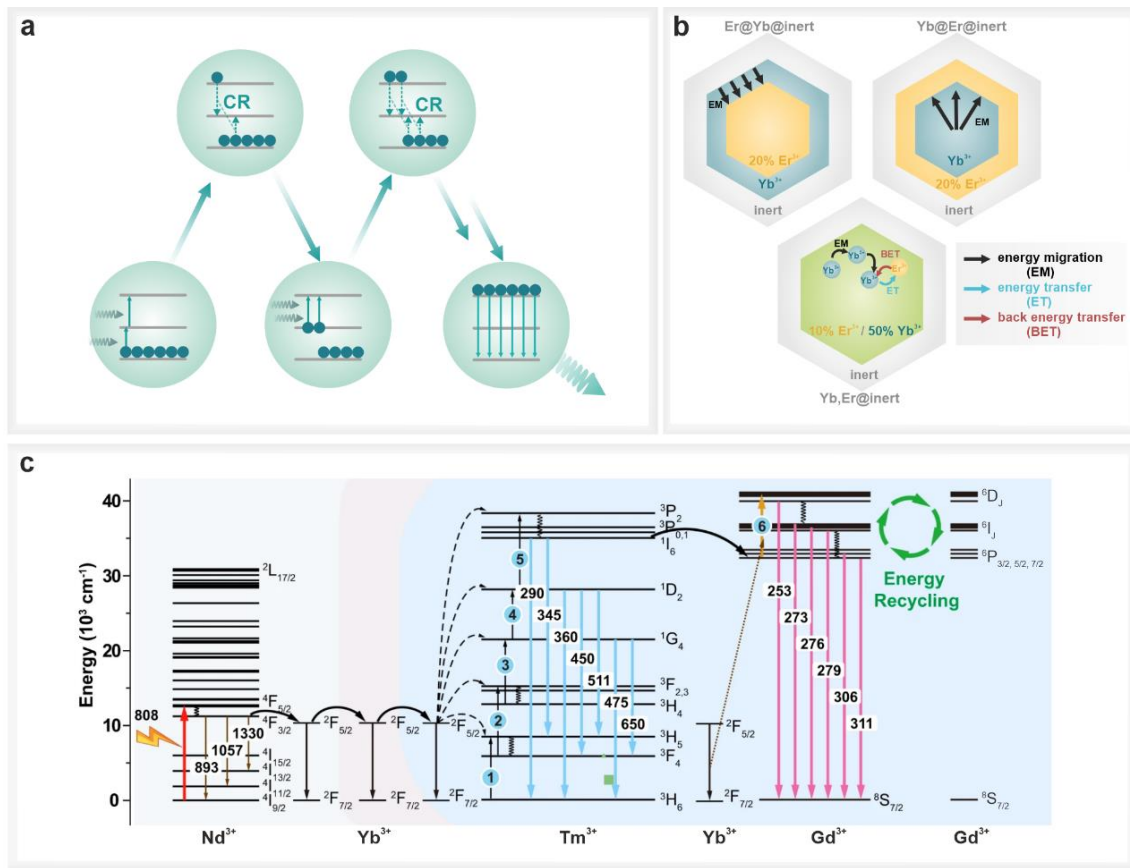
Figure 5.1. (a) Mechanism of cross-relaxation-assisted photon avalanche. (b) Energy migration pathways in core-shell approaches w/ or w/o segregation of sensitizer and activator ions. The graphic is adapted from Ref.[27]. (c) Energy level diagram of a multishell approach using particles of the type Gd,Yb,Tm@Yb@Gd,Yb,Nd@Gd. The graphic is adapted from Ref.[29].

Even omitting the spatial separation of the sensitizing and activating groups can result in bright UCL if directional energy migration from the shell to the core is forced *via* sensitizing Yb-shells protected by inert shells. This has been shown, for example, by Zhou *et al.* on Yb,Tm@Yb@inert particles.[30] A recent review article gives an excellent overview of different types of multishell approaches, including the doping with different sensitizers to shift excitation wavelengths and combining different activators to achieve multicolored emissions.[31] A striking example for the design of complex, efficient multishell particles is provided by Jin *et al.* by synthesizing particles of Gd,Yb,Tm@Yb@Gd,Yb,Nd@Gd architecture to generate a six-photon energy cascade (Figure 5.1c). Directed energy migration from sensitizer shells to activator-containing cores brings the decisive advantage. A combination of the two different sensitizers Yb^{3+} and Nd^{3+} in an additional shell enables excitation at 808 nm, thus avoiding sample overheating in aqueous media upon 980 nm excitation. The presence of Gd^{3+} enables energy trapping in highly excited states, which reduces the probability of luminescence quenching, leading to an even brighter upconversion.[29]

These examples clearly illustrate that there is potential in novel core-shell particle architectures and doping ratios that are unusual at first glance. These developments are only just beginning, and a great deal of progress can still be expected. The future certainly lies in complex particle architectures in which different lanthanides are combined but in different compartments of the particles. This can be achieved as described in the examples above, but even more complex structures can be imagined, for example by using anisotropic particles such as rods and platelets. Upconversion nanoparticles with a hexagonal crystal structure possess two different types of crystal facets, the hexagonal (001) and the rectangular (100) facet, which have different affinities for different ligands. In principle, this affinity can be used to achieve anisotropic growth, as Jin *et al.* have already shown impressively (Figure 5.2a).[32]
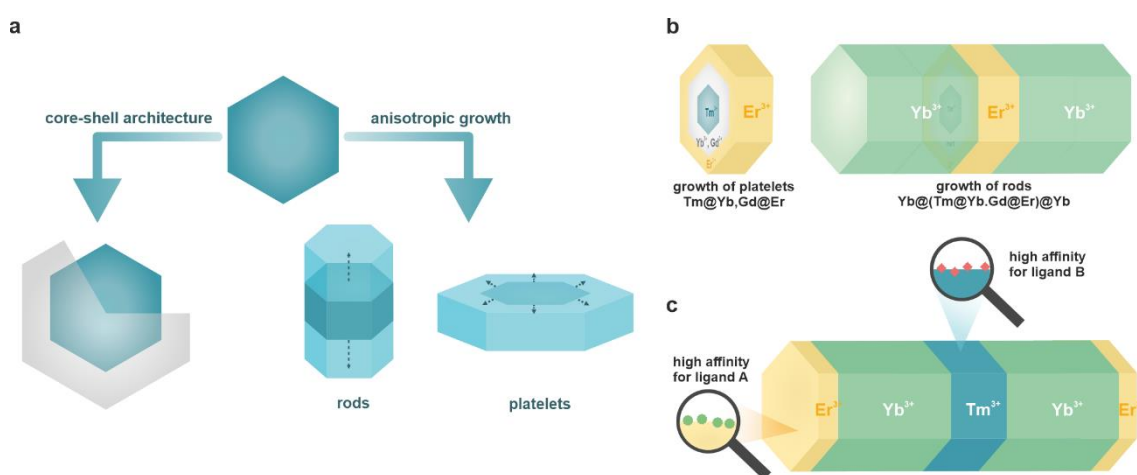
Figure 5.2. (a) Strategies for particle design. (b) Platelet growth (Tm@Yb,Gd@Er) followed by rod growth, where the platelets are prolongered with strongly absorbing NaYbF$_4$. The Er^{3+} is exposed to the environment and therefore accessible to analytes, while Tm^{3+} in the inside can be used for reference. (c) Design of upconversion rods with Er^{3+} on the outer edges and Tm^{3+} in the center. Different sensitivities of different ligands to the hexagonal or rectangular surface could allow recognition of different ligands by Er^{3+}/Tm^{3+}.

This could allow even more complex combinations of lanthanide ions and morphologies. A major goal would be to achieve efficient multicolor emissions by co-doping different lanthanides in different particle compartments. This could result in different sensitivities of the respective elements to the environment, as exemplified in Figure 5.2b, where Tm^{3+} in the core provides a reference emission, while the Er^{3+}emission, generated closer to the surface, is sensitive to environmental changes, thus enabling self-referential nanosensors for intracellular applications. By growing Yb^{3+} anisotropically, high absorption and energy migration from outside to inside can be achieved without increasing the distance between Er^{3+} and the surroundings. Such an approach could improve applications that exploit energy transfer processes from the particle surface to ligands or analytes in solution. The additional co-doping of Gd^{3+} not only enables energy trapping, but also creates multimodality as such

particles also become accessible for magnet resonance imaging (MRI). The second approach (Figure 5.2c) gives an example of how one could create a particle system that might be able to detect different analytes near the surface, since the analytes that prefer the hexagonal face will see a stronger change of Er^{3+} emissions while binding to rectangular areas would alter Tm^{3+} signals.

5.4 Challenges in Surface Chemistry

The famous quote "God made the bulk; surfaces were invented by the devil",[33] which is attributed to the Nobel Prize winner Wolfgang Pauli, describes quite well in an exaggerated way what also applies to UCNPs: No matter how much you can optimize the luminescent properties of the nanoparticles, in the end it is the interfacial phenomena on the particle surface that determine their usefulness. This is precisely why many research groups are united by the question: How can one gain control over the surface and thus stabilize and functionalize the particles at the same time? Nanomaterials have an exceptionally high surface-to-volume ratio, which is great because this high surface area provides an excellent platform for functionalization. At the same time, however, it is also a major disadvantage as it entails a high surface free energy. This means that literally anything sticks to the surface of a nanoparticle, which can lower that energy, or the nanoparticles stick together and form agglomerates.[34] Attempts are thus being made to stabilize the nanoparticles and prevent aggregation by attaching ligands to the particle surface in a targeted manner *via* electrostatic forces or steric repulsion.[35] The biggest hurdle in surface design is that, in addition to high stability, functionalization is also desired at the same time (Figure 5.3).
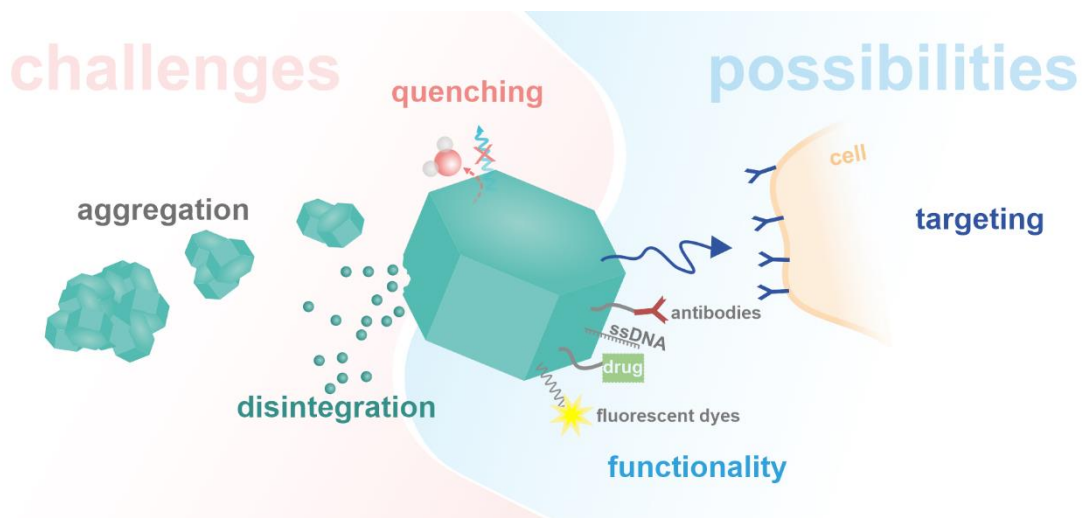

Figure 5.3. Challenges and possibilities in surface design of upconversion nanoparticles.

In a biological environment, the phenomena described at the particle surface apply in principle to all types of nanoparticles and many findings can be transferred from one type to other types of nanoparticles. In the specific case of UCNPs, two phenomena occur that deserve special attention. On the one hand, the upconversion luminescence is strongly quenched by O-H vibrations, and on the other hand, the particles tend to dissolve in high dilution. As a result, certain types of surface modification, some of which are very efficient, are less suitable for biological applications.

In particular, the most common, simplest, but also most vulnerable type of surface modification would be the method of ligand exchange. First, the original ligand (usually oleate) is removed from the UCNP surface by addition of $NOBF_4$ or HCl in a two-phase system of organic and aqueous solvent and then the desired ligand molecule is offered for binding.[36,37] The method is very popular because it is extremely versatile in terms of the selection of the attached ligands and can be carried out quickly without a large laboratory effort. In addition to the incomplete coverage of the particle surface – often only about 20% of the theoretical maximum coverage density is achieved[38]– the main problem with this method is that the ligands are bound to the nanoparticle surface according to their affinity. In the case of UCNPs, these are functional groups such as phosphate, sulfonate, or carboxylate, which are omnipresent in biological media as well. Consequently, depending on their affinity to the nanoparticle surface, an exchange of these groups is expected, and thus the properties of the particle will change over time.[39] The process of exchange can be slowed down by the addition of polymers instead of monodentate ligands, since the probability that all polymer functional groups are exchanged at the same time is low.[40] However, multidentate ligands also harbor the risk of cross-linking individual particles and thus promoting agglomeration. In addition, the already mentioned low degree of surface coverage does not represent a diffusion barrier for water molecules, which is why nanoparticles modified by such methods usually suffer greatly from luminescence quenching by water.[41]

In contrast, methods based on silica shell growth have the advantage that binding of the ligands to the silica surface is in most cases of covalent nature, enabled, *e.g.*, by the integration of APTES into the silica shell, which means that the ligands cannot be easily replaced.[42,43] However, in silica-coated UCNPs, the distance between the particle and the ligand is greatly increased, which can be disadvantageous for applications including FRET. Furthermore, it deserves special experimental skills to synthesize silica coated UCNPs free of aggregates or to have them later in monodisperse distribution through purification steps.

A very promising alternative strategy is the ligand addition method, in which the hydrophobic oleate remains on the particle surface and an amphiphilic ligand is attached to it. The resulting hydrophobic layer prevents hydrophilic molecules from diffusing to the particle surface, thereby reducing the likelihood of exchange, dissolution, and luminescence quenching. Various strategies have been developed, using amphiphilic polymers, phospholipids, or more simply, just oleate molecules to form this bilayer.[44–49]

In addition to colloidal stability, the chemical stability of nanoparticles is also an extremely important issue, which is often somewhat neglected in the excitement of the outstanding properties of the nanoparticle itself. Most inorganic nanoparticles cannot be regarded as inert systems but are in constant equilibrium with their environment and tend to disintegrate, which alters the photophysical properties of the systems on the one hand and makes the toxicity of the individual components relevant on the other. In the case of UCNPs, fluoride carries the risk of toxic effects because it can interact with many proteins, induce oxidative stress and tissue damage, and liberate free radicals.[50] However, the rare earth ions also have toxic effects.[51] The formation of lanthanide phosphates is strongly thermodynamically favored, which is why the lanthanide ions extract phosphate from the cells, *e.g.*, from lipid membranes, leading to organelle damages or inflammatory processes.[52] Since toxicity is always highly dependent on the concentration of the specific agent, it is of utmost importance to know about the chemical stability of the used nanomaterials before using them for biological applications. For UCNPs, long-term studies revealed that partial release of the ions occurs most rapidly within the first three days, with a fluoride ion release rate of about 0.12 mol% per hour in PBS buffer (pH 7.4).[53] This rate can even be accelerated by increasing the temperature or decreasing the particle size. For applications in living organisms, it would be desirable to prevent the dissolution of the nanoparticles to minimize the toxic effects of their components. Lisjak *et al.* have shown that an amphiphilic surface coating drastically reduces the disintegration rate by a factor of 8.[54] This again emphasizes the importance of carefully designing the nanoparticle surface and, if possible, incorporating hydrophobic barriers to increase the colloidal and chemical stability of the nanoparticles.

Although surface modification is crucial for any application of nanomaterials, what actually happens at the surface of a nanoparticle still is largely an enigma. This is mainly due to the difficulty of molecularly characterizing the interfaces of nanoscale objects with high local precision and at the same time across an entire particle ensemble. Light scattering experiments or nanoparticle tracking analysis can

demonstrate whether monodispersity can be maintained, while zeta potential measurements are commonly used to determine surface charge changes; but in most cases the characterization of the particle surface ends here. There are, of course, countless methods available to determine the exact composition of ligands on the surface. Methods such as TGA or quantitative NMR can determine the total amount of bound ligand, while colorimetric assays are used, for example, to quantify the available functional groups.[55–59] However, these methods are not very widely used for the characterization of nanoparticles, which is probably due to the large variety of ligands that differ in the method of quantification and the lack of standardized and validated protocols and techniques.[59] There is definitely an urgent need for further development in this field of analytical chemistry here. Critics of this statement may object that it is debatable whether it is necessary to consider the composition of the surface in detail, or whether one must assume that the composition at the particle interface changes significantly as soon as particles enter an organism and one can therefore save oneself the trouble. As proof of this, it can be provided that already in the first 30 s after a nanoparticle entered an organism, it is surrounded by a biomolecular corona.[60] This phenomenon is extremely frustrating for nanoparticle researchers as it reduces control over the chemical processes on the particle surface. Imagining an ideal nanoparticle for bioapplications, one would likely create a multifunctional nanoplatform that not only has therapeutic functions, enabling *e.g.*, photodynamic therapy or optogenetics, but also contains a targeting entity.[61–65] A protein corona significantly limits functionality, especially with respect to targeting. This is confirmed by a comparative study of the targeting efficiencies achieved to date. It was discovered with disillusionment that only about 0.7% of the nanoparticles reach the target tissue.[66] In general, the response of an organism to nanoparticles is strongly influenced by the formation of the protein corona, since the corona is first recognized by the cells, and hence the inherent particle plays a rather minor role from this point on.[67] Therefore, the protein corona is crucial for parameters such as blood circulation time, cytotoxicity, or biodistribution. On the one hand, the production of reactive oxygen species (ROS) and thus the cytotoxicity can be reduced, on the other hand the blood flow time is influenced, since the absorption of macrophage cells and thus the removal from the body can be increased or reduced depending on the adsorbed proteins.[68]

Although the formation of the protein corona appears to be an undesirable phenomenon at first glance, it can be of great benefit. In addition to reduced cytotoxicity, a protein corona can also help to internalize nanoparticles into cells.[60,68,69] In addition, the dissolution of nanoparticles is slowed down when the

particle is protected by proteins.[70] However, it was found that the formation of the protein corona is highly dependent on the ligands used. A high surface charge density favors the attachment of proteins to the particle surface,[71] while long-chain polymers as PEG lead to reduced protein corona formation due to the formation of a hydrophilic protective layer.[72,73] Since this in turn leads to lower cell uptake, it is a difficult task to find the optimal balance between desired and undesired consequences of a protein corona.[60,68,74] It is clear that the characterization of the surface of UCNPs before and after entering complex biological processes in terms of their functionality, colloidal stability, and media toxicity should become more in focus in the coming years of research. This will also help to make the processes inside an organism more predictable and further improve the design of the particle surface.

5.5 Potential in Bioapplications

For many biomedical or bioanalytical questions that are based on optical probes, UCNPs represent an attractive way to solve them. Due to the NIR-excitation, they are particularly impressive where autofluorescence and low penetration depths of the excitation light have a limiting effect (Figure 5.4).
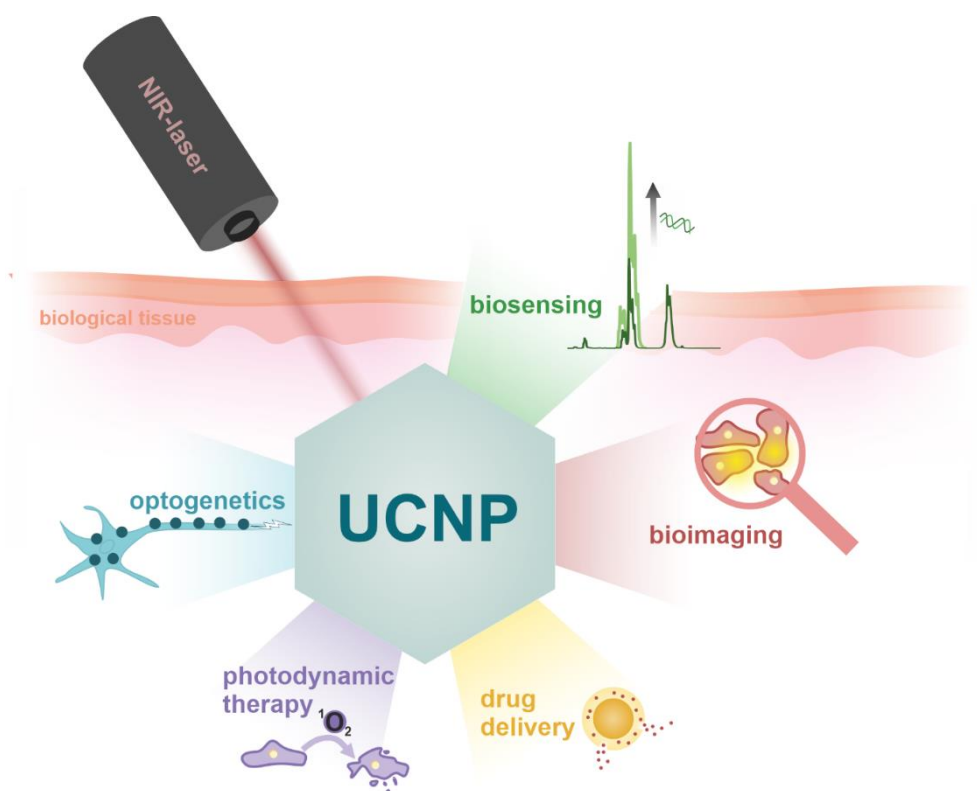

Figure 5.4. Possible applications for UCNPs in bioanalytical and biomedical sciences.

In sensor applications, NIR-excitation benefits above all from the high signal-to-noise ratio. The recent reviews by Chen *et al.* and de Camargo *et al.* summarize the wide variety of possible sensor applications based on UCNPs, ranging from parameters like temperature or pH to the detection of inorganic ions or biomolecules (nucleic acids, proteins, etc.).[75,76] Such sensors usually use the change in emission band intensities of the upconversion emission bands. Considering the several spectrally well separated emission bands of UCNPs, another advantageous feature, one clearly might envision ratiometric sensing applications. This is especially important when intracellular sensing is desired where calibration is not possible and self-referencing is the solution. When designing such a sensor particle, it is important to understand in detail the energetic processes between the lanthanide ions. Considering Er^{3+}-activated UCNPs, the green (approx. 525/545 nm) and the red emission (approx. 650 nm) are usually used for sensing purposes. However, due to the multiphoton process, the intensities of the individual bands depend on the power density of the excitation light. This represents a major challenge, especially in tissue, where light scattering is practically unavoidable and hence the excitation power density becomes an unknown quantity, which additionally can fluctuate locally. The preferred area of use for sensing applications is therefore more in cell culture rather than *in vivo*. Furthermore, considering that within one kind of lanthanide ion the energy levels are related to each other to a certain extent, it becomes clear that sensor applications of UCNPs pose several challenges. Considering Er^{3+}-doped systems, two excitation paths of the red emitting level are based on the green emitting levels. In specific terms, this means that the red emission would also lose intensity if the green-emitting energy level gets depopulated by an energy transfer.[77] The more complex core-multishell-particles with compartmentation of different lanthanide ions as presented earlier in this article offer a possible way out of the dilemma. The benefit of having two different types of activator ions, such as Er^{3+} and Tm^{3+} that do not interact when they are spatially separated, was recently demonstrated by Zhou *et al.* Here, the intensity ratio of 450 nm (Tm^{3+})/540 nm (Er^{3+}) of multishell nanoparticles of the type Yb,Er,Ce@inert@Yb,Tm could be used for thermometry with a sensitivity of almost 10% signal change in the physiological range.[78] This impressive result was achieved for particles dried to powder. Thus, to apply this method under biologically relevant conditions, a precise surface design is required. However, the idea of compartmentalization is obviously beneficial, as is the introduction of anisotropic structures like exemplified in Figure 5.2a, where perhaps even different ligand affinities could be achieved on a particle.

If the scattering and the absorption of the excitation light lead to problems, then of course this also applies to the emitted light, which cannot cross the tissue undisturbed either. Since this becomes a particular issue for shorter wavelength emissions, it could also lead to changes in peak ratios and therefore be an issue for ratiometric sensing. This does not mean that UCNPs are unsuitable for *in vivo* applications, as one way to circumvent this disadvantage is to look at luminescence lifetimes instead of luminescence intensities. Zhang *et al.* developed a FRET-based tumor detection sensor that provides information about changes in the lifetime of Nd^{3+}-doped UCNPs *via* the marker molecule peroxonitrite, which affects the spectral properties of a FRET-acceptor dye bound to the particle surface. This method impresses with its extremely stable lifetime signals, which are unaffected by scattering effects or light absorption.[79]

Similar considerations apply to imaging, where photoluminescence lifetime imaging (PLI) has proven to be an efficient tool, especially for multiplexed approaches that typically use different emission wavelengths to label different regions. Instead, using nanoparticles with the same wavelength but different luminescence lifetimes enables bioimaging with high sensitivity and accuracy.[80,81] In addition to upconversion, bioimaging also offers the charm of exploiting the Stokes-shifted NIR-emissions. The so-called NIR-II range (1,000–1,700 nm) enables almost background-free imaging due to the greatly reduced scattering and autofluorescence in this range.[82] It has also been shown several times that imaging in this range has clear advantages compared to imaging visible emissions from lanthanides.[83] Probably the most commonly used system for NIR-II imaging are nanoparticles doped with Yb^{3+}/Nd^{3+} sensitizers and Er^{3+} activators, sometimes additionally co-doped with Ce^{3+}, as reported by Dai *et al.* An approximately 9-fold enhancement of the 1,550 nm emission was obtained when 2% Ce^{3+} is doped into the nanocrystal.[84] A disadvantage of the Er^{3+} emission, although it is one of the brightest, is its quenching by O-H vibrations of water.[84] Recently, Kong *et al.* proposed a completely new concept for NIR-II imaging using $LiTmF_4(0.2\%Er)@LiYF_4$ nanoparticles that can be excited at 800 nm or 1,208 nm and show emissions between 1,600 and 1,900 nm. These can be traced back to the $^3F_4 \rightarrow ^3F_6$ transitions and have never been reported for imaging purposes before. This example illustrates the potential of a carefully tailored particle design with exceptional doping. According to Kong *et al.* a high Tm^{3+} content in the core particle, in combination with thick inert shells (5 nm), leads to bright emissions with a quantum yield of 14% for about 25 nm sized particles, which can even be increased to 16% by adding small amounts of Er^{3+} (0.2%) in the core.[85]

Such examples demonstrate the potential of the great variety of UCNPs. While the upconversion part of the spectrum can be used for sensors or actuators, the Stokes-emission in the NIR-II range seems to be very promising for imaging processes due to the high penetration depth. Upconversion is difficult to work with in tissues, at least when the goal is to quantify the emitted upconversion signals. However, detecting the upconversion signals is not always the goal. Perhaps the greatest, not fully utilized potential of upconversion in bioapplications so far is to use them as signal converters in organisms, locally converting low-energy light into high-energy light. The high-energy visible or UV light can be used for therapeutic purposes by initiating certain desired photochemical reactions. The major classes of such therapeutic applications are drug delivery, photodynamic therapy, and optogenetics.

An example for the use of UCNPs for drug delivery is the work of Wu *et al.* who succeeded in delivering drugs locally with UCNPs which are coated with mesoporous silica. The anticancer drug doxorubicin has been incorporated into the mesoporous silica, while a blue-light-sensitive ruthenium complex acts as a molecular valve. Under NIR-irradiation, the Tm^{3+} ions in the UCNP excite the ruthenium complex and release the anticancer drug.[86] Another smart approach encapsulates UCNPs and doxorubicin together in a light-sensitive disulfide-linked polymersome, which gets dissolved by the NIR-triggered upconversion luminescence and thus releases the active ingredient.[87]

Photodynamic therapy (PDT) uses a related but different concept to treat diseases such as cancer. The original principle is based on the local excitation of a photosensitizer (PS) into the excited singlet state, from which, in addition to internal conversion and fluorescence, intersystem crossing into a triplet state takes place. This triplet state PS can interact with a substrate and generate radicals and oxygenated products (Type I) or reacts directly with oxygen and generate $^1O_2$ (Type II). These highly reactive compounds can kill the surrounding cells, making the principle very attractive for tumor therapy. A major problem with this type of light therapy is that the photosensitizers used can be excited in the UV and visible range, which in turn means that non-invasive application is hardly possible due to the low penetration depth of the light.[88] For this reason, the combination of UCNPs with PS is extremely attractive, since the principle functionality (Figure 5.5a) has already been proven in several *in vitro* and *in vivo* studies.[89] An example of such an approach is the recent study presented by Kim *et al.*, in which two different types of PS were attached to the PEG-coated surface of a nanoparticle together with the tumor-targeting agent folic acid. (Figure 5.5b).[90] This approach impressively demonstrates the importance of surface design for such applications, as the challenge is to combine ligands that

ensure colloidal stability, ligands that enable therapeutic activity, and ligands for targeting. A major limitation for PDT is that tumor tissue is often hypoxic, what limits the production of reactive oxygen species (ROS) and thus the efficiency of the therapeutic approach. To solve this problem, several ideas have already been proposed, such as by Shi *et al.*, who coupled cyanobacteria to UCNPs that produce $^3O_2$ in situ, which is directly converted to $^1O_2$ by an upconversion-PS combination.[91] Another recent approach attaches the PS Chlorin-e6 together with CeO_2 to the surface of UCNPs. The CeO_2 can decompose H_2O_2 generated from a tumor to $^3O_2$, which is converted to $^1O_2$ by the PS.[92]

a

b
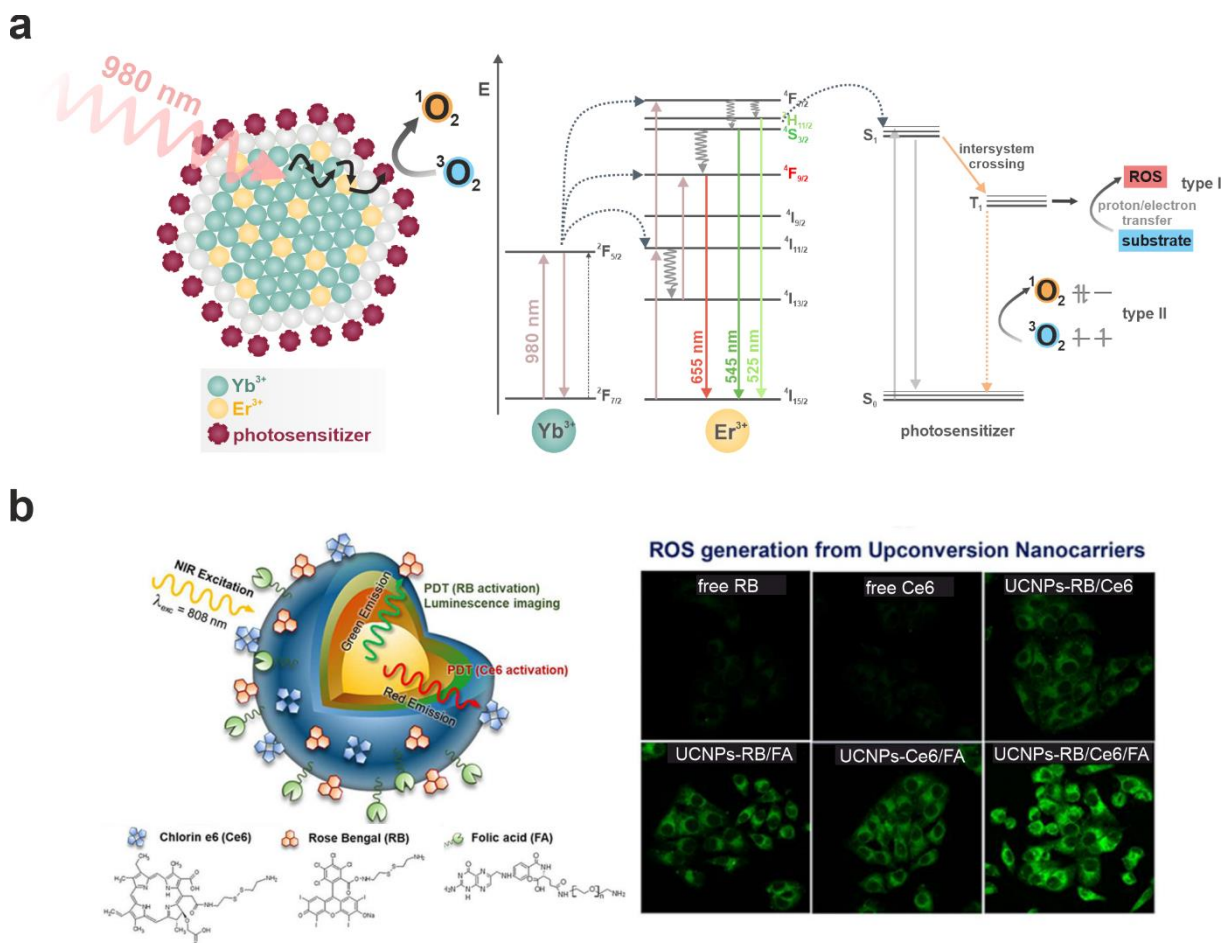
Figure 5.5. (a) Mechanism of photodynamic therapy involving UCNPs shown schematically (left) and in a simplified energy level diagram (right). The mechanism is shown for Yb/Er-doped UCNPs and a PS absorbing in the green range. (b) PDT approach by Kim *et al.*,[90] with two kinds of PS attached to a multishell UCNP. Schematic drawing of the particle (left) and ROS generation visualized with the ROS indicator DCFH-DA in KB cells incubated with the free photosensitizers, UCNPs with one or two PS attached and UCNPs w/ and w/o attached folic acid, which acts as tumor targeting agent. The graphic was adapted with permission from Ref.[90], ©2023 Elsevier.

A major opportunity to improve the therapeutic effect of upconversion systems is to focus on developing multimodal approaches. To give an example, one could imagine an upconversion nanocrystal doped with two activator ions, Er^{3+} and Tm^{3+}, and two

surface functionalities, a drug-release system triggered by Tm^{3+} emissions and a photosensitizer that is activated by Er^{3+} emissions combined with two different types of sensitizers (Yb^{3+} and Nd^{3+}). Such a photosensitizer could be Rose Bengal (green absorbing) or Chlorin-e6 (red absorbing), or ideally a combination of them to exploit both Er^{3+} emissions. With a well-designed core–multishell structure, it should be possible to switch between photodynamic therapy and drug delivery by changing the excitation wavelength.

The final application of UCNPs for biomedical purposes that shall be discussed here is the use of UCNPs for optogenetics. In optogenetics, light is used to control neurons or other cell types. This is done by introducing foreign genes into the target cell, resulting in the expression of light-sensitive ion channels. The channels can be opened or closed under irradiation with light, generating specific signals (Figure 5.6a). Since the activation in most cases works with visible light, which has low penetration depths, optical fibers are typically inserted into the brain. Therefore, the idea came up to use UCNPs for this method, allowing non-invasive excitation *via* NIR-light.[93] With optogenetic approaches using UCNPs, it has been already possible to achieve locomotion control in C. elegans, which changed their direction under 980 nm irradiation[94] or manipulation of the food intake behavior of mice, as recently demonstrated by Zhong *et al.*[95]

Zhang *et al.* presented a strategy that is elegant in both, the particle architecture as well as their application to neural manipulations (Figure 5.6b). They fabricated UCNPs with a total of seven shells, resulting in particles that are excitable at three different wavelengths (1,532/808/980 nm) and exhibit trichromatic green, red, and blue emissions. Combined with the expression of three different light-sensitive channel proteins (ChR2, ChrimsonR, and C1V1) that perfectly match the emission wavelengths, they were able to precisely control different types of ion channels. Manipulation of the locomotion behavior of mice was achieved, since the average running distance of the mice was increased under irradiation with 808 or 1,532 nm, while it was decreased under irradiation with 980 nm.[96]

Investigating the influences of ion channel manipulation on various behaviors will help neuroscientists gain a deeper understanding of the detailed mechanisms in the brain and will contribute to a better understanding of neuronal diseases. With optogenetics, it may also be possible to switch regions in the brain on or off, correcting aberrant neuronal signals that cause Parkinson's disease or epilepsy, for example.
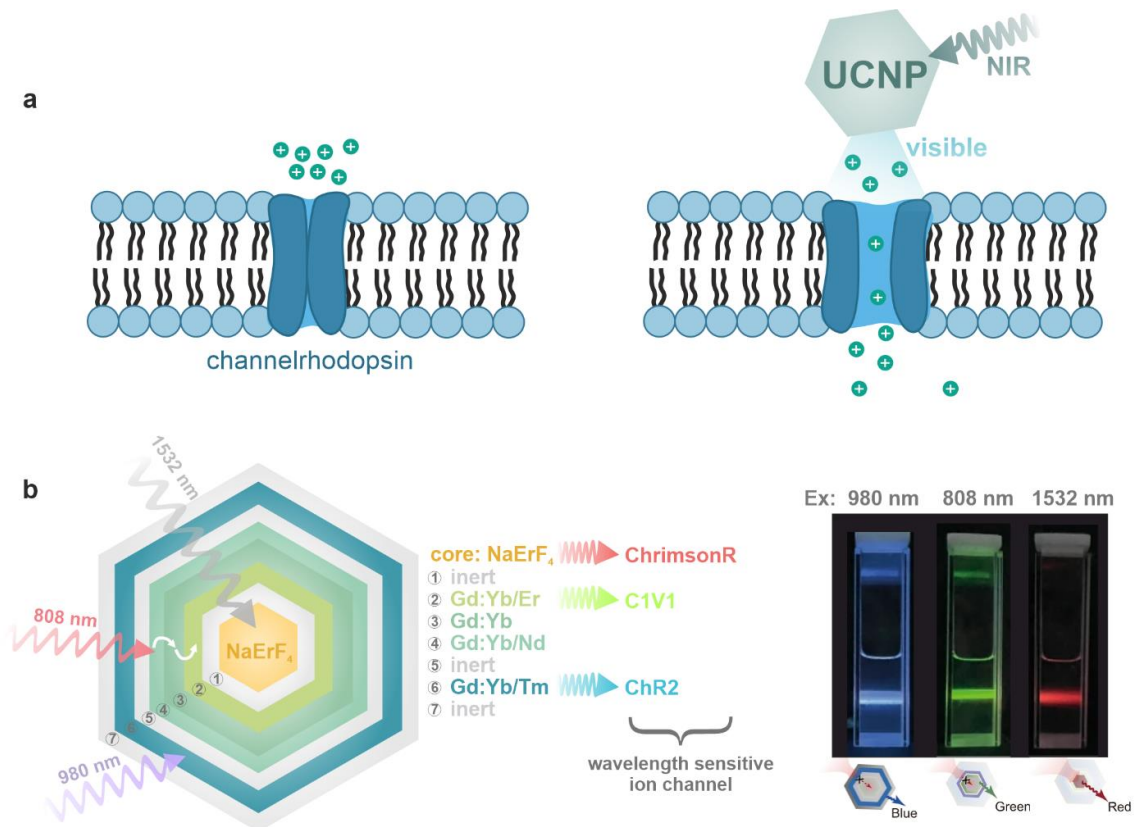
Figure 5.6. (a) Principle of UCNPs in optogenetics. Light sensitive ion channels (channelrhodopsins) open upon NIR-irradiation due to the upconversion of the NIR-light into visible light. (b) Particle design of a trichromatic upconversion nanoparticle suitable for optogenetic applications. Depending on the irradiation wavelength blue, green or red light is created which interacts with different kind of channelrhodopsins (ChR2, C1V1, ChrimsonR). The graphic is adapted from Ref.[96].

To achieve therapeutic relevance for humans, the use of UCNPs in optogenetics still must go through a long road of optimization. In mice, whose brains are only a small fraction of the size of the human brain, the NIR-light can reach all parts and stimulate the neurons. In the human brain, the light would have to cover far greater distances, while at the same time the excitation power densities of the laser light are limited, since the heating would cause tissue damage. Therefore, further optimization is required, *e.g.*, by implementing the multishell approaches described above, leading to improved upconversion efficiencies, together with a shift in excitation wavelengths to ranges, ideally above 1,000 nm, where water absorption does not occur, and scattering is reduced even more in comparison to the widely used 980 nm excitation. One should also pay special attention to surface engineering in optogenetics applications, since an additional challenge appears here: To get close to the neurons, the blood-brain barrier, which protects the brain from pathogens and toxins, must be conquered. Surface design is important for the process of transcytosis, since *e.g.*, positive ligands or peptides, which can bind to specific receptors on the membrane, can help to cross the barrier.[97,98] This once again emphasizes how important the entire interplay of particle architecture and surface design is and that neither of the

two areas should be neglected. However, it also becomes clear that one has different specific requirements for each application and the design must be precisely adapted to achieve optimal results in the end.

5.6 Outlook

The recently developed strategies together with the latest examples in the development of UCNPs demonstrate the outstanding potential of such probes in bioapplications. The bottom lines for further research are identified as follows:

(1) *Design and synthesis of complex particle architecture:* The spatial confinement of different doping within one particle gives rise to surprising features and better efficiencies, caused by energy migration and energy trapping zones. The possibilities in multishell architectures in combination with the large variety of lanthanide ions is not fully explored yet, especially when thinking of anisotropic particle shapes such as rods or platelets. One challenge beside small and efficient particle design is still to characterize and to maintain stability of the individual compartments during multishell growth at high temperature.

(2) *Thorough characterization of the particles surface and controlled surface engineering:* The progress, which was made in designing the surface coating of nanoparticles is enormous. However, the knowledge regarding the exact events happening on the UCNP surface is relatively low, especially as soon as the particle enters complex matrices. To better estimate whether and to what extent the function of the particle is preserved and how great the stability and toxicity of the particle is, precise surface characterization methods regarding composition, surface coverage, and density need to be established. With this, a next level can be entered by controlling a complex particle surface consisting of targeting moieties, reporter molecules, building blocks providing colloidal stability, or reservoirs capable to host drugs.

(3) *Better linkage of the individual disciplines in UCNP development:* So far, standard particle compositions and architectures have often been used for smart applications without particular attention to surface chemistry, while outstanding particle designs are often characterized only outside of a biological system. The

highly complex field of UCNP research, which demands expertise in so many disciplines, could be much more prospective with better collaboration among materials chemists, photophysicists, and medical scientists.

(4) *Establishment of standards:* To speed up the progress in particle development, especially when one thinks of the almost countless possibilities of multishell approaches, it would be very desirable to be able to easily compare the findings of individual researchers. A great benefit would be to have a minimal set of standards when reporting on luminescence features, surface composition, colloidal stability, or toxicity.

It is expected that this fascinating field of UCNP-research continues to grow and that topics like multimodality by generating hybrid composite particles will get in focus, with lots of further room for experimentation and improvement.

5.7 References

[1] Fang, X.; Zheng, Y.; Duan, Y.; Liu, Y.; Zhong, W. Recent Advances in Design of Fluorescence-Based Assays for High-Throughput Screening. *Anal. Chem.* **2019**, *91* (1), 482–504. DOI: 10.1021/acs.analchem.8b05303.

[2] Xu, Y.; Xu, R.; Wang, Z.; Zhou, Y.; Shen, Q.; Ji, W.; Dang, D.; Meng, L.; Tang, B. Z. Recent Advances in Luminescent Materials for Super-resolution Imaging via Stimulated Emission Depletion Nanoscopy. *Chem. Soc. Rev.* **2021**, *50* (1), 667–690. DOI: 10.1039/d0cs00676a.

[3] Haase, M.; Schäfer, H. Upconverting Nanoparticles. *Angew. Chem., Int. Ed.* **2011**, *50* (26), 5808–5829. DOI: 10.1002/anie.201005159.

[4] Bünzli, J.-C. G. Lanthanide Luminescence: From a Mystery to Rationalization, Understanding, and Applications. In *Handbook on the Physics and Chemistry of Rare Earths*; Gschneidner, K. A., Bünzli, J.-C., Pecharsky, V. K., Eds.; Elsevier, **2016**; 141–176. DOI: 10.1016/bs.hpcre.2016.08.003.

[5] Wen, S.; Zhou, J.; Zheng, K.; Bednarkiewicz, A.; Liu, X.; Jin, D. Advances in Highly Doped Upconversion Nanoparticles. *Nat. Commun.* **2018**, *9* (1), 2415. DOI: 10.1038/s41467-018-04813-5.

[6] Bhattacharjee, K.; Prasad, B. L. V. Surface Functionalization of Inorganic Nanoparticles with Ligands: A Necessary Step for their Utility. *Chem. Soc. Rev.* **2023**, *52* (8), 2573–2595. DOI: 10.1039/d1cs00876e.

[7] Yi, Z.; Luo, Z.; Qin, X.; Chen, Q.; Liu, X. Lanthanide-Activated Nanoparticles: A Toolbox for Bioimaging, Therapeutics, and Neuromodulation. *Acc. Chem. Res.* **2020**, *53* (11), 2692–2704. DOI: 10.1021/acs.accounts.0c00513.

[8] Chen, G.; Damasco, J.; Qiu, H.; Shao, W.; Ohulchanskyy, T. Y.; Valiev, R. R.; Wu, X.; Han, G.; Wang, Y.; Yang, C.; Ågren, H.; Prasad, P. N. Energy-Cascaded Upconversion in an Organic Dye-Sensitized Core/Shell Fluoride Nanocrystal. *Nano Lett.* **2015**, *15* (11), 7400–7407. DOI: 10.1021/acs.nanolett.5b02830.

[9] Paudel, H. P.; Zhong, L.; Bayat, K.; Baroughi, M. F.; Smith, S.; Lin, C.; Jiang, C.; Berry, M. T.; May, P. S. Enhancement of Near-Infrared-to-Visible Upconversion Luminescence Using Engineered Plasmonic Gold Surfaces. *J. Phys. Chem. C* **2011**, *115* (39), 19028–19036. DOI: 10.1021/jp206053f.

[10] Wiesholler, L. M.; Genslein, C.; Schroter, A.; Hirsch, T. Plasmonic Enhancement of NIR to UV Upconversion by a Nanoengineered Interface Consisting of NaYF$_4$:Yb,Tm Nanoparticles and a Gold Nanotriangle Array for Optical Detection of Vitamin B12 in Serum. *Anal. Chem.* **2018**, *90* (24), 14247–14254. DOI: 10.1021/acs.analchem.8b03279.

[11] Das, A.; Bae, K.; Park, W. Enhancement of Upconversion Luminescence Using Photonic Nanostructures. *Nanophotonics* **2020**, *9* (6), 1359–1371. DOI: 10.1515/nanoph-2020-0159.

[12] Gargas, D. J.; Chan, E. M.; Ostrowski, A. D.; Aloni, S.; Altoe, M. V. P.; Barnard, E. S.; Sanii, B.; Urban, J. J.; Milliron, D. J.; Cohen, B. E.; Schuck, P. J. Engineering Bright Sub-10-nm Upconverting Nanocrystals for Single-molecule Imaging. *Nat. Nanotechnol.* **2014**, *9* (4), 300–305. DOI: 10.1038/nnano.2014.29.

[13] Johnson, N. J. J.; He, S.; Diao, S.; Chan, E. M.; Dai, H.; Almutairi, A. Direct Evidence for Coupled Surface and Concentration Quenching Dynamics in Lanthanide-Doped Nanocrystals. *J. Am. Chem. Soc.* **2017**, *139* (8), 3275–3282. DOI: 10.1021/jacs.7b00223.

[14] Ma, C.; Xu, X.; Wang, F.; Zhou, Z.; Liu, D.; Zhao, J.; Guan, M.; Lang, C. I.; Jin, D. Optimal Sensitizer Concentration in Single Upconversion Nanocrystals. *Nano Lett.* **2017**, *17* (5), 2858–2864. DOI: 10.1021/acs.nanolett.6b05331.

[15] Shen, B.; Cheng, S.; Gu, Y.; Ni, D.; Gao, Y.; Su, Q.; Feng, W.; Li, F. Revisiting the Optimized Doping Ratio in Core/Shell Nanostructured Upconversion Particles. *Nanoscale* **2017**, *9* (5), 1964–1971. DOI: 10.1039/c6nr07687d.

[16] Tian, B.; Fernandez-Bravo, A.; Najafiaghdam, H.; Torquato, N. A.; Altoe, M. V. P.; Teitelboim, A.; Tajon, C. A.; Tian, Y.; Borys, N. J.; Barnard, E. S.; Anwar, M.; Chan, E. M.; Schuck, P. J.; Cohen, B. E. Low Irradiance Multiphoton Imaging with Alloyed Lanthanide Nanocrystals. *Nat. Commun.* **2018**, *9* (1), 3082. DOI: 10.1038/s41467-018-05577-8.

[17] Wang, Z.; Meijerink, A. Concentration Quenching in Upconversion Nanocrystals. *J. Phys. Chem. C* **2018**, *122* (45), 26298–26306. DOI: 10.1021/acs.jpcc.8b09371.

[18] Hu, P.; Wu, X.; Hu, S.; Chen, Z.; Yan, H.; Xi, Z.; Yu, Y.; Dai, G.; Liu, Y. Enhanced Upconversion Luminescence through Core/Shell Structures and its Application for Detecting Organic Dyes in Opaque Fishes. *Photochem. Photobiol. Sci.* **2016**, *15* (2), 260–265. DOI: 10.1039/c5pp00310e.

[19] Johnson, N. J. J.; van Veggel, F. C. J. M. Lanthanide-based Heteroepitaxial Core-Shell Nanostructures: Compressive Versus Tensile Strain Asymmetry. *ACS Nano* **2014**, *8* (10), 10517–10527. DOI: 10.1021/nn503946t.

[20] Hossan, M. Y.; Hor, A.; Luu, Q.; Smith, S. J.; May, P. S.; Berry, M. T. Explaining the Nanoscale Effect in the Upconversion Dynamics of β-NaYF$_4$:Yb^{3+}, Er^{3+} Core and Core–Shell Nanocrystals. *J. Phys. Chem. C* **2017**, *121* (30), 16592–16606. DOI: 10.1021/acs.jpcc.7b04567.

[21] Würth, C.; Fischer, S.; Grauel, B.; Alivisatos, A. P.; Resch-Genger, U. Quantum Yields, Surface Quenching, and Passivation Efficiency for Ultrasmall Core/Shell Upconverting Nanoparticles. *J. Am. Chem. Soc.* **2018**, *140* (14), 4922–4928. DOI: 10.1021/jacs.8b01458.

[22] Fischer, S.; Bronstein, N. D.; Swabeck, J. K.; Chan, E. M.; Alivisatos, A. P. Precise Tuning of Surface Quenching for Luminescence Enhancement in Core-Shell Lanthanide-Doped Nanocrystals. *Nano Lett.* **2016**, *16* (11), 7241–7247. DOI: 10.1021/acs.nanolett.6b03683.

[23] Gao, W.; Sun, Z.; Han, Q.; Han, S.; Cheng, X.; Wang, Y.; Yan, X.; Dong, J. Enhancing Upconversion Emission of Er^{3+} in Single β-NaYF$_4$ Microrod Through Constructing Different Inert and Active Shells with Doping Yb^{3+} ions. *J. Alloys Compd.* **2021**, *857*, 157578. DOI: 10.1016/j.jallcom.2020.157578.

[24] Lee, C.; Xu, E. Z.; Liu, Y.; Teitelboim, A.; Yao, K.; Fernandez-Bravo, A.; Kotulska, A. M.; Nam, S. H.; Suh, Y. D.; Bednarkiewicz, A.; Cohen, B. E.; Chan, E. M.; Schuck, P. J. Giant Nonlinear Optical Responses from Photon-avalanching Nanoparticles. *Nature* **2021**, *589* (7841), 230–235. DOI: 10.1038/s41586-020-03092-9.

[25] Liu, Y.; Lu, Y.; Yang, X.; Zheng, X.; Wen, S.; Wang, F.; Vidal, X.; Zhao, J.; Liu, D.; Zhou, Z.; Ma, C.; Zhou, J.; Piper, J. A.; Xi, P.; Jin, D. Amplified Stimulated Emission in Upconversion Nanoparticles for Super-Resolution Nanoscopy. *Nature* **2017**, *543* (7644), 229–233. DOI: 10.1038/nature21366.

[26] Bednarkiewicz, A.; Chan, E. M.; Kotulska, A.; Marciniak, L.; Prorok, K. Photon Avalanche in Lanthanide Doped Nanoparticles for Biomedical Applications: Super-resolution Imaging. *Nanoscale Horiz.* **2019**, *4* (4), 881–889. DOI: 10.1039/C9NH00089E.

[27] Zhang, Y.; Wen, R.; Hu, J.; Guan, D.; Qiu, X.; Zhang, Y.; Kohane, D. S.; Liu, Q. Enhancement of Single Upconversion Nanoparticle Imaging by Topologically Segregated Core-Shell Structure with Inward Energy Migration. *Nat. Commun.* **2022**, *13* (1), 5927. DOI: 10.1038/s41467-022-33660-8.

[28] Zhou, B.; Tang, B.; Zhang, C.; Qin, C.; Gu, Z.; Ma, Y.; Zhai, T.; Yao, J. Enhancing Multiphoton Upconversion Through Interfacial Energy Transfer in Multilayered Nanoparticles. *Nat. Commun.* **2020**, *11* (1), 1174. DOI: 10.1038/s41467-020-14879-9.

[29] Su, Q.; Wei, H.-L.; Liu, Y.; Chen, C.; Guan, M.; Wang, S.; Su, Y.; Wang, H.; Chen, Z.; Jin, D. Six-photon Upconverted Excitation Energy lock-in for Ultraviolet-C Enhancement. *Nat. Commun.* **2021**, *12* (1), 4367. DOI: 10.1038/s41467-021-24664-x.

[30] Liu, S.; Huang, J.; Yan, L.; Song, N.; Zhang, P.; He, J.; Zhou, B. Multiphoton Ultraviolet Upconversion Through Selectively Controllable Energy Transfer in Confined Sensitizing Sublattices Towards Improved Solar Photocatalysis. *J. Mater. Chem. A* **2021**, *9* (7), 4007–4017. DOI: 10.1039/D0TA11387E.

[31] Liu, S.; Yan, L.; Huang, J.; Zhang, Q.; Zhou, B. Controlling Upconversion in Emerging Multilayer Core-Shell Nanostructures: From Fundamentals to Frontier Applications. *Chem. Soc. Rev.* **2022**, *51* (5), 1729–1765. DOI: 10.1039/d1cs00753j.

[32] Liu, D.; Xu, X.; Du, Y.; Qin, X.; Zhang, Y.; Ma, C.; Wen, S.; Ren, W.; Goldys, E. M.; Piper, J. A.; Dou, S.; Liu, X.; Jin, D. Three-dimensional Controlled Growth of Monodisperse Sub-50 nm Heterogeneous Nanocrystals. *Nat. Commun.* **2016**, *7*, 10254. DOI: 10.1038/ncomms10254.

[33] Brantley, S. L.; White, A. F.; Hodson, M. E.; Surface Area of Primary Silicate Materials. In *Growth, Dissolution and Pattern Formation in Geosystems*; Jamtveit, B.; Meakin, P., Eds.; Springer Netherlands, **1999**, 291. DOI: 10.1007/978-94-015-9179-9

[34] Pfeiffer, C.; Rehbock, C.; Hühn, D.; Carrillo-Carrion, C.; Aberasturi, D. J. de; Merk, V.; Barcikowski, S.; Parak, W. J. Interaction of Colloidal Nanoparticles with their Local Environment: The (ionic) Nanoenvironment Around Nanoparticles is Different from Bulk and Determines the Physico-chemical Properties of the Nanoparticles. *J. R. Soc., Interface* **2014**, *11* (96), 20130931. DOI: 10.1098/rsif.2013.0931.

[35] Guerrini, L.; Alvarez-Puebla, R. A.; Pazos-Perez, N. Surface Modifications of Nanoparticles for Stability in Biological Fluids. *Materials* **2018**, *11* (7), 1154. DOI: 10.3390/ma11071154.

[36] Dong, A.; Ye, X.; Chen, J.; Kang, Y.; Gordon, T.; Kikkawa, J. M.; Murray, C. B. A Generalized Ligand-Exchange Strategy Enabling Sequential Surface Functionalization of Colloidal Nanocrystals. *J. Am. Chem. Soc.* **2011**, *133* (4), 998–1006. DOI: 10.1021/ja108948z.

[37] Rosen, E. L.; Buonsanti, R.; Llordes, A.; Sawvel, A. M.; Milliron, D. J.; Helms, B. A. Exceptionally Mild Reactive Stripping of Native Ligands from Nanocrystal Surfaces by Using Meerwein's salt. *Angew. Chem., Int. Ed.* **2012**, *51* (3), 684–689. DOI: 10.1002/anie.201105996.

[38] Himmelstoß, S. F.; Hirsch, T. Long-Term Colloidal and Chemical Stability in Aqueous Media of NaYF$_4$ -Type Upconversion Nanoparticles Modified by Ligand-Exchange. *Part. Part. Syst. Charact.* **2019**, *57*, 1900235. DOI: 10.1002/ppsc.201900235.

[39] Duong, H. T. T.; Chen, Y.; Tawfik, S. A.; Wen, S.; Parviz, M.; Shimoni, O.; Jin, D. Systematic Investigation of Functional Ligands for Colloidal Stable Upconversion Nanoparticles. *RSC Adv.* **2018**, *8* (9), 4842–4849. DOI: 10.1039/c7ra13765f.

[40] Grubbs, R. B. Roles of Polymer Ligands in Nanoparticle Stabilization. *Polym. Rev. (Philadelphia, PA, U. S.)* **2007**, *47* (2), 197–215. DOI: 10.1080/15583720701271245.

[41] Wilhelm, S.; Kaiser, M.; Würth, C.; Heiland, J.; Carrillo-Carrion, C.; Muhr, V.; Wolfbeis, O. S.; Parak, W. J.; Resch-Genger, U.; Hirsch, T. Water Dispersible Upconverting Nanoparticles: Effects of Surface Modification on their Luminescence and Colloidal Stability. *Nanoscale* **2015**, *7* (4), 1403–1410. DOI: 10.1039/c4nr05954a.

[42] Liu, J.-N.; Bu, W.-B.; Shi, J.-L. Silica Coated Upconversion Nanoparticles: A Versatile Platform for the Development of Efficient Theranostics. *Acc. Chem. Res.* **2015**, *48* (7), 1797–1805. DOI: 10.1021/acs.accounts.5b00078.

[43] Kembuan, C.; Saleh, M.; Rühle, B.; Resch-Genger, U.; Graf, C. Coating of Upconversion Nanoparticles with Silica Nanoshells of 5-250 nm thickness. *Beilstein J. Nanotechnol.* **2019**, *10*, 2410–2421. DOI: 10.3762/bjnano.10.231.

[44] Černič, T.; Koren, M.; Majaron, B.; Ponikvar-Svet, M.; Lisjak, D. Optimisation of Amphiphilic-Polymer Coatings for Improved Chemical Stability of NaYF$_4$-based Upconverting Nanoparticles. *Acta Chim. Slov.* **2022**, *69* (2), 448–457. DOI: 10.17344/acsi.2021.7336.

[45] Märkl, S.; Schroter, A.; Hirsch, T. Small and Bright Water-Protected Upconversion Nanoparticles with Long-Time Stability in Complex, Aqueous Media by Phospholipid Membrane Coating. *Nano Lett.* **2020**, *20* (12), 8620–8625. DOI: 10.1021/acs.nanolett.0c03327.

[46] Rojas-Gutierrez, P. A.; DeWolf, C.; Capobianco, J. A. Formation of a Supported Lipid Bilayer on Faceted LiYF$_4$:Tm^{3+}/Yb^{3+} Upconversion Nanoparticles. *Part. Part. Syst. Charact.* **2016**, *33* (12), 865–870. DOI: 10.1002/ppsc.201600218.

[47] Thanasekaran, P.; Chu, C.-H.; Wang, S.-B.; Chen, K.-Y.; Gao, H.-D.; Lee, M. M.; Sun, S.-S.; Li, J.-P.; Chen, J.-Y.; Chen, J.-K.; Chang, Y.-H.; Lee, H.-M. Lipid-Wrapped Upconversion Nanoconstruct/Photosensitizer Complex for Near-Infrared Light-Mediated Photodynamic Therapy. *ACS Appl. Mater. Interfaces* **2019**, *11* (1), 84–95. DOI: 10.1021/acsami.8b07760.

[48] Liras, M.; González-Béjar, M.; Peinado, E.; Francés-Soriano, L.; Pérez-Prieto, J.; Quijada-Garrido, I.; García, O. Thin Amphiphilic Polymer-Capped Upconversion Nanoparticles: Enhanced Emission and Thermoresponsive Properties. *Chem. Mater.* **2014**, *26* (13), 4014–4022. DOI: 10.1021/cm501663n.

[49] Schroter, A.; Arnau del Valle, C.; Marín, M. J.; Hirsch, T. Bilayer-Coating Strategy for Hydrophobic Nanoparticles Providing Colloidal Stability, Functionality, and Surface Protection in Biological Media. *Angew. Chem., Int. Ed.* **2023**, e202305165. DOI: 10.1002/anie.202305165.

[50] Johnston, N. R.; Strobel, S. A. Principles of Fluoride Toxicity and the Cellular Response: A Review. *Arch. Toxicol.* **2020**, *94* (4), 1051–1069. DOI: 10.1007/s00204-020-02687-5.

[51] Gnach, A.; Lipinski, T.; Bednarkiewicz, A.; Rybka, J.; Capobianco, J. A. Upconverting Nanoparticles: Assessing the Toxicity. *Chem. Soc. Rev.* **2015**, *44* (6), 1561–1584. DOI: 10.1039/c4cs00177j.

[52] Li, R.; Ji, Z.; Chang, C. H.; Dunphy, D. R.; Cai, X.; Meng, H.; Zhang, H.; Sun, B.; Wang, X.; Dong, J.; Lin, S.; Wang, M.; Liao, Y.-P.; Brinker, C. J.; Nel, A.; Xia, T. Surface Interactions with Compartmentalized Cellular Phosphates Explain Rare Earth Oxide Nanoparticle Hazard and Provide Opportunities for Safer Design. *ACS Nano* **2014**, *8* (2), 1771–1783. DOI: 10.1021/nn406166n.

[53] Lisjak, D.; Plohl, O.; Vidmar, J.; Majaron, B.; Ponikvar-Svet, M. Dissolution Mechanism of Upconverting AYF$_4$:Yb,Tm (A = Na or K) Nanoparticles in Aqueous Media. *Langmuir* **2016**, *32* (32), 8222–8229. DOI: 10.1021/acs.langmuir.6b02675.

[54] Plohl, O.; Kralj, S.; Majaron, B.; Fröhlich, E.; Ponikvar-Svet, M.; Makovec, D.; Lisjak, D. Amphiphilic Coatings for the Protection of Upconverting Nanoparticles Against Dissolution in Aqueous Media. *Dalton Trans.* **2017**, *46* (21), 6975–6984. DOI: 10.1039/c7dt00529f.

[55] Geißler, D.; Nirmalananthan-Budau, N.; Scholtz, L.; Tavernaro, I.; Resch-Genger, U. Analyzing the Surface of Functional Nanomaterials-How to Quantify the Total and Derivatizable Number of Functional Groups and Ligands. *Microchim. Acta* **2021**, *188* (10), 321. DOI: 10.1007/s00604-021-04960-5.

[56] Kunc, F.; Gallerneault, M.; Kodra, O.; Brinkmann, A.; Lopinski, G. P.; Johnston, L. J. Surface Chemistry of Metal Oxide Nanoparticles: NMR and TGA Quantification. *Anal. Bioanal. Chem.* **2022**, *414* (15), 4409–4425. DOI: 10.1007/s00216-022-03906-x.

[57] Hsiao, I.-L.; Fritsch-Decker, S.; Leidner, A.; Al-Rawi, M.; Hug, V.; Diabaté, S.; Grage, S. L.; Meffert, M.; Stoeger, T.; Gerthsen, D.; Ulrich, A. S.; Niemeyer, C. M.; Weiss, C. Biocompatibility of Amine-Functionalized Silica Nanoparticles: The Role of Surface Coverage. *Small* **2019**, *15* (10), e1805400. DOI: 10.1002/smll.201805400.

[58] Hennig, A.; Borcherding, H.; Jaeger, C.; Hatami, S.; Würth, C.; Hoffmann, A.; Hoffmann, K.; Thiele, T.; Schedler, U.; Resch-Genger, U. Scope and Limitations of Surface Functional Group Quantification Methods: Exploratory Study with Poly(acrylic acid)-grafted Micro- and Nanoparticles. *J. Am. Chem. Soc.* **2012**, *134* (19), 8268–8276. DOI: 10.1021/ja302649g.

[59] Sun, Y.; Kunc, F.; Balhara, V.; Coleman, B.; Kodra, O.; Raza, M.; Chen, M.; Brinkmann, A.; Lopinski, G. P.; Johnston, L. J. Quantification of Amine Functional Groups on Silica Nanoparticles: A Multi-Method Approach. *Nanoscale Adv.* **2019**, *1* (4), 1598–1607. DOI: 10.1039/c9na00016j.

[60] Docter, D.; Westmeier, D.; Markiewicz, M.; Stolte, S.; Knauer, S. K.; Stauber, R. H. The nanoparticle Biomolecule Corona: Lessons Learned - Challenge Accepted? *Chem. Soc. Rev.* **2015**, *44* (17), 6094–6121. DOI: 10.1039/c5cs00217f.

[61] Li, Z.; Lu, S.; Li, X.; Chen, Z.; Chen, X. Lanthanide Upconversion Nanoplatforms for Advanced Bacteria-Targeted Detection and Therapy. *Adv. Opt. Mater.* **2023**, 2202386. DOI: 10.1002/adom.202202386.

[62] Cao, J.; Zhang, L.; Ding, X.; Di Liu; Su, B.; Shi, J. Dual-Targeting Peptides RGD10-NGR9-Conjugated Lanthanide Nanoparticle@Polydopamine as Upconversion Nanoprobes for In Vivo Imaging of Lung Cancer. *Small Methods* **2020**, *4* (12), 2000648. DOI: 10.1002/smtd.202000648.

[63] Guryev, E. L.; Smyshlyaeva, A. S.; Shilyagina, N. Y.; Sokolova, E. A.; Shanwar, S.; Kostyuk, A. B.; Lyubeshkin, A. V.; Schulga, A. A.; Konovalova, E. V.; Lin, Q.; Roy, I.; Balalaeva, I. V.; Deyev, S. M.; Zvyagin, A. V. UCNP-based Photoluminescent Nanomedicines for Targeted Imaging and Theranostics of Cancer. *Molecules* **2020**, *25* (18), 4302. DOI: 10.3390/molecules25184302.

[64] Liang, G.; Wang, H.; Shi, H.; Wang, H.; Zhu, M.; Jing, A.; Li, J.; Li, G. Recent Progress in the Development of Upconversion Nanomaterials in Bioimaging and Disease Treatment. *J. Nanobiotechnol.* **2020**, *18* (1), 154. DOI: 10.1186/s12951-020-00713-3.

[65] Jalani, G.; Tam, V.; Vetrone, F.; Cerruti, M. Seeing, Targeting and Delivering with Upconverting Nanoparticles. *J. Am. Chem. Soc.* **2018**, *140* (35), 10923–10931. DOI: 10.1021/jacs.8b03977.

[66] Wilhelm, S.; Tavares, A. J.; Dai, Q.; Ohta, S.; Audet, J.; Dvorak, H. F.; Chan, W. C. W. Analysis of Nanoparticle Delivery to Tumours. *Nat. Rev. Mater.* **2016**, *1* (5), 16014. DOI: 10.1038/natrevmats.2016.14.

[67] Lynch, I.; Salvati, A.; Dawson, K. A. Protein-nanoparticle Interactions: What Does the Cell See? *Nat. Nanotechnol.* **2009**, *4* (9), 546–547. DOI: 10.1038/nnano.2009.248.

[68] Cai, R.; Chen, C. The Crown and the Scepter: Roles of the Protein Corona in Nanomedicine. *Adv. Mater.* **2019**, *31* (45), e1805740. DOI: 10.1002/adma.201805740.

[69] Frei, E. Albumin Binding Ligands and Albumin Conjugate Uptake by Cancer Cells. *Diabetol. Metab. Syndr.* **2011**, *3* (1), 11. DOI: 10.1186/1758-5996-3-11.

[70] Saleh, M. I.; Rühle, B.; Wang, S.; Radnik, J.; You, Y.; Resch-Genger, U. Assessing the Protective Effects of Different Surface Coatings on NaYF$_4$:Yb^{3+}, Er^{3+} Upconverting Nanoparticles in Buffer and DMEM. *Sci. Rep.* **2020**, *10* (1), 19318. DOI: 10.1038/s41598-020-76116-z.

[71] Gessner, A.; Lieske, A.; Paulke, B.; Müller, R. Influence of Surface Charge Density on Protein Adsorption on Polymeric Nanoparticles: Analysis by Two-dimensional Electrophoresis. *Eur. J. Pharm. Biopharm.* **2002**, *54* (2), 165–170. DOI: 10.1016/S0939-6411(02)00081-4.

[72] Wani, T. U.; Raza, S. N.; Khan, N. A. Nanoparticle Opsonization: Forces Involved and Protection by Long Chain Polymers. *Polym. Bull.* **2020**, *77* (7), 3865–3889. DOI: 10.1007/s00289-019-02924-7.

[73] Schöttler, S.; Becker, G.; Winzen, S.; Steinbach, T.; Mohr, K.; Landfester, K.; Mailänder, V.; Wurm, F. R. Protein Adsorption is Required for Stealth Effect of Poly(ethylene glycol)- and Poly(phosphoester)-coated Nanocarriers. *Nat. Nanotechnol.* **2016**, *11* (4), 372–377. DOI: 10.1038/nnano.2015.330.

[74] Voronovic, E.; Skripka, A.; Jarockyte, G.; Ger, M.; Kuciauskas, D.; Kaupinis, A.; Valius, M.; Rotomskis, R.; Vetrone, F.; Karabanovas, V. Uptake of Upconverting Nanoparticles by Breast Cancer Cells: Surface Coating versus the Protein Corona. *ACS Appl. Mater. Interfaces* **2021**, *13* (33), 39076–39087. DOI: 10.1021/acsami.1c10618.

[75] Jiang, W.; Yi, J.; Li, X.; He, F.; Niu, N.; Chen, L. A Comprehensive Review on Upconversion Nanomaterials-Based Fluorescent Sensor for Environment, Biology, Food and Medicine Applications. *Biosensors* **2022**, *12* (11). DOI: 10.3390/bios12111036.

[76] Arai, M. S.; Camargo, A. S. S. de. Exploring the Use of Upconversion Nanoparticles in Chemical and Biological Sensors: From Surface Modifications to Point-of-care Devices. *Nanoscale Adv.* **2021**, *3* (18), 5135–5165. DOI: 10.1039/d1na00327e.

[77] Würth, C.; Kaiser, M.; Wilhelm, S.; Grauel, B.; Hirsch, T.; Resch-Genger, U. Excitation Power Dependent Population Pathways and Absolute Quantum Yields of Upconversion Nanoparticles in Different Solvents. *Nanoscale* **2017**, *9* (12), 4283–4294. DOI: 10.1039/c7nr00092h.

[78] Liu, H.; Yan, L.; Huang, J.; An, Z.; Sheng, W.; Zhou, B. Ultrasensitive Thermochromic Upconversion in Core-Shell-Shell Nanoparticles for Nanothermometry and Anticounterfeiting. *J. Phys. Chem. Lett.* **2022**, *13* (10), 2306–2312. DOI: 10.1021/acs.jpclett.2c00005.

[79] Zhao, M.; Li, B.; Wu, Y.; He, H.; Zhu, X.; Zhang, H.; Dou, C.; Feng, L.; Fan, Y.; Zhang, F. A Tumor-Microenvironment-Responsive Lanthanide-Cyanine FRET Sensor for NIR-II Luminescence-Lifetime In Situ Imaging of Hepatocellular Carcinoma. *Adv. Mater.* **2020**, *32* (28), e2001172. DOI: 10.1002/adma.202001172.

[80] Zhu, X.; Liu, X.; Zhang, H.; Zhao, M.; Pei, P.; Chen, Y.; Yang, Y.; Lu, L.; Yu, P.; Sun, C.; Ming, J.; Ábrahám, I. M.; El-Toni, A. M.; Khan, A.; Zhang, F. High-Fidelity NIR-II Multiplexed Lifetime Bioimaging with Bright Double Interfaced Lanthanide Nanoparticles. *Angew. Chem., Int. Ed.* **2021**, *133* (44), 23737–23743. DOI: 10.1002/ange.202108124.

[81] Gu, Y.; Guo, Z.; Yuan, W.; Kong, M.; Liu, Y.; Liu, Y.; Gao, Y.; Feng, W.; Wang, F.; Zhou, J.; Jin, D.; Li, F. High-sensitivity Imaging of Time-domain Near-infrared Light Transducer. *Nat. Photonics* **2019**, *13* (8), 525–531. DOI: 10.1038/s41566-019-0437-z.

[82] Diao, S.; Hong, G.; Antaris, A. L.; Blackburn, J. L.; Cheng, K.; Cheng, Z.; Dai, H. Biological Imaging without Autofluorescence in the Second Near-infrared Region. *Nano Res.* **2015**, *8* (9), 3027–3034. DOI: 10.1007/s12274-015-0808-9.

[83] Fan, Y.; Zhang, F. A New Generation of NIR-II Probes: Lanthanide-Based Nanocrystals for Bioimaging and Biosensing. *Adv. Opt. Mater.* **2019**, *7* (7), 1801417. DOI: 10.1002/adom.201801417.

[84] Zhong, Y.; Ma, Z.; Zhu, S.; Yue, J.; Zhang, M.; Antaris, A. L.; Yuan, J.; Cui, R.; Wan, H.; Zhou, Y.; Wang, W.; Huang, N. F.; Luo, J.; Hu, Z.; Dai, H. Boosting the Down-shifting Luminescence of Rare-earth Nanocrystals for Biological Imaging Beyond 1500 nm. *Nat. Commun.* **2017**, *8* (1), 737. DOI: 10.1038/s41467-017-00917-6.

[85] Chang, Y.; Chen, H.; Xie, X.; Wan, Y.; Li, Q.; Wu, F.; Yang, R.; Wang, W.; Kong, X. Bright Tm^{3+}-based Downshifting Luminescence Nanoprobe Operating Around 1800 nm for NIR-IIb and c Bioimaging. *Nat. Commun.* **2023**, *14* (1), 1079. DOI: 10.1038/s41467-023-36813-5.

[86] He, S.; Krippes, K.; Ritz, S.; Chen, Z.; Best, A.; Butt, H.-J.; Mailänder, V.; Wu, S. Ultralow-intensity Near-infrared Light Induces Drug Delivery by Upconverting Nanoparticles. *Chem. Commun.* **2015**, *51* (2), 431–434. DOI: 10.1039/C4CC07489K.

[87] Tsai, M.-F.; Lo, Y.-L.; Soorni, Y.; Su, C.-H.; Sivasoorian, S. S.; Yang, J.-Y.; Wang, L.-F. Near-Infrared Light-Triggered Drug Release from Ultraviolet- and Redox-Responsive Polymersome Encapsulated with Core-Shell Upconversion Nanoparticles for Cancer Therapy. *ACS Appl. Bio Mater.* **2021**, *4* (4), 3264–3275. DOI: 10.1021/acsabm.0c01621.

[88] Chilakamarthi, U.; Giribabu, L. Photodynamic Therapy: Past, Present and Future. *Chem. Rec.* **2017**, *17* (8), 775–802. DOI: 10.1002/tcr.201600121.

[89] Liu, Y.; Meng, X.; Bu, W. Upconversion-based Photodynamic Cancer Therapy. *Coord. Chem. Rev.* **2019**, *379*, 82–98. DOI: 10.1016/j.ccr.2017.09.006.

[90] Choi, J.; Kim, S. Y. Multi-shell Structured Nanocarriers with Enhanced Multiphoton Upconversion Luminescence Efficiency for NIR-mediated Targeted Photodynamic Therapy. *Appl. Mater. Today* **2023**, *31*, 101755. DOI: 10.1016/j.apmt.2023.101755.

[91] Huo, M.; Liu, P.; Zhang, L.; Wei, C.; Wang, L.; Chen, Y.; Shi, J. Upconversion Nanoparticles Hybridized Cyanobacterial Cells for Near-Infrared Mediated Photosynthesis and Enhanced Photodynamic Therapy. *Adv. Funct. Mater.* **2021**, *31* (16), 2010196. DOI: 10.1002/adfm.202010196.

[92] Xu, Y.; Wang, K.; Chen, Z.; Hu, R.; Zhao, Y.; Li, X.; Qu, J.; Liu, L. Oxygen Self-supplied Upconversion Nanoplatform Loading Cerium Oxide for Amplified Photodynamic Therapy of Hypoxic Tumors. *Biomater. Sci.* **2022**, *11* (1), 119–127. DOI: 10.1039/d2bm01455f.

[93] All, A. H.; Zeng, X.; Teh, D. B. L.; Yi, Z.; Prasad, A.; Ishizuka, T.; Thakor, N.; Hiromu, Y.; Liu, X. Expanding the Toolbox of Upconversion Nanoparticles for In Vivo Optogenetics and Neuromodulation. *Adv. Mater.* **2019**, *31* (41), e1803474. DOI: 10.1002/adma.201803474.

[94] Bansal, A.; Liu, H.; Jayakumar, M. K. G.; Andersson-Engels, S.; Zhang, Y. Quasi-Continuous Wave Near-Infrared Excitation of Upconversion Nanoparticles for Optogenetic Manipulation of C. elegans. *Small* **2016**, *12* (13), 1732–1743. DOI: 10.1002/smll.201503792.

[95] Sun, F.; Shen, H.; Yang, Q.; Yuan, Z.; Chen, Y.; Guo, W.; Wang, Y.; Yang, L.; Bai, Z.; Liu, Q.; Jiang, M.; Lam, J. W. Y.; Sun, J.; Ye, R.; Kwok, R. T. K.; Tang, B. Z. Dual Behavior Regulation: Tether-Free Deep-Brain Stimulation by Photothermal and Upconversion Hybrid Nanoparticles. *Adv. Mater.* **2023**, e2210018. DOI: 10.1002/adma.202210018.

[96] Liu, X.; Chen, H.; Wang, Y.; Si, Y.; Zhang, H.; Li, X.; Zhang, Z.; Yan, B.; Jiang, S.; Wang, F.; Weng, S.; Xu, W.; Zhao, D.; Zhang, J.; Zhang, F. Near-infrared Manipulation of Multiple Neuronal Populations via Trichromatic Upconversion. *Nat. Commun.* **2021**, *12* (1), 5662. DOI: 10.1038/s41467-021-25993-7.

[97] Ni, D.; Zhang, J.; Bu, W.; Xing, H.; Han, F.; Xiao, Q.; Yao, Z.; Chen, F.; He, Q.; Liu, J.; Zhang, S.; Fan, W.; Zhou, L.; Peng, W.; Shi, J. Dual-targeting Upconversion Nanoprobes Across the Blood-brain Barrier for Magnetic Resonance/Fluorescence Imaging of Intracranial Glioblastoma. *ACS Nano* **2014**, *8* (2), 1231–1242. DOI: 10.1021/nn406197c.

[98] Ceña, V.; Játiva, P. Nanoparticle Crossing of Blood-brain Barrier: A Road to New Therapeutic Approaches to Central Nervous System Diseases. *Nanomedicine* **2018**, *13* (13), 1513–1516. DOI: 10.2217/nnm-2018-0139.

Curriculum Vitae

Name	Alexandra Schroter
Geburtsdatum	04.07.1995
Geburtsort	Öhringen

Hochschulausbildung

01/2020-09/2023	**Promotion,** Universität Regensburg, Institut für Analytik, Chemo- und Biosensorik; "Particle Architecture and Surface Engineering of NIR-to-VIS Upconversion Nanoparticles as Luminescent Probes for Bioapplications" – Dr. Thomas Hirsch & Prof. Dr. Antje Baeumner
10/2017-09/2019	**Master of Science** der Chemie, Universität Regensburg Schwerpunkt: Bioanalytische Chemie *Masterarbeit*: „Efficient and Stable Lanthanide-based Spectral Shifters for Bioanalytical Applications" - Prof. Dr. Antje Baeumner
10/2013-08/2017	**Bachelor of Science** der Chemie, Universität Regensburg *Bachelorarbeit*: „Plasmonic Sensors with Upconversion Properties" - Prof. Dr. Antje Baeumner

Weiterbildungen

07/2021-10/2021	**Seminarreihe „BWL für Ingenieure"** Strategische Partnerschaft Sensorik e.V.
04/2021-07/2021	**Qualitätssicherungsmanagement in der Analytischen Chemie** Dr. Robert Schupfner, Universität Regensburg
10/2020	**Lösungsorientierte Gesprächsführung und Konfliktmanagement** Carpe verba! GmbH&Co.KG Regensburg
03/2019	**Frühjahrsschule „Industrielle Analytische Chemie"** Industrieforum der GDCh

Präsentationen

04/2023	Vortrag – ANAKON 2023 (Wien) *„NIR-to-VIS Spectral Shifters: Revisiting the Upconversion Nanoparticle Composition and Surface Functionalization for Bioanalytical Applications"*
09/2022	Posterpräsentation – MAF 2022 (Göteborg) *„A Bright Match: High Lanthanide Content Meets Surface Protection via Bilayer Strategy – Small, Efficient, NIR-excitable Upconversion Probes for Bioapplications"*
06/2022	Posterpräsentation – ANALYTICA 2022 (München) *„Synthesis and Characterization of Highly Efficient NIR-excitable Upconversion Luminescent Probes for Bioanalytical Applications"*
04/2021	Vortrag - UPCON 2021 (online) *„Small and Bright Core-Shell Upconversion Nanoparticles with High Concentration of Sensitizer- and Activator-Ions"*
09/2020	Vortrag - 14. Interdisziplinäres Doktorandenseminar des AK Prozessanalytik der GDCh (online) *„Synthesis and Design of Small and Efficient Upconversion Nanoparticles"*

Auszeichnungen

09/2020	**Studienpreis Analytische Chemie (Master)** Preis für herausragende Studienleistung in Analytischer Chemie der Fachgruppe Analytische Chemie des GDCh
07/2018	**Studienpreis Analytische Chemie (Bachelor)** Preis für herausragende Studienleistung in Analytischer Chemie der Fachgruppe Analytische Chemie des GDCh

Publikationen

Alexandra Schroter, Thomas Hirsch; *Control of Luminescence and Interfacial Properties as Perspective for Upconversion Nanoparticles*; Small, 2023, DOI: 10.1002/smll.202306042

Alexandra Schroter, Carla Arnau del Valle, María J. Marín, Thomas Hirsch; *Bilayer-Coating Strategy for Hydrophobic Nanoparticles Providing Colloidal Stability, Functionality, and Surface Protection in Biological Media*; Angewandte Chemie International Edition, 2023, DOI: 10.1002/anie.202305165

Alexandra Schroter, Susanne Märkl, Naomi Weitzel, Thomas Hirsch; *Upconversion Nanocrystals with High Lanthanide Content: Luminescence Loss by Energy Migration versus Luminescence Enhancement by Increased NIR Absorption;* Advanced Functional Materials, 2022, DOI: 10.1002/adfm.202113065

Susanne Märkl, **Alexandra Schroter**, Thomas Hirsch; *Small and Bright Water-Protected Upconversion Nanoparticles with Long-Time Stability in Complex, Aqueous Media by Phospholipid Membrane Coating*; Nano Letters, 2020, DOI: 10.1021/acs.nanolett.0c03327

Angelina Hirmer, Susanne Märkl, **Alexandra Schroter**, Thomas Hirsch; *Surface engineering of small and bright upconversion nanoparticles providing chemical and colloidal stability in biological media*; SPIE Nanoengineering, 2020, DOI: 10.1117/12.2568758

Lisa Wiesholler, Christa Genslein, **Alexandra Schroter**, Thomas Hirsch; *Plasmonic Enhancement of NIR to UV Upconversion by a Nanoengineered Interface Consisting of $NaYF_4$:Yb,Tm Nanoparticles and a Gold Nanotriangle Array for Optical Detection of Vitamin B12 in Serum*; Analytical Chemistry, 2018, DOI: 10.1021/acs.analchem.8b03279

Eidesstattliche Erklärung

Ich erkläre hiermit an Eides statt, dass ich die vorliegende Arbeit ohne unzulässige Hilfe Dritter und ohne Benutzung anderer als der angegebenen Hilfsmittel angefertigt habe; die aus anderen Quellen direkt oder indirekt übernommenen Daten und Konzepte sind unter Angabe des Literaturzitats gekennzeichnet.

Weitere Personen waren an der inhaltlich-materiellen Herstellung der vorliegenden Arbeit nicht beteiligt. Insbesondere habe ich hierfür nicht die entgeltliche Hilfe eines Promotionsberaters oder anderer Personen in Anspruch genommen. Niemand hat von mir weder unmittelbar noch mittelbar geldwerte Leistungen für Arbeiten erhalten, die im Zusammenhang mit dem Inhalt der vorgelegten Dissertation stehen.

Die Arbeit wurde bisher weder im In- noch im Ausland in gleicher oder ähnlicher Form einer anderen Prüfungsbehörde vorgelegt.

_____   _____

Ort, Datum   Unterschrift